Technische Universität München

Thermal Relics of Non-Minimal Dark Sectors

Dissertation

Johannes Paul Joachim Herms

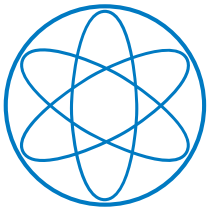

Physik-Department T30d, TUM

Technische Universität München

Physik-Department T30d

Thermal Relics of Non-Minimal Dark Sectors

Johannes Paul Joachim Herms

Vollständiger Abdruck der von der Fakultät für Physik der Technischen Universität München zur Erlangung des akademischen Grades eines

Doktors der Naturwissenschaften

genehmigten Dissertation.

Vorsitzende:		Prof. Dr. Laura Fabbietti
Prüfer der Dissertation:	1.	Prof. Dr. Alejandro Ibarra
	2.	Prof. Dr. Björn Garbrecht

Die Dissertation wurde am 17.08.2020 bei der Technischen Universität München eingereicht und durch die Fakultät für Physik am 15.09.2020 angenommen.

Abstract

Dark matter is a central part of our understanding of the Universe. The nature of its constituents is yet unknown, and relic particles produced by thermal processes in the early Universe are a prime candidate. This thesis studies scenarios where the relic abundance and observational prospects are not determined by the interactions of dark matter with the visible sector alone, but are instead crucially affected by the presence of additional dark matter flavours or self-interactions in the dark sector. We characterise the production mechanisms of multi-flavour scalar and fermionic dark matter in simple scenarios and find signatures not present in the minimal setup, in particular in cosmic gamma rays. Further, a non-minimal scenario of sterile neutrino dark matter is investigated, where strong self-interactions determine the relic abundance.

Zusammenfassung

Dunkle Materie ist ein zentraler Teil unseres Verständnisses des Universums. Ihre Bestandteile sind noch immer unbekannt, und durch thermische Prozesse im frühen Universum produzierte Reliktteilchen sind ein führender Kandidat. Diese Arbeit untersucht Szenarien in denen Reliktvorkommen und Nachweismöglichkeiten nicht allein durch die Interaktion der Dunklen Materie mit dem Lichtsektor bestimmt werden, sondern stattdessen entscheidend von zusätzlichen Dunkle Materie Flavours oder Selbstwechselwirkungen innerhalb des Dunkelsektors betroffen sind. Die Produktion von skalarer und fermionischer multi-flavour Dunkler Materie in einfachen Modellen wird beschrieben, was Nachweismöglichkeiten insbesondere durch kosmische Gammastrahlen aufzeigt, die im minimalen Modell nicht möglich sind. Desweiteren wird ein nicht-minimales Szenario von Steriler Neutrino Dunkle Materie untersucht, in dem starke Selbstwechselwirkungen das Reliktvorkommen bestimmen.

Contents

Chapter 1

Introduction

The nature of dark matter (DM) is a major open question in physics. Identifying the dark matter in the Universe would be a triumph for cosmology, where it would spectacularly confirm the standard Lambda-Cold-Dark-Matter (ΛCDM) cosmological model [1, 2], that has been very successful in explaining observations from cosmology down to the structures of galaxies. Dark matter may consist of elementary particles and the sheer amount of astrophysical and cosmological evidence for this unidentified matter component in the universe has led to the situation where this astrophysical/cosmological issue drives a large part of particle physics research.

In particle physics, the Standard Model of Particle Physics (SM) has just recently been completed by the discovery of a massive scalar boson at the Large Hadron Collider (LHC), whose properties measured so far perfectly match those expected of the Standard Model Higgs boson [3–5]. Big open questions remain, in particular regarding the origin of the mass scale and structure of the Standard Model. Interesting ideas like Supersymmetry, Grand Unification or extra dimensions, have been developed to address them. Many of these ideas for beyond the Standard Model (BSM) physics predict new neutral stable particles that could play the role of dark matter, which has been studied extensively in these contexts.

The contemporary absence of positive experimental results for theory-driven models containing particle dark matter has popularised the bottom-up perspective, focusing on the necessary features of dark matter and determining the associated phenomenology in a "no stone left unturned" approach [6]. This entails relating what we know about dark matter –the average relic density $\rho_{\rm DM}$, as well as aspects of its distribution $\rho_{\rm DM}(\vec{r})$– to distinctive signatures today, via general models.

In this spirit, particle dark matter candidates can be classified by their production mechanism. This work focuses on thermal dark matter production, understood to refer to scenarios where the dark matter abundance today is calculable from reactions with the thermal plasma of Standard Model particles in the early Universe. The simplest thermal dark matter candidates are *weakly interacting massive particles* (WIMPs), where the relic abundance is determined when dark matter annihilation in the early Universe *freezes-out* and stops [1]. This relates dark matter production to dark matter annihilation signals in overdense regions of the Universe today, and possibly dark matter scattering off terrestrial detectors or dark matter production at colliders. Equally simple in terms of model, but relying on stronger assumptions on cosmology, is *feebly-interacting-massive-particle* (FIMP) dark matter, whose relic density *freezes-in* through rare production reactions from the SM bath [7]. It is much more feebly coupled than WIMP dark matter, making it challenging to

test in the minimal setup.

In these phenomenological studies, minimality is often a guiding principle, hoping that it will reduce the specificity of the results to the particular model choices made, so that general conclusions can be drawn. However, the *dark sector* (referring to the particles and forces involved in dark matter production, often separated from the Standard Model *visible sector* by the symmetry that prevents dark matter decay) may consist of many particle species and new interactions, such that crucial signatures can be missed when only looking at minimal scenarios. This work goes beyond minimality by investigating the effects of additional dark matter flavours on the relic abundance and detectability for FIMP and WIMP dark matter. Further, we consider strong forces within the dark sector, which can determine the relic abundance by the freeze-out of number-changing self-annihilations (the SIMP mechanism, for *strongly interacting massive particles* [8, 9]).

We start out by reviewing the standard models of particle physics and cosmology in chapter 2, concluding with a brief thermal history of the Universe. Chapter 3 makes the case for dark matter based on the gravitational evidence across astrophysical and cosmological scales. It then situates thermal relic particles among the various viable dark matter candidates. Implications and prospects for the identification of thermal relic dark matter are reviewed in chapter 4. Chapter 5 describes the evolution of particle abundances in the early universe and presents standard relic abundance calculations in the WIMP and FIMP scenarios.

With this understanding of production and the strategies for detection of thermal relic dark matter, we go beyond the minimal scenario of one DM particle species whose relic abundance is determined by its interaction with the visible sector. In chapter 6, we add a second dark matter flavour to the minimal real-scalar FIMP model, finding promising detection possibilities in gamma ray telescopes. Chapter 7 repeats this analysis for multi-flavour fermionic dark matter and extends it to the full parameter space of dark matter couplings, allowing dark matter production via freeze-in or freeze-out. There can be strong interplay between the two flavours in the freeze-out case and we identify several distinct production regimes. We find that the overabundance constraint, together with constraints on dark matter decay, already rules out large parts of parameter space. Implications for dark matter indirect detection include much larger annihilation signals than expected in the single-flavour scenario. In chapter 8, we study a simple dark matter candidate, the *sterile neutrino*. We go beyond minimality by adding self-interactions, demonstrating the viability of Majorana fermion SIMP dark matter. In this case, the relic abundance can not be related to conventional dark matter indirect detection signatures, but to dark matter self-interactions, which can manifest themselves in the structures of dark matter halos. Chapter 9 summarises these results.

Parts of the work presented in this thesis have been published at:

- Johannes Herms, Alejandro Ibarra, and Takashi Toma. A new mechanism of sterile neutrino dark matter production. *JCAP*, 06:036, 2018. arXiv:1802.02973, doi:10.1088/1475-7516/2018/06/036
- Johannes Herms and Alejandro Ibarra. Probing multicomponent FIMP scenarios with gamma-ray telescopes. *JCAP*, 03:026, 2020. arXiv:1912.09458, doi:10.1088/1475-7516/2020/03/026

Chapter 2

The Standard Models of Particle Physics and Cosmology

Both particle physics and cosmology are today dominated by central "standard" models, underpinned by large amounts of evidence, from which exploration into the unkonwn is launched. In the case of the *Standard Model of Particle Physics*, its final predicted component –the Higgs boson– has been discovered, leading to the expectation that further measurements and theories of particle physics beyond the Standard Model (BSM physics) will refine and extend, rather than overthrow the Standard Model. In cosmology, this degree of confidence in a model has not yet been reached. However, the *Lambda-Cold-Dark-Matter* model is supported by increasingly precise observations and is proving very hard to dislodge from its position at the center of attention. The nature of its hypothesised central constitutents –the cosmological constant Λ and cold dark matter– are however still poorly understood.

In this chapter, the Standard Model of Particle Physics is introduced as the particle physics reality that all models of particle dark matter need to be compatible with within experimental accuracy, before introducing the ΛCDM-model of Big Bang cosmology that is both the motivation, as well as the basis to study the production and signatures of particle dark matter.

Throughout this text, natural units $\hbar = c = k_B = 1$ are used, with sign convention $(+,-,-,-)$ for the metric.

2.1 The Standard Model of Particle Physics

The Standard Model of particle physics is a quantum field theory that describes all known particles and their electromagnetic, weak and strong interactions in terms of the exchange of spin-1 gauge bosons. It is based on the gauge group

$$\mathrm{U}(1)_Y \times \mathrm{SU}(2)_L \times \mathrm{SU}(3)_c$$

that is spontaneously broken to that of the electromagnetic and strong interactions

$$\mathrm{U}(1)_{\mathrm{em}} \times \mathrm{SU}(3)_c$$

by the vacuum expectation value of the spin-0 Higgs field. The spin-1 gauge bosons that mediate the electromagnetic, weak and strong nuclear forces are the massless photon γ,

				$\mathrm{U}(1)_Y$	$\mathrm{SU}(2)_L$	$\mathrm{SU}(3)_c$
L^i	$\begin{pmatrix}\nu_e\\ e^-\end{pmatrix}_L$	$\begin{pmatrix}\nu_\mu\\ \mu^-\end{pmatrix}_L$	$\begin{pmatrix}\nu_\tau\\ \tau^-\end{pmatrix}_L$	$-\frac{1}{2}$	$\underline{\mathbf{2}}$	$\underline{\mathbf{1}}$
e^i_R	e^-_R	μ^-_R	τ^-_R	-1	$\underline{\mathbf{1}}$	$\underline{\mathbf{1}}$
Q^i	$\begin{pmatrix}u\\ d'\end{pmatrix}_L$	$\begin{pmatrix}c\\ s'\end{pmatrix}_L$	$\begin{pmatrix}t\\ b'\end{pmatrix}_L$	$\frac{1}{6}$	$\underline{\mathbf{2}}$	$\underline{\mathbf{3}}$
u^i_R	u_R	c_R	t_R	$\frac{2}{3}$	$\underline{\mathbf{1}}$	$\underline{\mathbf{3}}$
d^i_R	d_R	s_R	b_R	$-\frac{1}{3}$	$\underline{\mathbf{1}}$	$\underline{\mathbf{3}}$

Table 2.1: Fermions of the Standard Model and their charges and representations under the SM gauge group.

the massive Z, $W^\pm$ bosons and the massless gluons g respectively.[1] The *flavours* of up-type quarks (u, c, t), down-type quarks (d, s, b), charged leptons (e, μ, τ) and neutrinos (ν_e, ν_μ, ν_τ) are arranged into three *generations* of left-chiral $\mathrm{SU}(2)_L$-doublets and right-chiral $\mathrm{SU}(2)_L$-singlets, charged under the gauge group as shown in table 2.1.

The Lagrangian of the Standard Model in the unbroken phase is given by (following [12])

$$\begin{aligned}\mathcal{L}_{\mathrm{SM}} = &-\frac{1}{4}\left(W^a_{\mu\nu}\right)^2 - \frac{1}{4}B^2_{\mu\nu} - \frac{1}{4}\left(G^a_{\mu\nu}\right)^2\\ &+ (D_\mu H)^\dagger (D_\mu H) + m^2 H^\dagger H - \lambda (H^\dagger H)^2\\ &+ i\bar{L}^i \not{D}_\mu L^i + i\bar{e}^i_R \not{D}_\mu e^i_R + i\bar{Q}^i \not{D}_\mu Q^i + i\bar{u}^i_R \not{D}_\mu u^i_R + i\bar{d}^i_R \not{D}_\mu d^i_R\\ &- Y^e_{ij}\bar{L}^i H e^j_r - Y^u_{ij}\bar{Q}^i \tilde{H} u^j_r - Y^d_{ij}\bar{Q}^i H d^j_r + \mathrm{h.c.}\end{aligned} \tag{2.1}$$

Here, in the first line $B_{\mu\nu} = \partial_\mu B_\nu - \partial_\nu B_\mu$ is the field strength of the hypercharge gauge boson B_μ, $W^a_{\mu\nu}$ is the field strength of the $\mathrm{SU}(2)_L$ gauge bosons W^a_μ and $G^a_{\mu\nu}$ is the field strenght of the $\mathrm{SU}(3)_c$ gauge bosons g^a_μ. The second line accounts for the kinetic terms of the Higgs doublet $H = (\phi^+, \phi^0)^T$ with covariant derivative $D_\mu = \partial_\mu - igW^a_\mu \tau^a - y_H i g' B_\mu$, where g, g' are the $\mathrm{SU}(2)_L$ and $\mathrm{U}(1)_Y$ gauge couplings, respectively, τ^a is are the generators of the doublet representation of $\mathrm{SU}(2)_L$ and $y_H = 1/2$ is the hypercharge of the Higgs field. The third line consists of the fermion kinetic terms, with covariant derivatives as appropriate to the representation of the respective fermion (see table 2.1). The last line contains the Yukawa couplings between the Higgs field and the charged fermions, with $\tilde{H} \equiv i\sigma_2 H^*$. The gauge structure and particle content of the Standard Model has been confirmed at particle colliders and precision experiments, and any theory of particle physics beyond the Standard Model (*BSM* physics) has to accommodate these successes (for a review, see [5]).

The Universe today is in the broken phase of the Standard Model, where the Higgs-field has acquired a non-zero *vacuum expectation value* (vev) $\langle\phi_0\rangle = v/\sqrt{2}$ with $v = m/\sqrt{\lambda} = 247\,\mathrm{GeV}$, leaving the subgroup $\mathrm{U}(1)_{\mathrm{em}} \times \mathrm{SU}(3)_c$ of the SM gauge group unbroken and electromagnetic charge conserved. As a result, the particle spectrum today includes three massive spin-1 bosons $W^\pm$, Z and the massless photon γ.

The Yukawa couplings of eqn. (2.1) generate mass matrices for the quarks and charged leptons as $M^{e,u,d}_{ij} = \frac{v}{\sqrt{2}} Y^{e,u,d}_{ij}$, which upon diagonalisation yield the mass eigenstates we

[1] The forces associated to $\mathrm{U}(1)_Y \times \mathrm{SU}(2)_L$ are often referred to as the *electroweak forces*, and the strong force related to $\mathrm{SU}(3)_c$ is also called *quantum chromodynamics* (QCD).

observe as propagating particles. The rotation $U_{u,d,e,\nu}$ of flavours from the mass basis to the flavour basis of the $\mathrm{SU}(2)_L$ doublets (i.e. that of eqn. (2.1)) generates mixing effects that can be parameterised by the Cabbibo-Kobayashi-Maskawa matrix $V_{\mathrm{CKM}} = U_u^\dagger U_d$ in the case of quarks and the Pontecorvo-Maki-Nakagawa-Sakata matrix $V_{\mathrm{PMNS}} = U_e^\dagger U_\nu$.

The Standard Model, as introduced above, does not include masses for the neutrinos, for which there exists overwhelming evidence from the observation of neutrino flavour oscillations [5]. Eqn. (2.1) includes only renormalisable terms, up to mass dimension 4. Extending the theory to include also non-renormalisable operators, neutrino masses arise already at mass dimension-5, through the Weinberg operator $\mathcal{L}_{\mathrm{dim}-5} = -\kappa_{ij}(\bar{L}^i\tilde{H})(\tilde{H}^T(L^j)^c)$ (with $(L^j)^c$ the charge conjugate of L_j). The origin of neutrino masses in a renormalisable model implies BSM physics, and one possibility is encountered in passing in chapter 8.

Of particular importance to the study of relics from the early Universe is the question of stability. Heavy particles decay into lighter ones, unless this is forbidden by a symmetry. In the following, we review the stable particles in the Standard Model that make up the visible sector of our Universe.

The lightest particle is the photon. It is exactly massless in the Standard Model and hence absolutely stable. Next by mass are the neutrinos, the lightest fermions. Their decay into the lighter photons is forbidden by spacetime symmetry. The electron is the lightest charged particle and is stabilised by electromagnetic charge conservation. Quarks and gluons confine to $\mathrm{SU}(3)_c$-singlet, composite objects at energies below the QCD scale $\Lambda_{\mathrm{QCD}} \sim 200\,\mathrm{MeV}$. They form bosonic mesons (the lightest of which are the pions $\pi^\pm$, π^0) and fermionic baryons (the lightest of which are the proton and the neutron). Mesons decay into leptons or photons, but the lightest baryon, the proton, has never been observed to decay. Although its decay into e.g. a positron and a pion, $p \to e^+\pi^0$ is not forbidden by charge conservation or Lorentz symmetry, experiments constrain this decay rate to be smaller than $(1.6 \times 10^{34}\,\mathrm{yr})^{-1}$ [13]. This is a consequence of the accidental symmetry of baryon number conservation: Given the symmetries and particle content of the Standard Model, there is a conserved global $\mathrm{U}(1)_B$ symmetry under which all quarks carry charge 1/3. The proton is the lightest baryon (containing three quarks) and hence stable.

To conclude this brief review of the Standard Model of particle physics, note should be taken of its limitations: It is a very predictive model, able to explain virtually all particle physics observations to date in terms of a very limited number of free parameters, in a beautiful framework defined by symmetries. The absence of relevant neutrino masses in the Standard Model is an obvious blind spot, which is however easily covered by extensions that hardly modify non-neutrino-oscillation observables and offer little guidance on the possible embedding of the Standard Model in a more complete theory (though this is only a possibility; neutrino masses may well turn out to be key to understand physics beyond the Standard Model). Besides this, there are some lingering tensions between SM predictions and experimental data in precision or flavour observables, maybe the most significant one being the anomalous magnetic moment of the muon (e.g. [14]). The strongest reasons to be interested in particle physics beyond the Standard Model, however, are the absence of any explanation of its parameters, as well as the fact that the origin of the Universe we live in is far from anything expected from Standard Model physics alone. The origin of the electroweak scale v motivates many models of BSM physics (the *hierarchy problem* of stabilising the electroweak scale against quantum corrections from heavy new physics or the Planck scale, see e.g. [15]). Likewise, the flavour structure of the Yukawa couplings looks far from random and suggests that they are not independent free parameters in a more complete model (the *flavour problem*). The CP-violation in the QCD sector is tiny without apparent

reason, which has inspired explanations, such as the axion [16]. Further, the matter fields and forces of the Standard Model suggest the intriguing possibility of unification into a larger gauge group in a Grand Unified Theory (GUT).

Looking at the Universe today, glaring holes in the Standard Model as a fundamental theory of matter open up: While the Standard Model of particle physics is nearly completely symmetric between particles and antiparticles, people, stars and galaxies are made of baryons and electrons, with little trace left of antimatter. The Standard Model has no mechanism to address this question of *baryogenesis*. Of most relevance to this thesis, the bulk of the matter in the Universe appears to not actually be made up of Standard Model particles (or at least not in any form we have observed on Earth), but of Dark Matter, as discussed in section 3.1. While explanations exist that go beyond particle physics, it appears that all explanations do require particle physics beyond the Standard Model to work. Additionally, many of the particle physics models build to address questions originating in particle physics contain stable neutral particles that naturally play the role of dark matter.

In this thesis, simple extensions of the Standard Model that can account for particle dark matter are studied. They are often at least tangentially motivated by other open questions in particle physics, but primarily serve to explore particle dark matter phenomenology related to relic abundance and detection.

2.2 ΛCDM cosmology

The Lambda-Cold-Dark-Matter model of cosmology is a particular realisation of the Big Bang scenario, asserting that the Universe as observed today was once in a much hotter, denser state, with evolution to today governed by general relativity and the energy content of the Universe. This section briefly recapitulates Big Bang cosmology in the theory of General Relativity, before introducing the ΛCDM-model and its supporting observations.

Model On large scales, the Universe is observed to be strikingly homogeneous and isotropic. The metric describing a homogeneous, isotropic spacetime is the *Robertson-Walker* metric, described by the line element (see e.g. [1, 17])

$$ds^2 = dt^2 - R(t)^2 \left[\frac{dr^2}{1-kr^2} + r^2 d\theta^2 + r^2 \sin^2\theta d\varphi^2 \right] \tag{2.2}$$

with t the cosmic time parameter, $R(t)$ the scale factor and (r, θ, φ) comoving spatial coordinates, while $k \in \{-1, 0, 1\}$ is the curvature parameter. The evolution of the spacetime described by (2.2) depends on the matter content of the universe, described by the energy momentum tensor $T_{\mu\nu}$, and is governed by the Einstein equation

$$R_{\mu\nu} - \frac{1}{2} g_{\mu\nu} \mathcal{R} = 8\pi G T_{\mu\nu} + \Lambda g_{\mu\nu} \tag{2.3}$$

with $R_{\mu\nu}$ the Ricci tensor that contains the evolution of the metric $g_{\mu\nu}$, $\mathcal{R} = g^{\mu\nu} R_{\mu\nu}$ the Ricci scalar and $G = m_{\mathrm{Pl}}^{-2}$ Newton's constant (with Planck mass $m_{\mathrm{Pl}} = 1.22 \cdot 10^{-19}\,\mathrm{GeV}$). Λ is the cosmological constant.

To understand the evolution of the scale factor in the Robertson-Walker universe with homogeneous matter content, it is sufficient to look at the 00-component of the Einstein equation. This leads to the Friedmann-Lemaitre equation for the expansion rate $H \equiv \dot{R}/R$

(the *Hubble rate*) of the universe

$$H^2 = \frac{8\pi G}{3}\rho + \frac{1}{3}\Lambda - \frac{k}{R^2}\,, \tag{2.4}$$

where $\rho = T_{00}$ is the energy density. The energy content of the Universe can be modeled as a homogeneous, isotropic perfect fluid with density $\rho(t)$, and pressure $\mathcal{P}(t)$:

$$T^{\mu}{}_{\nu} = \mathrm{diag}(\rho, -\mathcal{P}, -\mathcal{P}, -\mathcal{P}) \tag{2.5}$$

Energy conservation $\nabla_\mu T^{\mu\nu} = 0$ in the expanding universe implies for the evolution of the energy density

$$\dot{\rho} + (\rho + \mathcal{P})\,\frac{3\dot{R}}{R} = 0\,. \tag{2.6}$$

For the simple equation of state

$$\mathcal{P} = \omega\rho, \qquad \text{with } \omega = \begin{cases} 0 & \text{matter} \\ 1/3 & \text{radiation} \\ -1 & \text{vacuum energy} \end{cases} \tag{2.7}$$

this leads to

$$\rho \propto R^{-3(1+\omega)} = \begin{cases} R^{-3} & \text{matter} \\ R^{-4} & \text{radiation} \\ \text{const.} & \text{vacuum energy}\,. \end{cases} \tag{2.8}$$

The scale factor dependence indicates that while vacuum energy dominates the energy density of the Universe today, there can be (and has been) an earlier epoch of matter domination, preceded by an epoch of radiation domination at very early times (small R).

The content of the universe is often expressed in terms of dimensionless *density parameters* Ω_i by normalising to the *critical density* ρ_C:

$$\Omega_i \equiv \frac{\rho_i}{\rho_C} \quad \rho_C \equiv \frac{3H^2(t)}{8\pi G}. \tag{2.9}$$

They take on special meaning when rewriting the Friedmann-Lemaitre eqn. (2.4) as

$$1 = \Omega_M + \Omega_r + \Omega_\Lambda - \frac{k}{H^2R^2}\,, \tag{2.10}$$

(with $\Omega_\Lambda = \Lambda/8\pi G$) showing that $\Omega = \Omega_M + \Omega_r + \Omega_\Lambda = 1$ corresponds to a spatially flat universe. Observation suggests that our Universe is spatially flat at the level of $|\Omega_k| \equiv |k/H^2R^2| \lesssim 0.002$ [18].

This short review enables us to formulate today's standard model of cosmology, the ΛCDM-model. The ΛCDM-model models the Universe as a spatially flat ($k = 0$) Friedmann-Lemaitre-Robertson-Walker Universe with metric eqn. (2.2) obeying eqn. (2.4). Its homogeneous energy content is characterised by the fractions of the critical density in radiation Ω_r, matter Ω_M and *vacuum energy/cosmological constant (Λ)* Ω_Λ today. The matter content of the universe has two contributions $\Omega_M = \Omega_b + \Omega_{\mathrm{DM}}$: one from baryons, Ω_b, and one from *cold dark matter (CDM)*, Ω_{DM}, a collisionless, non-relativistic perfect fluid. Also accounting for three parameters that are of little relevance in this thesis,[2] the ΛCDM-model is a simple 6-parameter model for the Universe at large (for a recent review, see e.g. [2]).

[2] These are the optical depth τ to the cosmic microwave background, as well as the amplitude A and spectral index n_s of the adiabatic curvature fluctuations that seeded the growth of structure in the Universe.

Evidence The evidence in support of ΛCDM reaches from the earliest available tracer of cosmological evolution to the present-day accelerated expansion of the Universe.

The ΛCDM-model allows to calculate the relic densities of particles and nuclei from the early Universe, using understanding of the microphysics in the associated production processes. The Standard Model of particle physics does not include physics to explain the huge relic abundance of baryons left after all antibaryons annihilated, and this baryon asymmetry η can be taken as one of the free parameters of ΛCDM (instead of Ω_b). Given an input value for this primordial abundance of baryons, the model predicts the abundances of light nuclei produced in *Big Bang Nucleosynthesis* (BBN) when the temperature of the Universe dropped below 1 MeV, yielding compatible results for η from the observed primordial ratios of D/H and ^{4}He/H [19]. This is the earliest evidence for ΛCDM, from a time when the energy density in the Universe was dominated by relativistic SM particles.

The most precise measure of the energy content of the Universe results from the measurement of correlations of anisotropies in the *cosmic microwave background* (CMB) and the distribution of matter in the Universe. When matter starts to dominate the evolution of the universe, the small inhomogeneities (that are taken as an initial condition in the ΛCDM-model, characterised by amplitude A and spectral index n_s) in the dark matter density begin to grow. While the baryon-photon plasma is still tightly coupled, it falls into the potential wells created by the dark matter, bouncing back from its own pressure when it becomes sufficiently overdense, creating acoustic density waves at the characteristic scale of the speed of sound of the plasma. The oscillation stopped when photons decoupled from baryons when their temperature dropped below $T \sim 1\,\text{eV}$, causing baryons and electrons to form neutral atoms and the Universe to become transparent to light. At this time of *recombination*, the density waves froze into place, forming the *baryon acoustic oscillations* (BAO), which determine the large scale structure of the Universe today. The released photons form the CMB, which carries the same pattern of inhomogeneities (observed as anisotropy of the CMB). Combined, the measurements of BAO and CMB anisotropies allow to precisely determine all ΛCDM parameters [18]. They find consistency with η determined from BBN. Further, both BBN and BAO/CMB are compatible with the Standard Model expectation of three neutrino species, decoupling from the baryon-electron-photon bath as predicted by particle physics.

The observed flatness of the universe, along with its measured matter and radiation contents, imply that the expansion of the Universe today is dominated by the cosmological constant term, Ω_Λ. Local tracers of the cosmic expansion can measure the Hubble rate today [20], finding values in the same ballpark as those inferred from the CMB [21].

There are two significant disagreements between ΛCDM-prediction and data: The long-standing *lithium problem* is that the primordial abundance of ^{7}Li is only about a third of that predicted from the other light element abundances [22], which is a topic of ongoing investigation [23]. Recently, with increased precision in the CMB measurements by the Planck-satellite, tension has emerged between the value of the Hubble constant today H_0 as implied by ΛCDM fitted to CMB and BAO observations [18], and the direct determination of the cosmic expansion rate by the measurement of luminosity distances to supernovae serving as standard candles [20]. This *Hubble tension* is yet unresolved, and many extensions and refinements of ΛCDM have been proposed to address it (see e.g. [24]).

The observational status lends good support to the ΛCDM model, and the puzzling open issues may indicate a need for refinement rather than overhaul. The main difference between the status of the Standard Model of particle physics and the status of ΛCDM is then that the nature of the main component of the latter, dark matter, has not been identified.

Dark matter This thesis investigates particle physics processes that determine the present-day density of dark matter, which is a central observable. The PLANCK collaboration [18] gives its results from combining CMB and BAO observations in terms of present-day values

$$\Omega_{\mathrm{DM}} h^2 = 0.120 \pm 0.001 \tag{2.11}$$

with $h = H_0/(100\,\mathrm{km\,s^{-1}\,Mpc^{-1}})$ the present expansion rate of the Universe

$$H_0 = 67.4 \pm 0.5\ \mathrm{km\,s^{-1}\,Mpc^{-1}}\,. \tag{2.12}$$

The critical density can be written in terms of h as $\rho_C = 1.87840(9) \cdot 10^{-29} h^2\,\mathrm{g\,cm^{-3}} = 1.05371(5) \cdot 10^{-5} h^2\,\mathrm{GeV\,cm^{-3}}$ [5], leading to the present-day average dark matter density

$$\rho^{\mathrm{obs}}_{\mathrm{DM},0} = 1.26 \cdot 10^{-6}\,\mathrm{GeV\,cm^{-3}}\,. \tag{2.13}$$

The work presented in this thesis focuses on particle dark matter models whose relic density is related to thermal processes. Chapter 3 presents more evidence for cold dark matter and reviews classes of candidates.

A brief history of the early Universe

Just as in archaeology, studying relics of bygone eras enables us to look back into history. Using the standard models of particle physics and cosmology, we can interpret what observations we have, and extrapolate into the far prehistory. A note on Big Bang timekeeping is in order: Instead of counting time in seconds, dates in the early Universe are most usefully given in terms of temperature T (specifically, temperature T_γ of the photon gas), which characterises the energies available to particles at that moment. Later in time, dates are often given in *redshift* $1 + z \equiv R_0/R$, which is directly observable in astronomy through the reddening of emission lines of light emitted at smaller scale factor R.

The history of the early Universe (see e.g. [1,5]) starts with speculative pre-history, about which little is known for certain:

- $T = ?$, *Inflation:* The observable Universe is strikingly homogeneous, regions that are causally disconnected still have very similar density. This, together with the observed flatness of the Universe, can be explained by an initial period of inflation, where the Universe expanded exponentially.

- $T = T_{\mathrm{RH}}$, *Reheating:* The reheating temperature marks the start of radiation domination (i.e. the radiation era), and hence the start of the applicability of ΛCDM. History before reheating is unclear, and the reheating temperature is only constrained by BBN to be $T_{\mathrm{RH}} \gtrsim 4\,\mathrm{MeV}$ [25], with the implication that any cosmic history at larger temperatures includes speculation.

- $T_{\mathrm{EWPT}} \sim 160\,\mathrm{GeV}$, *Electroweak phase transition*: At temperatures larger than T_{EWPT}, the Higgs vev is zero, and electroweak symmetry is restored.

- $T \sim \Lambda_{\mathrm{QCD}} \sim 200\,\mathrm{MeV}$, *QCD phase transition*: At energies above Λ_{QCD}, unbound quarks and gluons populate the Universe. At the QCD phase transition, they confine into composite mesons and baryons.

Since we do not know the reheating temperature, we cannot be certain about what happened at these early times. However, we are probing the Standard Model of particle physics up to the TeV scale in the laboratory. This allows to meaningfully extrapolate the radiation dominated era to high temperatures when studying e.g. dark matter production, by the simple assumption that there should be no BSM effects beyond the one being studied. At $T \sim$ MeV, we enter well-established territory:

- $T \sim 1\,\mathrm{MeV}$, $t \sim 1\,\mathrm{s}$, *Neutrino decoupling*: Neutrinos decouple from the baryon-photon gas. Their relic density is determined by the value of the decoupling temperature, which can be calculated in the Standard Model and agrees with observation.
- $T \lesssim 1\,\mathrm{MeV}$, *Big Bang Nucleosynthesis*: Neutrons decouple and form light nuclei with protons. The primordial abundance of light nuclei, together with the neutrino relic density, is the earliest probe of cosmology.
- $T \sim 1\,\mathrm{eV}$, $z \sim 3350$, *Matter-radiation equality* [5]: Start of the matter dominated era.
- $z \sim 1100$, $T \sim 0.2\,\mathrm{eV}$, $t \sim 10^{13}\,\mathrm{s}$ *Recombination / CMB decoupling*: Electrons and nuclei combine into atoms, the Universe becomes transparent to photons. Relic photons form the cosmic microwave background.

As discussed above, the CMB carries the first and most precise information about the average density of dark matter in the Universe. Dark matter production hence needs to have happened at earlier times, and we stop our review of the history of the early Universe here, at roughly 400 thousand years after the Big Bang.

Chapter 3

Dark matter – Evidence and Candidates

This chapter recapitulates the evidence counted towards the existence of dark matter (section 3.1), which determines the basic properties a dark matter candidate needs to fulfil. This is followed by a review of dark matter candidates in section 3.2. The aim of this chapter is to present a compelling argument for dark matter and situate thermally produced relic particles in the context of dark matter candidates; a review of the history of dark matter can e.g. be found at [26].

3.1 Evidence of Dark Matter

Dark matter is a common interpretation of numerous types of observations that range from the scale of hundreds of parsec in dwarf galaxies up to the gigaparsec scale of the observable Universe. The result that the ΛCDM cosmological model with cold dark matter as its centerpiece can account for all of these observations is the reason for the joint effort of astronomers, cosmologists and particle physicists to identify the nature of dark matter.

3.1.1 Galactic scales

The most illustrative evidence for dark matter is found in *galactic rotation curves*, i.e. the circular velocities of stars and gas as they rotate around their galactic center as a function of the distance from the center. They are obtained by measuring the Doppler shift of emission lines in visible light [27] or radio spectra [28], with the generic result that the rotation velocities of galaxies approach constant values at large distance, well beyond the extent of the optical disk of the galaxy (an example is shown in fig. 3.1). This is in contrast to the expectation from Newtonian gravity, where the rotation velocity at radius r is related to the enclosed mass $M(r)$ within that radius by

$$v(r) = \sqrt{\frac{GM(r)}{r}}\,, \tag{3.1}$$

which should be falling as $v \propto r^{-1/2}$ at large distances if $M(r) \sim$ const. beyond the extent of the galactic disk (dashed line in fig. 3.1). Instead, sticking to Newtonian dynamics,[1] the

[1] It should be noted that dark matter halos are neither the only, nor the simplest model that can explain galactic rotation curves. Instead, modifying Newtonian dynamics at low accelerations (MOND) [29] can

flat rotation curves imply the existence of non-luminous halos with mass profile $M(r) \propto r$ that extend beyond the stellar disks of galaxies. Kinematic tracers of the mass contained in galaxies offer detailed measurements of dark matter density profiles of galaxies, and together with simulations of galaxy formation offer insights on the nature of dark matter, as well as its expected local density in the Solar sytem (e.g. [32]).

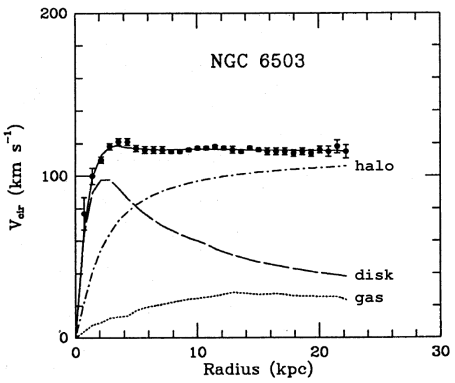

Figure 3.1: Example rotation curve of dwarf spiral galaxy NGC 6503 with inferred contribution of stellar disk, galactic gas and the dark matter halo to the rotation velocity. Figure adapted from fig. 1 of [33].

3.1.2 Galaxy clusters

Just as in rotating galaxies, kinematic tracers can also be used to determine the mass of galaxy clusters. In this case the velocity dispersion (determined again from Doppler-shift of emission lines) of individual galaxies in the cluster can be related to the mass of the cluster: Assuming equilibrium, the observed average kinetic energy $\langle T \rangle$ is related to the average gravitational potential energy $\langle U \rangle$ by the Virial theorem $\langle T \rangle = 1/2 \cdot \langle U \rangle$. This argument, applied to the Coma cluster by [34], was one of the first strong indications for large amounts of dark matter present in galaxy clusters, finding that the Coma cluster would have 400 times the mass estimated there for the galaxies in the cluster. This number becomes considerably smaller when taking into account the intracluster gas that dominates the baryonic mass of the cluster, but the conclusion that large amounts of dark matter are required to explain observations remains [35].

It is also possible to infer the masses of galaxy clusters from the X-ray luminosity of the hot cluster gas that is taken to be in hydrostatic equilibrium in the gravitational field of the cluster (e.g. [36]).

A third way of measuring the mass distribution inside galaxy clusters is via gravitational lensing, where the light from a background galaxy is distorted by the foreground cluster. This results in spectacular drawn-out arcs in the case of strong lensing or slight distortions of galaxy shapes in the case of weak lensing, both of which allow the reconstruction of the mass distribution of the lensing system. This has been put to use in characterising systems of colliding clusters [37], where the bulk of the baryonic mass contained in the intracluster

result in a one-parameter model that in principle predicts rotation curves from the visible baryonic matter alone and has proven hard to disentangle from the dark matter hypothesis on the basis of rotation curves alone (e.g. [30, 31]).

gas can become separated from the pressureless galaxies. The most impressive example is the *Bullet cluster* [38], shown in fig. 3.2, where a small cluster (the "bullet") passed through a larger one, leaving the fluid-like gas (visible in X-ray) trailing behind the collisionless constituent galaxies. Gravitational lensing reveals the gravitational potential of the system, dominated by the dark matter component. The fact that the centers of the gravitational potentials of the two clusters are still centered on the galaxies after the collision implies that dark matter is collisionless (the implications for dark matter self-interactions are discussed in sec. 4.2).

Figure 3.2: The Bullet Cluster system. The "bullet" on the right passed through the larger cluster on the left $\sim 100\,\mathrm{Myr}$ ago. Shown is a visible light image (galaxies), with X-ray intensity (pink) and mass distribution inferred from gravitational lensing (blue) superimposed. The offset between the mass distribution and the X-ray emitting plasma shows that the latter cannot dominate the mass of the system. Insted, the bulk of the mass is contained in the dark matter halos, which have passed through each other with little interaction and remained centered on the constitutent galaxies of the two subclusters [38]. NASA image from [39].

3.1.3 Large Scale Structure and the Cosmic Microwave Background

Having reviewed the evidence for dark matter in collapsed structures, we turn to the most precise measurements of the overall dark matter content of the Universe, which come from cosmology and are precisely those that underpin the ΛCDM cosmological model introduced in section 2.2. In particular, the density in protons and neutrons can be inferred precisely from the primordial abundances of light elements. Both the baryon density and the total matter density affect the evolution of matter density inhomogeneities from the start of matter domination to the decoupling of baryons from photons at recombination, which is observed today as the baryon acoustic oscillation feature in correlations of both CMB anisotropies and galaxy surveys at distance $\sim 100h^{-1}\,\mathrm{Mpc}$ [40]. The non-trivial interplay of cosmological parameters entering the correlation of CMB anisotropies can be used to give the most precise determination of cosmological parameters from observation [18], as well as constrain departures from the ΛCDM-model.

Small scales are more sensitive to detailed astrophysics affecting galaxy formation ("baryonic effects") and hence harder to interpret in terms of fundamental cosmological parameters or properties of dark matter. Detailed measurements of the matter power spectrum down to

small scales by observations of absorption lines in the spectra of distant quasars imprinted by intervening clouds of hydrogen (the *Ly-α forest*) are providing information on the smallest collapsed objects, important in identifying the nature of dark matter (e.g. [41]).

One should also note the role of simulation in the study of structure formation, translating the near-homogeneous CMB into the collapsed structures we observe today and shaping our expectations for what dark matter halos today should look like. Figure 3.3 illustrates the success of ΛCDM structure formation simulations in reproducing observed galaxy distributions [42]. The same general agreement between simulation and observation holds is the case for the shape of dark matter halos in galaxies and galaxy clusters, where dark-matter-only simulations find that a universal halo profile can fit simulated data across a wide range of halo masses [43, 44]. There remain discrepancies, especially in the centers of halos, where observations favour constant-density cores instead of the predicted cuspy profiles, which is discussed in more detail in section 4.2.

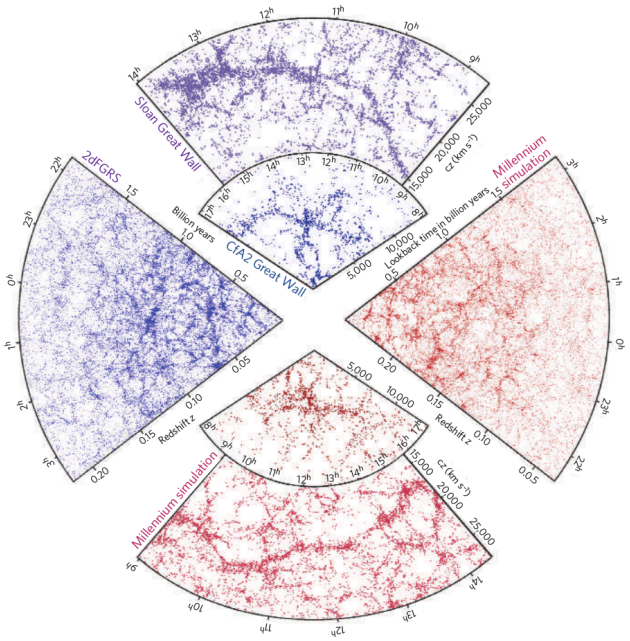

Figure 3.3: Galaxy distribution obtained from galaxy surveys (blue) and constructed from cosmological simulations (red) by [42], illustrating the agreement of ΛCDM with observation at the largest scales.
Reprinted by permission from Springer Nature: "The large-scale structure of the Universe", Volker Springel, Carlos S. Frenk and Simon D.M. White , Nature, 440:1137, copyright 2006 [42].

Summarising the evidence, dark matter appears central to the formation and shape of structures in the Universe at large. It evidently cannot dissipate energy and collapse to the same extent that baryons can, leaving the latter to shape the densest parts of the Universe. The ΛCDM model describes cosmological observables well, but leaves us with a major question: What is dark matter made of?

3.2 Dark Matter Candidates

This section reviews classes of dark matter candidates, sorting them roughly by production phenomenology instead of focusing on particular BSM models that can result in dark matter.

There are few generic constraints on dark matter besides the one that dark matter should be dark, i.e. not interact with photons too much (e.g. [45]). Individual compact dark matter objects can not be too massive, $m_{\mathrm{DM}} \lesssim 10 M_{\odot}$, from bounds on excessive kinetic heating of dwarf galaxies [46]. From the lower end, the dark matter mass is bounded by $m_{\mathrm{DM}} \gtrsim 10^{-21}\,\mathrm{eV}$ from the requirement that its astrophysical-scale wave nature should not interfere with structure formation [47] (i.e. dark matter is not too "fuzzy", see however [48]). This leaves a vast range of possibilities to be explored, and only by looking at particular plausible models can we get a better sense of what signatures to search for.

3.2.1 Massive compact halo objects

Dark matter could be made of large objects, called MACHOs (*massive compact halo objects*). Planets, comets and asteroids are non-luminous and collisionless on astronomical scales. Such objects, formed from the baryons participating in Big Bang Nucleosynthesis, cannot account for the bulk of dark matter, since the baryon abundance determined from BBN matches that determined from the CMB and is insufficient to make up dark matter.

Earlier formation of compact objects is possible, and *primordial black holes* (PBHs) that formed before BBN from large density inhomogeneities are a viable dark matter candidate (see e.g. [49, 50]). They are constrained towards small masses by $M_{\mathrm{PBH}} \gtrsim 10^{17}\,\mathrm{g}$ ($10^{-16} M_{\odot}$) from non-observation of their evaporation through Hawking radiation (a PBH specific bound) and towards large masses by $M_{\mathrm{PBH}} \lesssim 10^{23}\,\mathrm{g}$ ($10^{-10} M_{\odot}$) from microlensing surveys, which are MACHO-specific dark matter searches looking for changes in the brightness of stars due to lensing by massive compact objects passing the line of sight [49].

3.2.2 Particle dark matter

When not restricting the possibilities by imposing a particular production mechanism, the only lower bounds on the dark matter mass is the fuzzy-ness bound discussed above for bosonic particles, and a much stricter bound of $m_{\mathrm{DM}}^{\mathrm{fermion}} \gtrsim 0.4\,\mathrm{keV}$ for fermionic dark matter on Pauli exclusion grounds [51, 52]. Much of the extensive particle mass range from $10^{-21}\,\mathrm{eV}$ to the Planck scale has been populated with viable dark matter candidates, often in the context of models addressing open issues in particle physics not originally linked to dark matter. Dark matter candidates lighter than $\sim$ few keV are not necessarily cold, i.e. may have had a primordial velocity dispersion large enough to interfere with structure formation [53] (see sec. 4.1).

A class of dark matter candidates that can populate smaller masses are light pseudoscalar fields, like the *axion* as a solution to the strong-CP problem [16] and *axion-like-particles* (ALPs) that can arise in string theory [54]. They can be produced non-thermally i.e. without connection to the thermal bath of Standard Model particles. In the misalignment scenario, the axion starts out as a homogeneous field away from its minimum (which contributes to dark energy) and only behaves as cold dark matter once it starts oscillating when its mass term becomes significant compared to the cosmic expansion [54]. Their nature as coherently oscillating field on astrophysical length scales makes for signatures very distinct from more massive DM candidates.

Thermal relic particles

Most particle physics dark matter candidates fall into the class of thermal relics, i.e. relic particles whose abundance today is determined by their contact to the thermal bath of Standard Model particles in the early Universe.

Very large dark matter masses are possible in this case, and models with m_{DM} just two orders of magnitude below the Planck scale have been formulated [55], which would require a very large reheating temperature. A further example of a dark matter candidate that depends sensitively on the reheating temperature is the gravitino in supersymmetry [56]. In these cases where production is efficient only at high energies, direct searches for dark matter interactions in astrophysics or the laboratory are difficult, and one has to rely on different tests of the associated particle physics models.

Very attractive scenarios of thermal relic particle production arise when there exist renormalisable couplings between the dark and visible sectors, and the maximum interaction rate between the sectors is reached during radiation domination. This requires extrapolation of standard cosmology only to temperatures of order of the masses of new particles added to the Standard Model. Particular production mechanisms then relate the dark matter relic density to testable properties of the candidate particles.

If the interactions between visible and dark sector are very small, the DM relic abundance may be determined by rare reactions in the SM thermal bath, without itself reaching equilibrium. This is the *freeze-in* mechanism [7], which is treated in more detail in section 5.4. *Sterile neutrinos* also fall into this broad category [57], see section 8.1.

If the interactions between the visible and dark sectors are sizable, the sectors will equilibrate. The equilibrium abundance of massive particles becomes Boltzmann suppressed once the temperature drops below their mass, and the energy stored in them is converted to other particles. In the expanding Universe, this conversion process is bound to eventually become inefficient compared to the Hubble rate, if the particle under consideration is stable. At that time, the dark matter candidate *freezes out*, relating the final abundance to the strength of the interaction that depletes the number of dark matter particles. Dark matter particles produced this way are called *weakly-interacting-massive-particles* (WIMPs). In the standard WIMP mechanism, the relic abundance is determined by $2 \to 2$ annihilation reactions of WIMPs into Standard Model particles. This can naturally result in the observed relic abundance for DM masses around the electroweak scale, with electroweak-strength interactions. These often appear in theories addressing the hierarchy problem of the electroweak scale (e.g. the neutralino in supersymmetry [15]), which is referred to as the "WIMP miracle" (e.g. [58]). The freeze-out mechanism is however rather general and need not involve particles charged under the gauge group of the Standard Model [59]. The standard calculation of the WIMP relic abundance is introduced in section 5.3.

Many variants of the freeze-out scenario have been pointed out in the literature, depending on what kind of interaction is most effectively depleting the dark matter abundance. For example, it is possible that this freeze-out happens entirely within the dark sector [8]. In chapter 8, a scenario is presented where the strength of $4 \to 2$ number-changing interactions within the dark sector determines the relic abundance and possible signatures of a *strongly interacting massive particle* (SIMP) dark matter candidate.

Further, there are scenarios where the relic abundance depends crucially on out-of-equilibrium processes. This is the case for the massive relics of the Standard Model, where the baryon asymmetry determines the baryon and electron abundances today. If dark matter carries an additive conserved quantum number, *asymmetric dark matter* is possible, whose

relic abundance may be linked to baryogenesis (e.g. [60]).

Concluding note This chapter discussed observations on astrophysical and cosmological scales that can jointly be explained by cold dark matter. There are vastly different candidates for cold dark matter, from ultralight axions with wavelengths on astrophysical scales, over thermally produced dark matter particles with masses that range from those of the SM particles to the Planck scale, to massive objects as heavy as the Sun. The mechanism that determines their abundance today is a key ingredient in linking the observational evidence for dark matter to model-specific signatures that would allow to identify the nature of dark matter.

Chapter 4

Signatures of Particle Dark Matter

The identification of dark matter entails measuring signatures specific to a dark matter model. This may consist in finding *non-gravitational interactions* of dark matter with the visible sector for positive identification, but gravitational signatures of specific dark matter properties can also narrow down the search to dark matter models that have those properties.

This section reviews classes of signatures of thermally produced particle dark matter, from general constraints on its velocity dispersion (section 4.1), through signatures of dark matter self-interactions (section 4.2) to interactions with the visible sector searched for in dark matter indirect detection (section 4.3) and at laboratory experiments (section 4.4). Particular emphasis is given to the self-interaction and indirect detection signatures that are encountered in chapter 8 and chapters 6 and 7, respectively.

4.1 Free streaming

In the ΛCDM model, the structures in the Universe we observe today were seeded by primordial density fluctuations that on larger scales have been observed in the CMB anisotropies. The spectrum of density fluctuations can be summarised in the matter power spectrum, which provides a powerful probe of cosmology. This matter power spectrum can be measured from correlations of galaxies in galaxy surveys and at smaller scales in Ly-α absorption lines imprinted on the spectra of quasars (e.g. [61, 62]).

These density fluctuations start to grow and form structures once the matter dominated era begins. If dark matter is not very cold, small scale overdensities are erased by *free-streaming* of dark matter, suppressing the matter power spectrum. The observation of structures at small scales constrains this free-streaming scale, while non-observation could indicate significant free-streaming (see next section for a review of the "small scale crisis of ΛCDM", in particular the *missing satellites problem*).

The co-moving free streaming scale is given by the distance travelled by the free streaming particle before matter-radiation equality at $t_{\rm EQ}$.

$$\lambda_{\rm FS} = \int_{t_i}^{t_{\rm EQ}} \frac{\langle v \rangle(t')}{R(t')}\, dt' \,, \tag{4.1}$$

with $\langle v \rangle$ the velocity dispersion [1, 62]. If the particle becomes non-relativistic during the radiation dominated era, this approximately gives

$$k_{\rm FS} = \frac{2\pi}{\lambda_{\rm FS}} \simeq 5\,{\rm Mpc}^{-1} \left(\frac{m_{\rm DM}}{1\,{\rm keV}}\right) \left(\frac{T_\nu}{T_{\rm DM}}\right) , \tag{4.2}$$

where the phase space distribution of dark matter is assumed to be thermal with temperature $T_{\rm DM}$ and T_ν is the temperature of SM neutrinos [63]. The effect of free streaming on the matter power spectrum is usually determined using simulations, obtaining constraints by subsequently comparing the power spectrum to observations. Results are commonly given in terms of a bound on the mass of *warm dark matter*, which is defined as a dark matter candidate obeying [63]:[1]

$$\Omega_{\rm DM}h^2 = \left(\frac{T_{\rm WDM}}{T_\nu}\right)^3 \left(\frac{m_{\rm WDM}}{94\,\text{eV}}\right) , \tag{4.3}$$

which small-scale structure observations constrain to be (at 2σ CL) [53]

$$m_{\rm WDM} > 5.3\,\text{keV} . \tag{4.4}$$

Equation (4.3) and the dependence of eqn. (4.2) on $m_{\rm DM}/T_{\rm DM}$ can then be used to find the corresponding bounds on dark matter particles with different temperature. In dark matter models with multiple relic populations, higher velocity dispersions may be allowed for a subdominant dark matter component (e.g. [62,64]). Although currently there are only limits, a positive detection of a cutoff in the dark matter halo mass function could rule out many models of particle dark matter (e.g. [65]).

4.2 Self-interactions

The ΛCDM model for cosmology at the largest scales assumes that dark matter behaves as "dust", a collisionless perfect fluid that has no interactions with other particles or itself, beyond gravitational attraction. The quest for the identification of particle dark matter is looking for non-gravitational interactions of dark matter. While non-gravitational interactions with Standard Model particles can be searched for in the laboratory or by looking at the cosmic flux of SM particles with telescopes and cosmic ray detectors, dark matter self-interactions cannot be directly probed. Instead, we need to rely on cosmological and astrophysical signatures.

Excitingly, there is evidence in favor of non-gravitational interactions of dark matter in the form of self-interactions (for a review, see [66]). The ΛCDM paradigm is experiencing what is sometimes referred to as the "small scale crisis" [66], that is fuelled by the predictivity of CDM-only N-body simulations that generate universal, cuspy/singular "Navarro-Frenk-White"(NFW) dark matter density profiles for small and large dark matter halos alike [43, 44], with a large abundance of small dark matter halos [67]. The comparison of observations to CDM-only simulations leads to discrepancies that are significant enough to have been given names. They are briefly reviewed in the following, before addressing their relation to dark matter self-interactions.

1. *Missing satellites problem:* CDM-only simulations predict hundreds of dark matter subhalos massive enough to host dwarf galaxies in a galactic halo like that of the Milky Way, yet we know of only tens of dwarf satellite galaxies [68]. This problem has been historically important in the study of dark matter properties, but better understanding of suppression of star formation in small halos, combined with accounting for the imperfect completeness of surveys looking for dwarf galaxies have ameliorated the apparent discrepancy [69].

[1] Counterintuitively, for $m_{\rm WDM} \gtrsim$ keV, this makes warm dark matter actually rather cold in terms of temperature.

2. *Too-big-to-fail problem:* There is a lack of Milky Way satellites that can account for the largest subhalos expected for a Milky-Way-sized galaxy in CDM-only simulations (these halos would be too big to fail at becoming luminous galaxies, hence the name) [70, 71]. It is yet unclear whether accretion history and baryonic feedback can resolve this mismatch within the cold dark matter paradigm [72].

3. *Core-cusp problem:* CDM-only N-body simulations universally find cuspy DM halo profiles $\rho_{\rm DM} \propto r^{-1}$ [43, 44], while many measured rotation curves indicate density profiles with a constant density core $\rho_{\rm DM} \propto r^0$ (e.g. [73,74]). Violent baryonic processes have the potential to produce flat cores from cusps (e.g. [75]), but it has been argued that heavily dark matter dominated dwarf galaxies would still provide an environment to test CDM predictions (e.g. [76]).

4. *Diversity problem:* The universal density profiles found in CDM-only simulations [44], or predictive models of cored halos (e.g. from WDM) fail to accommodate the observed variation in density profiles in galactic interiors [77, 78].

These issues originally arose from comparison of observations to early CDM-only simulations. There is ongoing work to determine to what degree they are alleviated when baryonic processes such as violent disturbances of the gravitational potential by supernova explosions and stellar winds, suppression of galaxy formation by reionisation and tidal disruption of subhalos are taken into account [66].

It is an exciting possibility that these small scale issues are evidence of dark matter dynamics beyond gravitational interactions. In particular, they can be addressed in the context of self-interacting dark matter (SIDM) [66]. The dark matter collision rate per particle is given by $R_{\rm scatt} = \sigma_{2\to2} v_{\rm rel} \rho_{\rm DM}/m_{\rm DM}$ where $\rho_{\rm DM}$ and $m_{\rm DM}$ are the dark matter density and mass, while $\sigma_{2\to2}$ is the self-interaction cross section and $v_{\rm rel}$ the relative velocity of dark matter particles. The scaling with $\rho_{\rm DM}$ conserves the successes of cold dark matter in the formation of large scale structure (where the dark matter overdensity is not very large), while highly overdense regions in the centres of dark matter halos can be affected by large scattering rates [79]. In CDM halos, the central cusp is constituted by the lowest velocity dispersion/coldest dark matter particles. Collisions lead to heat transfer from the outer parts of the halo to the central region, turning the cusp into an isothermal core (solving the cusp-core problem) and lowering the central density (ameliorating the too-big-to-fail problem) [80]. Figure 4.1 shows results from [81], who compare a simple model for self-interacting dark matter halos to observations of cored galaxies and clusters. They model the SIDM halos by an inner isothermal core, induced by frequent self-interactions, matched to an outer halo following an NFW profile at a matching radius related to the rate of scattering $R_{\rm scatt} \times$ age $= 1$. The fits to cluster stellar dynamics data and galactic rotation curves determine the value of the self-interaction cross section at the characteristic collision velocity scale, finding that cored galaxies are explained by $\sigma/m \sim 1\,{\rm cm}^2/{\rm g}$, while galaxy clusters favour $\sigma/m \sim 0.1\,{\rm cm}^2/{\rm g}$ at larger characteristic velocities.

As an additional signature, self-interactions isotropise particle velocities and lead to more spherical halo shapes, possibly distinguishing them from CDM halos [82]. The diversity of dark matter halos can be enhanced by self-interactions: Core formation leaves them more susceptible to tidal mass loss in their individual environment, while the densest halos may undergo gravothermal collapse for cross sections $\sigma/m \gtrsim$ few $\,{\rm cm}^2/{\rm g}$ [83].

Even if not taking the small scale issues of ΛCDM seriously, the dark matter self-interaction cross section is a fundamental property of particle dark matter that is constrained

by astronomical observations. The most robust constraints on dark matter self-interactions are from colliding galaxy clusters. If dark matter interactions are frequent, they will act as a drag force on colliding dark matter halos, which will then lag behind the galaxies that are effectively collisionless due to the large distances between them. As most of the matter in the Universe is in the form of dark matter, this would lead to an offset between the center of the mass distributions of the colliding clusters (as inferred from gravitational lensing) and the center of the luminous galaxies constituting the clusters (as inferred from optical images). An analysis of the Bullet Cluster (fig. 3.2) finds an upper limit of $\sigma/m < 0.7\,\mathrm{cm}^2/\mathrm{g}$ [84], while a joint analysis of 30 merging galaxy cluster systems finds $\sigma/m < 0.47\,\mathrm{cm}^2/\mathrm{g}$ [37] (at 68%CL).

In summary, dark matter self-interactions can leave signatures in astrophysical settings if their cross section is large enough, potentially solving small scale issues of ΛCDM. They are bounded from above by observations of colliding galaxy clusters, indicating that the range of interesting self-interaction cross sections is

$$0.1\,\mathrm{cm}^2/\mathrm{g} \lesssim \frac{\sigma_{2\to2}}{m_{\mathrm{DM}}} \lesssim 1\,\mathrm{cm}^2/\mathrm{g}\,. \tag{4.5}$$

In this thesis, only velocity-independent cross sections are considered. Larger cross sections in small systems like dwarf galaxies are possible without violating the cluster constraints in models with velocity-dependent cross section (see Figure 4.1).

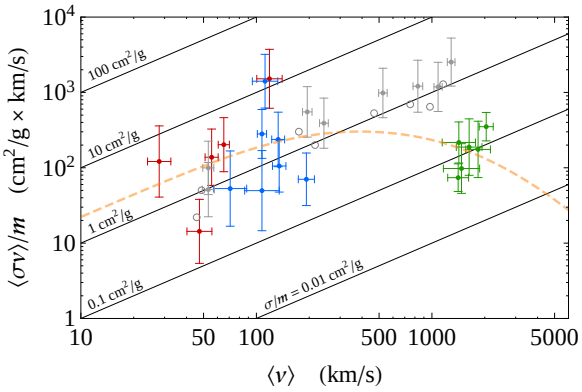

Figure 4.1: Velocity averaged dark matter self-interaction cross section determinations [81] from the core sizes of dark matter dominated galaxies (red, blue) and galaxy clusters (red), as well as from SIDM simulations with $\sigma/m = 1\,\mathrm{cm}^2/\mathrm{g}$ (gray). Diagonal lines indicate velocity-independent self-interaction cross sections, while the orange dashed line is an example for velocity dependent scattering via a light mediator. *Reprinted figure with permission from [81] Copyright (2016) by the American Physical Society.*

4.3 Dark matter indirect detection

Dark matter indirect detection refers to the search for non-gravitational interactions of particle dark matter in the cosmos, as opposed to *direct detection* of Galactic dark matter interacting with a detector in the laboratory. If dark matter consists of massive particles, transitions to lower mass states with large kinetic energy may be possible, either through decay of single dark matter particles or annihilation of multiple dark matter particles. While

decay is a generic expectation for a massive particle unless exactly forbidden by symmetry, dark matter annihilation plays a special role in the framework of WIMP dark matter, where the observed relic abundance implies a specific value of the thermally averaged annihilation cross section (see section 5.3, eqn. (5.45)), assuming standard cosmology.

If energetic Standard Model particles are produced in these processes, they may find their way to Earth and can be detected by cosmic ray detectors like AMS-02 [85], X-ray/gamma-ray telescopes like Fermi-LAT [86], or even neutrino telescopes (e.g. [87]). They may have even more indirect effects by modifying the ionization history of the Universe (e.g. [88]) or emitting radio waves as they encounter galactic magnetic fields (e.g. [89]). Non-observation of such signals can be used to constrain dark matter models, and positive observation of a highly specific signal would go a long way in identifying the nature of dark matter.

In all indirect searches, the potential dark matter signal has to compete with astrophysical backgrounds. In the Galaxy, supernova remnant shockwaves can accelerate the particles present in the interstellar gas to hundreds of TeV (for a review see e.g. [90]), and pulsars are now likewise understood to create and accelerate high energy electrons and positrons [91]. Different strategies are employed to separate astrophysical backgrounds from potential dark matter signals. Dark matter searches in antimatter cosmic rays (e.g. antiprotons) use the fact that there is no antimatter in the interstellar gas to be accelerated by astrophysical processes, while high energy particle physics processes typically distinguish very little between particles and antiparticles (e.g. [92]). Looking for larger antinuclei like antideuterons and antihelium additionally suppresses the background from antimatter production in cosmic ray collisions (e.g. [93, 94]). Dark matter has a different spatial distribution from that of baryons, which predicts characteristic spatial signatures (see e.g. [95]) and enables us to look for dark matter in places where little stellar activity is expected, like dwarf spheroidal galaxies (e.g. [96]). Finally, the energy spectra of particles produced in dark matter decay or annihilation and those accelerated by interstellar shockwaves or produced in cosmic ray collisions are very different. While the latter result in smooth, often soft power-law spectra, high energy particle physics processes generically produce harder spectra, potentially with sharp spectral features from kinematic cutoffs (for a review see e.g. [95]).

Gamma ray signals from Dark Matter

In this thesis, the focus is on gamma rays as messengers from dark matter annihilation and decay (for reviews, see e.g. [95, 97]). In contrast to charged cosmic rays that are deflected by magnetic fields, gamma rays point to their source, allowing to make use of spatial information to optimize the sensitivity of searches and test the dark matter origin of a possible signal. The detection of the gamma ray spectral features investigated in chapters 6 and 7 could have sufficient specificity to serve as compelling, "smoking-gun" evidence on non-gravitational interactions of dark matter.

Gamma ray telescopes measure the gamma ray flux $d\Phi/dE_\gamma$ in direction ψ given by

$$\frac{d\Phi}{dE_\gamma}(E_\gamma, \psi) = \frac{1}{4\pi} \int_{\text{l.o.s.}} ds\, Q\left(E_\gamma, \vec{r}(s, \psi)\right) , \tag{4.6}$$

integrating a source term $Q(E_\gamma, \vec{r}) = dN_\gamma / dE_\gamma\, dt\, dV$ over the line of sight. The source

terms from dark matter decay and annihilation are given by

$$Q_{\rm dec}(E,\vec{r}) = \Gamma_{\rm dec}\left(\frac{\rho_{\rm DM}(\vec{r})}{m_{\rm DM}}\right)\frac{dN_\gamma}{dE}\,, \tag{4.7}$$

$$Q_{\rm ann}(E,\vec{r}) = \langle\sigma v\rangle_{\rm ann}\left(\frac{\rho_{\rm DM}(\vec{r})}{m_{\rm DM}}\right)^2\frac{dN_\gamma}{dE}\,, \tag{4.8}$$

where $\Gamma_{\rm DM}$ is the dark matter decay rate into the channel of interest, and $\langle\sigma v\rangle_{\rm ann}$ is the velocity averaged annihilation cross section. If the latter is velocity-independent, this velocity averaged annihilation cross section corresponds to the thermally averaged annihilation cross section in the early Universe (eqn. (5.34)), providing a direct link between dark matter production in the WIMP paradigm and dark matter indirect detection. $\rho_{\rm DM}(\vec{r})$ is the dark matter mass density at position $\vec{r}$ along the line of sight, and dN_γ/dE is the gamma ray spectrum produced in a single decay/annihilation event. Both spatial and spectral information is used to separate astrophysical backgrounds from dark matter signals.

Targets for gamma ray dark matter searches Depending on the direction looked at in the sky, different contributions to the line of sight integral may dominate. Three contributions are of interest: that of the Milky Way dark matter halo, a contribution from localised sources of small angular diameter, and finally the isotropic cosmic gamma ray background. While the gamma ray flux from dark matter decay only depends on the line-of-sight integrated dark matter density, the flux from annihilation depends on the square of the density, favouring particularly overdense regions of the Universe as targets for gamma ray searches.

As we are situated within the Milky Way, there is always a contribution from our own dark matter halo. Different dark matter profiles are assumed in the literature to predict the gamma ray emission from the Galactic dark matter halo. Dark-matter-only simulations of galaxy formation find density profiles rising as a power law towards the center, like the Navarro-Frenk-White (NFW) profile [44] (see also section 4.2):

$$\rho_{\rm NFW}(\vec{r}) = \rho_\odot\frac{r_\odot}{|\vec{r}|}\frac{(1+r_\odot/r_s)^2}{(1+|\vec{r}|/r_s)^2}\,, \tag{4.9}$$

where $|\vec{r}|$ is the distance from the Galactic center and $r_s \sim 24\,\mathrm{kpc}$ is the scale radius characterising the profile, $\rho_\odot \simeq 0.3\,\mathrm{GeV/cm^3}$ is the dark matter density at the location of the Sun and $r_\odot = 8.5\,\mathrm{kpc}$ is the distance of the Sun from the Galactic center [98]. In the inner Galaxy, baryons have an important effect on galaxy formation, which in different hydrodynamical simulations is found to be able to steepen the slope of the dark matter density profile or conversely to lead to the formation of a constant-density core. This is a major uncertainty in the search for dark matter annihilation at the Galactic center, as the annihilation rate depends on the square of the density [99]. The Galactic center would be the brightest source of DM-produced gamma rays and as such is a promising target for dark matter indirect detection. There is ongoing debate around the *Galactic Center Excess* (e.g. [100]), which is an extended excess of $\sim$ few GeV gamma rays surrounding the Galactic center that is consistent with dark matter of masses in the tens of GeV annihilating into hadronically decaying SM particles with annihilation cross section close to the one naively expected for WIMPs. Advanced techniques of using spatial information have been employed to try to distinguish its possible DM origin from a contribution from unresolved point sources (e.g. [101–103]).

Weaker, but cleaner signals of dark matter annihilation or decay may come from dwarf spheroidal galaxies close to the Milky Way that have a large mass to light ratio, i.e. promise a large dark matter signal relative to little astrophysical background. Their angular extent is smaller than the resolution of current gamma ray telescopes, such that their dark matter content can be summarised by the line-of-sight integrated $\rho^2_{\rm DM}$, integrated over the solid angle $\Delta\Omega$ spanned by the dwarf galaxy (so-called *J-factors*). In contrast to the galactic center, which is limited by systematic uncertainty in the backgrounds, the search for dark matter annihilation in dwarf galaxies is mostly exposure limited [104].

Finally, for dark matter decay, which is not sensitive to the degree of clustering, there is a contribution to the gamma ray flux from the integrated emission throughout cosmic history, resulting in an isotropic extragalactic contribution to the flux

$$\frac{d\Phi^{\rm dec}_{\rm extragalactic}}{dE_\gamma}(E_\gamma) = \frac{1}{4\pi}\frac{\Omega_{\rm DM}\rho_c}{m_{\rm DM}}\int_0^\infty dz\,\frac{1}{H(z)}\frac{d\Gamma}{dE_\gamma}\left(E_\gamma(1+z)\right)e^{-\tau(E_\gamma,z)}\,, \tag{4.10}$$

accounting for the effect of redshift z [105]. Here $\Omega_{\rm DM}$ is the DM relic density in units of the critical density of the Universe ρ_c, H is the Hubble expansion rate (see section 2.2) and τ the optical depth.

The relations above correspond to the scenario where all dark matter decays or participates in annihilation. They are easily extended to the case where only a fraction of the dark matter decays or annihilates, by assuming that all dark matter components have the same spatial distribution, $\rho_i(\vec{r})/\rho_{\rm DM}(\vec{r}) = \Omega_i/\Omega_{\rm DM}$. This is expected for cold dark matter.

Discriminating dark matter signals in gamma ray spectra The gamma ray spectra predicted by dark matter processes can be strikingly different from those believed to be possible to create in astrophysical scenarios. Figure 4.2 shows several gamma ray spectra that can result from dark matter decay/annihilation, distinguishing between secondary gamma rays (gray) produced as final products from dark matter decay/annihilation into SM states that decay predominantly hadronically and distinctive gamma ray spectral features (colored) that can result in many models, either at leading order, or at loop-level.

These have to be contrasted with the leading astrophysical contributions. Known astrophysical point sources can be masked in searches for dark matter signals, but this is not possible for the diffuse gamma ray emission from cosmic ray interactions with the interstellar gas or magnetic and radiation fields. This diffuse emission needs to be modeled in detail [106] and subtracted from the data to enable the most sensitive searches for dark matter. At high energies $\gtrsim$ GeV, these backgrounds scale as power laws with $d\Phi_{\rm astro}/dE \sim E^{-\gamma}$ with spectral index $\gamma \gtrsim 2$, allowing dark matter signals to stand out.

When searching for sharp spectral features above a smooth astrophysical background, no detailed background modeling is necessary. A sliding energy window technique is often used, deriving constraints from small energy ranges around the spectral feature of interest by fitting a smooth power law background plus a sharp signal contribution (e.g. [107, 108]). A precise measurement would provide detailed kinematical information on the decay or annihilation process, such that gamma ray spectral features are not only a very clean signal, but also a rich one.

Ultimately, detection of dark matter annihilation or decay producing sharp photon spectra would result in a completely new tracer of dark matter in the Universe, and may allow to map the dark matter density in our own Galaxy [107, 109] and the cosmos.

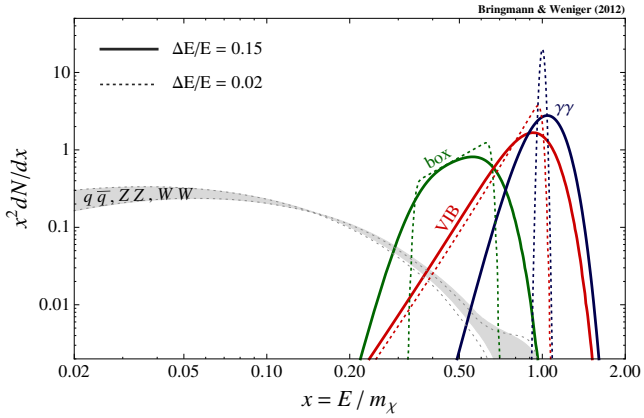

Figure 4.2: Example gamma ray spectra expected from dark matter decay/annihilation processes [95]. The gray band corresponds to the relatively featureless secondary gamma rays produced in annihilations/decays into unstable SM final states that decay predominantly hadronically. The coloured lines correspond to sharp spectral features, broadened by the energy resolution of the detector. Gamma ray lines (blue) are encountered in chapters 6 and 7, while the virtual internal bremsstrahlung feature (red) appears in section 7.2.2. The "box" spectral feature (green) can result from cascade decays, where the annihilation/decay produces an unstable particle that directly decays to two photons [95]. *Figure reprinted from [95].*

4.4 Laboratory probes of Dark Matter

Observing dark matter induced processes in a controlled environment on Earth would possibly be the most specific test of particle dark matter. On the flip side, this specificity makes the sensitivity and interpretation of laboratory tests very model dependent. Searches for particle dark matter on Earth take two forms: First, processes involving particle species that constitute dark matter can occur at general purpose particle physics experiments like the Large Hadron Collider, where specific search strategies have been developed to detect them. Second, *dark matter direct detection* (DMDD) experiments have been developed that seek to detect particles from the Galactic dark matter halo interacting in the detector. Further, precision tests in electroweak- and flavour physics play an important role in guiding the construction of viable dark matter models. They are not further discussed here, since they lack the specificity needed to positively identify dark matter.

Note that the discussion in this chapter is focused on WIMP dark matter and related models, and in particular dark matter models involving new light degrees of freedom have different signatures to those discussed here.

4.4.1 Dark matter at particle colliders

Dark matter searches at particle colliders have traditionally been dominated by searches for signatures of big visions of physics beyond the Standard Model, in particular for Supersymmetry (see [110] for an illustration). As the attractiveness of low-scale Supersymmetry as a solution to the electroweak hierarchy problem shrinks, there is growing interest in more model-independent signatures of BSM physics, including dark matter.

A systematic way of looking for signatures of WIMP dark matter at colliders is to study its production in an effective field theory (EFT) framework, yielding a limited number of

higher dimensional operators that can lead to dark matter production at colliders (e.g. [111]). Collider results on these operators can then be compared to the relic density expectation and contrasted with direct and indirect dark matter searches.

Such effective field theories that include only the dark matter particle as new degree of freedom are faithful simplifications of dark sectors in which all other particles of relevance are much heavier than the energy scales of interest. This may not be the case in dark matter production, if the dark sector contains particles close in mass to the DM candidate, or at the TeV-scale energies of the Large Hadron Collider. As a consequence, *simplified dark matter models* have been developed (e.g. [112,113]), which postulate a dark sector that next to the dark matter candidate contains just the minimal set of particles required to couple it to the Standard Model in the desired way. The aim of this is to search for realistic and specific dark matter signatures, while remaining as general as possible. In chapters 6 and 7, two examples of simplified dark matter models are extended by additional dark matter flavours, finding signatures that cannot appear in their minimal realisations.

The actual signatures looked for can be split into two groups. The first looks for dark matter production directly, the second constrains mediator particle properties. Dark matter candidates are neutral particles that leave no track in detectors. Still, the absence of energy deposition in the detector can be inferred from momentum conservation when precisely measuring the energies of all other products of a collision. At hadron colliders, this can only be done in the direction transverse to the beam, as the beam momentum fraction carried by the individual interacting partons in the beam direction is not known. The central dark matter observable in a hadron collision is hence the *missing transverse energy* $\not{E}_T$. For such events to be recorded, they must be visible to the detector trigger system, which cannot operate on missing energy/momentum alone. For the transverse momentum to be missing in the first place, it needs to recoil against something, which automatically provides a trigger signal. This can for instance be the initial state radiation of a gauge boson, resulting in *mono-X* $+\not{E}_T$ events (see e.g. [111]).

In many models, the dark matter particle is not the only new particle, and a new mediator particle charged under the SM gauge group plays an important role in determining the relic abundance. In scenarios of feebly coupled dark matter, the mediator may be the only particle that can be promptly produced at colliders at appreciable rates. If the mediator is not charged under a stabilising symmetry, it can be produced in a particle collision and decay again into SM particles via the interaction that formed it. Searches for e.g. di-jet resonances can be sensitive to this process (see e.g. [114]). If the mediator is charged under a stabilising symmetry, it needs to be pair-produced and will ultimately decay into the dark matter candidate. If this decay is prompt, as is typical in WIMP models, this results in missing energy plus SM particles with characteristic kinematic relations that can be used to increase sensitivity (see e.g. [115,116]). If the mediator has a macroscopic decay length $c\tau \gtrsim 1\,\text{mm}$, it can give rise to unique signatures with little Standard Model background, such as displaced vertices, disappearing tracks, and anomalous charged tracks (e.g. [113,117]).

A caveat in dark matter searches at colliders is that in the best case they can find proof of the existence of a somewhat stable, neutral massive particle. If its interactions can be measured precisely, conclusions about its plausible relic abundance may be drawn. But its cosmological stability cannot be tested, neither can its local abundance be determined without assumptions about cosmology. This highlights that, even though production at a collider may be the gold standard of discovering a new particle, the search for particle dark matter necessarily involves complementary approaches.

4.4.2 Direct detection of the Galactic dark matter halo in the laboratory

If the Galactic dark matter halo consists of particles χ, the interactions of these particles with Standard Model objects may be observable. *Dark matter direct detection* (DMDD) experiments look for scattering of Galactic halo dark matter off detector material by looking for the deposited recoil energy [118, 119]. The rate of $\chi T \to \chi T$ scattering events per unit target mass is given by

$$\frac{dR}{dE_R} = \frac{\rho_\chi}{m_T m_\chi} \int_{v_{\min}}^{\infty} dv\, v f(v) \frac{d\sigma_{\chi T \to \chi T}}{dE_R}(v, E_R)\,, \tag{4.11}$$

where the astrophysical quantities of the local DM-density ρ_χ and the dark matter speed distribution $f(v)$ in the laboratory frame enter, as well as the particle physics quantities related to the DM candidate χ and target T: m_χ and m_T are the DM and target masses respectively and $d\sigma_{\chi T \to \chi T}/dE_R$ is the elastic scattering cross section. The maximal recoil energy is given by

$$E_R \leq \frac{2\mu_T^2 v^2}{m_T}\,, \tag{4.12}$$

where $\mu_T = m_\chi m_T/(m_\chi + m_T)$ is the reduced mass of the DM-target system. The local dark matter density is of order $\rho_\chi \sim 0.3\,\mathrm{GeV/\,cm^3}$ and the speed distribution is characterised by the velocity distribution of the Galactic dark matter halo, which is often approximated as isothermal with characteristic speed $\sim 270\,\mathrm{km/s}$, to which the Solar system's speed relative to the DM halo ($\sim 220\,\mathrm{km/s}$) is added, modulated by the Earth's rotation around the Sun ($\sim 30\,\mathrm{km/s}$) [119].

These expressions already illuminate the current experimental situation: The search for WIMPs has been focused on electroweak-scale masses, accordingly choosing heavy elements like xenon as target material to optimise the available recoil energy, as well as maximise the possible coherence effect in spin-independent scattering, where $\sigma_{\mathrm{SI}} \sim A^2 \sigma_{\mathrm{nucleon}}$, with A the mass number of the target nucleus. This has led to tremendous success in constraining electroweak-scale dark matter that couples coherently to nucleons by ton-scale experiments sensitive to keV recoil energies (e.g. [120]), as long as the coupling is not suppressed e.g. by the dark matter velocity[2]. Complementary experiments target dark matter at lower masses by pushing sensitivities to lower E_R, as well as dark matter coupling to electrons or the spin of nuclei. Originally designed for WIMP searches, dark matter direct detection can also be sensitive to feebly coupled dark matter candidates in the case of light mediators [122].

The dark matter models considered in chapters 6, 7 and 8 of this thesis are generally not easy to probe by dark matter direct detection, either because they couple primarily to leptons and only at loop-level to nucleons, or because they are feebly coupled to heavy mediators.

[2] There is a positive signal from the DAMA/LIBRA experiment at high statistical significance [121]. This signal has not been corroborated by other experiments, making a dark matter interpretation difficult.

Chapter 5

Thermal Relics from the Early Universe

This chapter describes the evolution of particle populations that are governed by thermal processes, i.e. reactions between particles where at least one reactant is taken to follow an equilibrium phase space distribution. Section 5.1 introduces the equilibrium description of the thermal bath of Standard Model particles during the radiation era. Section 5.2 covers the Boltzmann equation that is used to determine the phase space distribution of particles that are not in equilibrium. These results are then used in sections 5.3 and 5.4 to analytically calculate the dark matter relic abundance in the minimal freeze-out and freeze-in scenarios. This lays the foundation for the calculation of thermal relic abundances in non-minimal dark sectors that is the topic of the remainder of this thesis.

5.1 Equilibrium thermodynamics in the expanding Universe

In general, a population of particles of some particle species is described by its phase space distribution $f(\vec{x}, \vec{p})$, which in a homogeneous, isotropic setting only depends on $p = |\vec{p}|$. For a dilute gas of these particles, with g internal degrees of freedom, the number density n, energy density ρ and pressure $\mathcal{P}$ are given by [1]

$$n = \frac{g}{(2\pi)^3} \int f(\vec{p}) d^3p \tag{5.1}$$

$$\rho = \frac{g}{(2\pi)^3} \int E(\vec{p}) f(\vec{p}) d^3p \tag{5.2}$$

$$\mathcal{P} = \frac{g}{(2\pi)^3} \int \frac{|\vec{p}|^2}{3E(\vec{p})} f(\vec{p}) d^3p \,, \tag{5.3}$$

with $E^2 = m^2 + |\vec{p}|^2$. If momentum transfer among the particles is frequent (i.e. fast compared to the Hubble rate), *kinetic equilibrium* holds, and the phase space distribution is given by the Fermi-Dirac or Bose-Einstein distributions for fermionic (+) or bosonic (−) particles respectively:

$$f(\vec{p}) = \frac{1}{e^{(E-\mu)/T} \pm 1} \,, \tag{5.4}$$

characterised by the particle's mass m, the temperature T and chemical potential μ. In the relativistic limit, for $T \gg m, \mu$, this results in

$$n = \begin{cases} (\zeta(3)/\pi^2) g T^3 & \text{bosons} \\ (3/4)(\zeta(3)/\pi^2) g T^4 & \text{fermions} \end{cases} \tag{5.5}$$

$$\rho = \begin{cases} (\pi^2/30) g T^4 & \text{bosons} \\ (7/8)(\pi^2/30) g T^4 & \text{fermions} \end{cases} \tag{5.6}$$

$$\mathcal{P} = \rho/3\,, \tag{5.7}$$

while for the non-relativistic limit, $T \ll m$, the distribution function approaches the Maxwell-Boltzmann distribution for both bosons and fermions, resulting in

$$n = g \left(\frac{mT}{2\pi}\right)^{3/2} \exp\left[-(m-\mu)/T\right] \tag{5.8}$$

$$\rho = mn \tag{5.9}$$

$$\mathcal{P} = nT\,. \tag{5.10}$$

If one assumes Maxwell-Boltzmann statistics, eqn. (5.1) has a simple expression in terms of modified Bessel functions $K_n(x)$ in thermal equilibrium:

$$n_{\mathrm{MB}} = g \frac{m^2 T}{\pi^2} K_2\left(\frac{m_\chi}{T}\right)\,. \tag{5.11}$$

If there are multiple species i, their temperatures T_i are equal if they are in kinetic equilibrium with each other. In addition, if interactions that, for example, change particles i and j into particles k and l (and vice versa), are frequent, *chemical equilibrium* holds and relates the chemical potentials to one another,

$$i + j \leftrightarrow k + l \quad \text{frequent} \quad \Rightarrow \quad \mu_i + \mu_j = \mu_k + \mu_l\,. \tag{5.12}$$

From eqns. (5.6), (5.9), it is clear that relativistic species dominate the energy density in the Universe, unless there are large chemical potentials $\mu_i \sim m_i$. It is then convenient to summarise all particle species with $\mu_i \ll m_i$ into a thermal bath of temperature T with an energy density of

$$\rho_R = \frac{\pi^2}{30} g_{\mathrm{eff}}(T) T^4\,, \tag{5.13}$$

where $g_{\mathrm{eff}}(T)$ is the *effective number of degrees of freedom* compared to a massless boson at temperature T [123]:

$$g_{\mathrm{eff}}(T) = \left(\sum_{\text{species } i} \frac{g_i}{(2\pi)^3} \int f_i(\vec{p}) E_i(\vec{p})\, d^3p \right) \Bigg/ \left(\frac{\pi^2}{30} T^4 \right) \tag{5.14}$$

yielding the familiar approximate expression counting only relativistic species with $m_i \ll T$:

$$g_{\mathrm{eff}}(T) = \sum_{i \in \text{rel. bosons}} g_i \left(\frac{T_i}{T}\right)^4 + \frac{7}{8} \sum_{i \in \text{rel. fermions}} g_i \left(\frac{T_i}{T}\right)^4\,. \tag{5.15}$$

For the thermal bath of Standard Model particles, the evolution of T_i can be calculated, and tabulated values for $g_{\mathrm{eff}}(T)$ are available [123]. It varies from $g_{\mathrm{eff}} = 106.75$ at $T \geq m_{\mathrm{top}}$

to $g_{\text{eff}}(10\,\text{MeV} \gtrsim T \gtrsim 1\,\text{MeV}) = 10.75$ before and $g_{\text{eff}}(T \ll 1\,\text{MeV}) = 3.36$ after neutrino decoupling. When ρ_R dominates the energy density, eqn. (5.13) and the Friedmann eqn. (2.4) yield a simple expression for the Hubble rate during the radiation era:

$$H = \underbrace{\sqrt{\frac{8\pi^3}{90}}}_{\simeq 1.66} g_{\text{eff}}^{1/2}(T)\frac{T^2}{m_{\text{Pl}}}. \tag{5.16}$$

When calculating relic densities, conserved quantities are useful to relate yields at time of production to the relic density today. In thermal equilibrium (which is a good approximation for the SM bath), the entropy S contained in a comoving volume V is constant. This means the *entropy density* $s \equiv S/V$ scales as

$$s \equiv \frac{S}{V} = \frac{\rho + \mathcal{P}}{T} \propto R^{-3}\,, \tag{5.17}$$

no matter whether the particles constituting the thermal bath are relativistic or not. In analogy to the formula for the density eqn. (5.13), the entropy density of a thermal bath of temperature T can be written in terms of an effective number of relativistic bosonic degrees of freedom in the bath,

$$s = \frac{2\pi^2}{45} h_{\text{eff}}(T) T^3 \tag{5.18}$$

with number of relativistic degrees of freedom relevant to the entropy density [123]

$$h_{\text{eff}}(T) = \left(\frac{1}{T} \sum_{\text{species } i} \frac{g_i}{(2\pi)^3} \int f_i(\vec{p}) \left(E_i(\vec{p}) + \frac{|\vec{p}|^2}{3E_i(\vec{p})} \right) d^3p \right) \Bigg/ \left(\frac{2\pi^2}{45} T^3 \right) \tag{5.19}$$

$$\simeq \sum_{i \in \text{rel. bosons}} g_i \left(\frac{T_i}{T} \right)^3 + \frac{7}{8} \sum_{i \in \text{rel. fermions}} g_i \left(\frac{T_i}{T} \right)^3 . \tag{5.20}$$

The entropy density has two important uses in the calculation of relic densities. First, the relations (5.17) and (5.18) determine the evolution of the temperature $T(R)$ of an adiabatically expanding population of particles as a function of the scale factor as $T \propto h_{\text{eff}}^{-1/3} R^{-1}$. While h_{eff} is constant, this leads to $T \propto R^{-1}$ expected from simple redshifting of relativistic momenta. Whenever a particle species is becoming non-relativistic, h_{eff} decreases, and T drops slightly more slowly, as the energy density stored in the non-relativistic species is converted into relativistic particles. In the Standard Model, this leads to a slightly colder relic population of neutrinos, which decouple from the rest of the thermal bath before the electrons become non-relativistic and heat the remaining photon bath. More extreme consequences are found in SIMP models of dark matter, explored in chapter 8.

Second, just as the total entropy S of the SM bath is conserved through the expansion of the Universe, so is the total number of relic particles N_i in that volume, if there are no processes that convert these particles into others. This lends special utility to the *abundance* Y_i of a species i, defined as

$$Y_i \equiv \frac{N}{S} = \frac{n_i}{s}\,. \tag{5.21}$$

Using that the entropy density today is [5]

$$s_0/k_B = 2891.2\,\text{cm}^{-3}\,, \tag{5.22}$$

the observed relic density today (eqn. (2.13)) requires that a dark matter species with mass $m_{\rm DM}$ has the relic abundance

$$Y_{\rm DM}^{\rm observed} = 4.35 \cdot 10^{-10} \left(\frac{m_{\rm DM}}{\rm GeV}\right)^{-1} . \tag{5.23}$$

In the absence of injections of large amounts of entropy into the thermal bath, this number stays constant between the epoch that determines the relic density and the epoch at which it is measured, e.g. at the time of CMB decoupling. Further, unless dark matter is very light, this is a small number. The basic task of dark matter production mechanisms is to reproduce this small number.

5.2 The early Universe dropping out of thermal equilibrium

Particles in the thermal plasma can be conveniently characterised by the equilibrium relations above. This section introduces the standard treatment of the evolution of particle populations that are governed by their connection to a thermal bath, but not actually in equilibrium [1, 124].

The Boltzmann equation describes the rate of change in the population of a particle due to motion/dilution, as well as creation and destruction and is in general given by [1]

$$\hat{\mathbf{L}}\left[f\right] = \hat{\mathbf{C}}\left[f\right] \tag{5.24}$$

with $\hat{\mathbf{L}}$ the Liouville operator that describes the rate of change in the phase space density and $\hat{\mathbf{C}}$ the collision operator that describes the rate of particles added or lost per phase space volume and time, acting on the phase space distribution $f(p^\mu, x^\mu)$. In the FRWL model, the Liouville operator reads [1]

$$\hat{\mathbf{L}}\left[f(E,t)\right] = E\frac{\partial f}{\partial t} - H|\vec{p}|^2\frac{\partial f}{\partial E} \tag{5.25}$$

The general equation (5.24) can be simplified considerably if the particle species under consideration is in kinetic equilibrium with itself at temperature $T(t)$, and the phase space distribution f is given by its equilibrium Fermi-Dirac or Bose-Einstein distribution $f_{\rm eq}^{\rm FD/BE}$ determined by $n(t)$ and $T(t)$ (see e.g. [125] for a study that goes beyond this standard assumption and solves the un-integrated Boltzmann equation numerically). The Boltzmann equation (5.24) can then be integrated over invariant phase space

$$d\Pi \equiv \frac{g}{(2\pi)^3}\frac{d^3p}{2E} \tag{5.26}$$

resulting in (using the relation between n and f eqn. (5.1)):

$$\frac{dn_\chi}{dt} + 3Hn_\chi = \frac{g}{(2\pi)^3}\int \frac{d^3p}{E}\hat{\mathbf{C}}\left[f_\chi(E,t)\right] , \tag{5.27}$$

where from now we refer to the particle of interest as χ. The collision term has contributions from all possible collision processes. For the integrated collision term, only inelastic processes are relevant. As an example that is straightforward to generalise, we look at the integrated collision term for a process $\chi + b \to i + j$, which is given by

$$\begin{aligned}\frac{g}{(2\pi)^3}\int \frac{d^3p_\chi}{E_\chi}\hat{\mathbf{C}}\left[f_\chi(E,t)\right] = -\int d\Pi_\chi\, d\Pi_b\, d\Pi_i\, d\Pi_j\, (2\pi)^4\, \delta^4\left(p_\chi + p_b - p_i - p_j\right) |\mathcal{M}|^2_{\chi+b\to i+j} \\ \times \left[f_\chi f_b(1 \pm f_i)(1 \pm f_j) - f_i f_j (1 \pm f_\chi)(1 \pm f_b)\right] ,\end{aligned} \tag{5.28}$$

where we have assumed for simplicity that the process under consideration is CP-invariant (i.e. $|\mathcal{M}|^2_{\chi+b\to i+j} = |\mathcal{M}|^2_{i+j\to\chi+b}$), as will be the case for all processes considered in this work. Note that if $\mathcal{M}$ depends on spin or polarisation of some of the particles involved, the number of internal degrees of freedom g in $d\Pi$ (eqn. (5.26)) needs to be replaced here by an explicit summation over these internal degrees of freedom.

At this point, it is common to approximate all distribution functions f_i by the Maxwell Boltzmann distribution [1, 17, 124],

$$f(E) \to e^{\mu/T} e^{-E/T} \,. \tag{5.29}$$

This restricts the applicability of the equations below to the non-relativistic case, where $T \ll E - \mu$, as e.g. is the case for standard WIMP freeze-out.[1] We can then ignore the final state enhancement/suppression factors $(1 \pm f)$ and use

$$f(E,t) = \frac{n(t)}{n^{\rm eq}(t)} f^{\rm eq}_{\rm MB}(E,t)\,, \tag{5.30}$$

with $f^{\rm eq}_{\rm MB}(E,t)$ and $n^{\rm eq}(t)$ the equilibrium Maxwell-Boltzmann phase space distribution and number density respectively at temperature $T(t)$. This considerably simplifies the collision term, as the last term of eqn. (5.28) now reads (using energy conservation $E_\chi + E_b = E_i + E_j$)

$$e^{-(E_\chi+E_b)/T}\left(\frac{n_\chi n_b}{n^{\rm eq}_\chi n^{\rm eq}_b} - \frac{n_i n_j}{n^{\rm eq}_i n^{\rm eq}_j}\right) . \tag{5.31}$$

We define the *thermally averaged cross section* $\langle\sigma v\rangle$ as

$$\begin{aligned}\langle\sigma v\rangle_{\chi+b\to i+j} \equiv \frac{1}{n^{\rm eq}_\chi n^{\rm eq}_b}\int d\Pi_\chi\, d\Pi_b\, d\Pi_i\, d\Pi_j\, e^{-(E_\chi+E_b)/T} \\ (2\pi)^4\,\delta^4\left(p_\chi + p_b - p_i - p_j\right)|\mathcal{M}|^2_{\chi+b\to i+j}\end{aligned} \tag{5.32}$$

Apart from the integration over initial state phase space, this is very similar to that for the cross section

$$\sigma \equiv \frac{1}{2E_\chi 2E_b|\vec{v}_\chi - \vec{v}_b|}\int d\Pi_i\, d\Pi_j\,(2\pi)^4\,\delta^4\left(p_\chi + p_b - p_i - p_j\right)|\mathcal{M}|^2_{\chi+b\to i+j}\,, \tag{5.33}$$

defined for collinear $\vec{v}_\chi || \vec{v}_b$. This allows to write $\langle\sigma v\rangle$ as a thermal average of the cross section [124]

$$\langle\sigma v\rangle = \frac{1}{n^{\rm eq}_\chi n^{\rm eq}_b}\int d^3p_\chi\, d^3p_b\, \sigma v_{\rm M\o l} e^{-(E_\chi+E_b)/T}, \tag{5.34}$$

where the occurrence of the Møller velocity $v_{\rm M\o l} = \sqrt{|\vec{v}_\chi - \vec{v}_b|^2 - |\vec{v}_\chi \times \vec{v}_b|^2}$ accounts for the transverse boost by $|\vec{v}_\chi \times \vec{v}_b|/|\vec{v}_\chi - \vec{v}_b|$ of the colliding system wrt. the plasma rest frame.

In summary, assuming kinetic equilibrium and approximating all particle statistics as Maxwell-Boltzmann distributed, the evolution of the χ-population is governed by

$$\frac{dn_\chi}{dt} + 3Hn_\chi = -\langle\sigma v\rangle_{\chi+b\to i+j}\left(n_\chi n_b - n^{\rm eq}_\chi n^{\rm eq}_b \frac{n_i n_j}{n^{\rm eq}_i n^{\rm eq}_j}\right) + \cdots\,, \tag{5.35}$$

[1] Recently, methods have been developed to go beyond this approximation [126–129], enabling the treatment of relativistic freeze-out/freeze-in, as well as capturing the effect of the final state enhancement/suppression factors.

where $\cdots$ refers to all other processes that can convert sets of particles $\{\chi, a, b, \dots\}$ to $\{i, j, \dots\}$, for which these expressions are easily generalised. The Boltzmann equation can be conveniently written in terms of the abundance Y by dividing eqn. (5.35) by $S = R^3 s$ and noting that S is conserved in time:

$$\frac{dY_\chi}{dt} = -s\langle\sigma v\rangle_{\chi+b\to i+j}\left(Y_\chi Y_b - Y_\chi^{\rm eq} Y_b^{\rm eq}\frac{Y_i Y_j}{Y_i^{\rm eq} Y_j^{\rm eq}}\right) + \cdots \tag{5.36}$$

Further, as $\langle\sigma v\rangle$ and $Y^{\rm eq}$ depend directly on the bath temperature T and only indirectly on time, it is convenient to use the dimensionless temperature parameter $x = m/T$ as evolution parameter (m can be any mass, conventionally $m_{\rm DM}$ is used). First converting from t as evolution parameter to R and then using $sR^3 = \text{const.}$ to convert to x, one finds [124, 125]

$$\frac{dY_\chi}{dx} = -\frac{s\langle\sigma v\rangle_{\chi+b\to i+j}}{x\tilde{H}}\left(Y_\chi Y_b - Y_\chi^{\rm eq} Y_b^{\rm eq}\frac{Y_i Y_j}{Y_i^{\rm eq} Y_j^{\rm eq}}\right) + \cdots, \tag{5.37}$$

with $\tilde{H} = H/\tilde{g}$, where $\tilde{g} = 1 + \frac{1}{3}\frac{T}{h_{\rm eff}}\frac{dh_{\rm eff}}{dT}$ accounts for the change of $h_{\rm eff}$ with temperature.

This concludes the review of standard techniques in tracking particle abundances in the early Universe. In the following two sections, the relic abundances in two generic minimal dark matter production scenarios are calculated analytically, first for a dark matter candidate that starts out in thermal equilibrium with the SM bath (sec. 5.3), then in the scenario where dark matter is produced through rare reactions of bath particles and never equilibrates with the visible sector.

5.3 Freeze-out of WIMP dark matter

Weakly Interacting Massive Particle dark matter in this thesis refers to a class of dark matter models defined by the production mechanism of thermal freeze-out through $2 \to 2$ annihilations. In the following, the general abundance evolution equations of the previous sections are particularised to the case of a WIMP dark matter candidate χ. A $\mathbb{Z}_2$ symmetry under which χ is odd and all SM particles are even is introduced to stabilise the dark matter candidate. This implies that only annihilation reactions $\chi\chi \leftrightarrow XY$ into SM particles X and Y can affect the dark matter abundance.[2] The Boltzmann equation (5.37) can then be written as [1]

$$\frac{x}{Y_\chi^{\rm eq}}\frac{dY_\chi}{dx} = -\frac{n_\chi^{\rm eq}\langle\sigma v\rangle}{\tilde{H}}\left(\left(\frac{Y_\chi}{Y_\chi^{\rm eq}}\right)^2 - 1\right), \tag{5.38}$$

where $\langle\sigma v\rangle$ is the thermally averaged annihilation cross section, summing over all channels $\chi\chi \to XY$. This form of the Boltzmann equation illustrates that Y_χ will be kept close to its equilibrium value $Y_\chi^{\rm eq}$ as long as the equilibrium annihilation rate $n_\chi^{\rm eq}\langle\sigma v\rangle$ is larger than the Hubble rate H. In the WIMP paradigm, $\langle\sigma v\rangle$ is large enough for this to be ensured at $T > m_\chi$. The typical behaviour of $Y_\chi^{\rm WIMP}(x)$ governed by eqn. (5.38) is illustrated in figure 5.1, and discussed analytically in the following.

The time when the annihilation rate per particle drops below the expansion rate

$$n_\chi(x_{\rm fo})\langle\sigma v\rangle(x_{\rm fo}) \simeq H(x_{\rm fo}) \tag{5.39}$$

[2] (Inverse) decay $X \leftrightarrow \chi\chi$ of a heavy $\mathbb{Z}_2$-even particle X with $m_X > 2m_\chi$ can also affect the abundance, but is not of relevance in the WIMP setup, due to becoming Boltzmann suppressed earlier.

marks the *freeze-out* of χ, since Y_χ only changes little thereafter. Two cases can be distinguished, depending on whether χ is relativistic or non-relativistic at the time of freeze out. In the relativistic case, Y_χ freezes at its relativistic equilibrium value

$$Y_\chi^{\mathrm{eq,rel}} = \frac{n^{\mathrm{eq,rel}}(T_{\mathrm{fo}})}{s(T_{\mathrm{fo}})} \sim 0.42 \cdot h_{\mathrm{eff}}^{-1}(T_{\mathrm{fo}})\,, \tag{5.40}$$

using eqns. (5.5) and (5.18) for $n^{\mathrm{eq,rel}}(T)$ and $s(T)$. Using eqn. (5.23) for the relic abundance corresponding to the observed dark matter density gives

$$\frac{\Omega_{\chi,\mathrm{HDM}}}{\Omega_{\mathrm{DM,obs}}} = 0.96 \left(\frac{m_\chi}{\mathrm{eV}}\right) h_{\mathrm{eff}}^{-1}(T_{\mathrm{fo}})\,, \tag{5.41}$$

and substituting the maximal $h_{\mathrm{eff}}^{\mathrm{max}} = 106.75$ attainable in the SM plasma into eqn. (7.8) results in an upper bound on the dark matter mass $m_\chi^{\mathrm{HDM}} \lesssim 110\,\mathrm{eV}$ from overabundance. Relativistic freeze out does not result in cold WIMPs, but in *hot dark matter* (HDM) with large velocity dispersion due to its small mass. This smoothes out primordial fluctuations in the matter density (see section 4.1) and is incompatible with the amount of structure observed in the Universe [130], such that a hot dark matter component may make up at most a small fraction of the observed dark matter density [63, 131].

Non-relativistic freeze out can allow for much heavier, cold dark matter: Eqn. (5.23) then implies that the dark matter abundance today needs to be much smaller than $Y_\chi^{\mathrm{eq,rel}}$. To achieve this in the WIMP scenario, the interaction $\langle\sigma v\rangle$ needs to be large enough to keep Y_χ close to its equilibrium value to late times $T \ll m_\chi$ when Y_χ^{eq} becomes strongly Boltzmann suppressed (eqn. 5.8). Simple estimates on the relic density today can then be made using the instantaneous freeze-out approximation

$$Y_\chi|_{\mathrm{today}} \simeq Y_\chi(x_{\mathrm{fo}}) \simeq Y_\chi^{\mathrm{eq}}(x_{\mathrm{fo}})\,. \tag{5.42}$$

Expanding $\langle\sigma v\rangle$ in terms of its velocity dependence[3] $\langle\sigma v\rangle \equiv \langle\sigma v\rangle_0 x^{-n}$, this results in the relic density

$$\Omega_{\mathrm{WIMP}} \simeq \frac{\sqrt{45/\pi}\sqrt{g_{\mathrm{eff}}(x_f)}x_f^{1+n}}{h_{\mathrm{eff}}(x_f)m_{\mathrm{Pl}}\langle\sigma v\rangle_0} s_0 \rho_c^{-1}\,, \tag{5.43}$$

which is inversely proportional to $\langle\sigma v\rangle_0$ (see fig. 5.1 for illustration) and independent of m_χ, up to a logarithmic dependence of the freeze-out time x_f on these parameters:

$$x_f = \log\left[\sqrt{\frac{45}{32\pi^6}}\left(g_\chi/g_{\mathrm{eff}}(x_f)^{1/2}\right) m_{\mathrm{Pl}} m \langle\sigma v\rangle_0\right] + (1/2 - n)\log(x_f)\,, \tag{5.44}$$

which is determined by the naive freeze-out condition eqn. (5.39), with typical values $x_f \sim 20 - 30$. Equation (5.43) leads to the generic prediction of the WIMP paradigm for the thermally averaged cross section at the time of freeze-out

$$\langle\sigma v\rangle_{\mathrm{WIMP}} \simeq (2 \sim 3) \times 10^{-26}\,\mathrm{cm}^3/\mathrm{s}\,, \tag{5.45}$$

fairly independently from the dark matter mass (for a more elaborate analytical treatment see for example [1,132]). In the case where σv is velocity independent, this directly translates

[3] Here $n = 0$ corresponds to s-wave annihilation with $\sigma v \propto v^0$, and $n = 1$ to p-wave annihilation with $\sigma v \propto v^2$, since $\langle v\rangle \sim T^{1/2}$ at non-relativistic velocities [1].

into a sensitivity target for searches for dark matter annihilation today, where this value is also referred to as the *thermal* value for the cross section.

Before discussing implications of this result, it is prudent to recall the assumptions made: The calculation assumed standard cosmology, implying that the expansion of the Universe was governed by the adiabatically expanding SM radiation bath (eqn. (5.16)). The earliest data underpinning standard cosmology is from neutrino decoupling and BBN at $T \sim 1\,\mathrm{MeV}$, and the WIMP calculation extrapolates this to temperatures $T > m_\chi/x_f$, about which little is known for certain. This uncertainty needs to be kept in mind when making claims about whether a particular model is ruled out by relic density constraints (see e.g. [133]).

The fact that $\langle\sigma v\rangle_{\mathrm{WIMP}} \simeq 2\times10^{-9}\,\mathrm{GeV}^{-2}$ can naturally result in extensions of the Standard Model drafted to explain the origin of the electroweak scale by introducing 100 GeV – TeV scale new particles with electroweak-strength couplings has been referred to as the "WIMP-miracle". In this thesis, "weakly interacting massive particle" is used generally to refer to dark matter produced by non-relativistic thermal freeze-out via $2 \to 2$ annihilations, with no relation to the electroweak forces in the Standard Model implied [59].

The production mechanism not only predicts the annihilation cross section, but also the possible mass range of WIMP dark matter: First, there is a theoretical upper limit on the WIMP mass, $m_{\mathrm{WIMP}} \lesssim \mathcal{O}(100)\,\mathrm{TeV}$ from unitarity of the annihilation cross section [134, 135]. Second, a lower limit follows from cosmological observations of the relative energy content in photons and neutrinos that would be changed if dark matter annihilations after neutrino decoupling at $T_D \sim$ MeV heat the photons or neutrinos (or inject energy into other non-interacting dark radiation), implying $m_{\mathrm{WIMP}} \gtrsim \mathcal{O}(1)\,\mathrm{MeV}$ [136].

There are various exceptions to the calculation of the thermal relic abundance presented here, that can arise when there are more than one particle species in the dark sector (chapter 7, see e.g. [137]) or the stabilising symmetry is less minimal than the $\mathbb{Z}_2$ dark parity assumed here (which, for example, could lead to a conserved dark matter particle-antiparticle asymmetry, see e.g. [60]). Another option is that $\chi\chi \to \mathrm{SM\,SM}$ annihilations are not the dominant dark matter depletion mechanism, but instead number changing interactions $\chi\chi\chi(\chi) \to \chi\chi$ are responsible for reducing the DM abundance (e.g. [8, 9]). An example of this is studied in chapter 8.

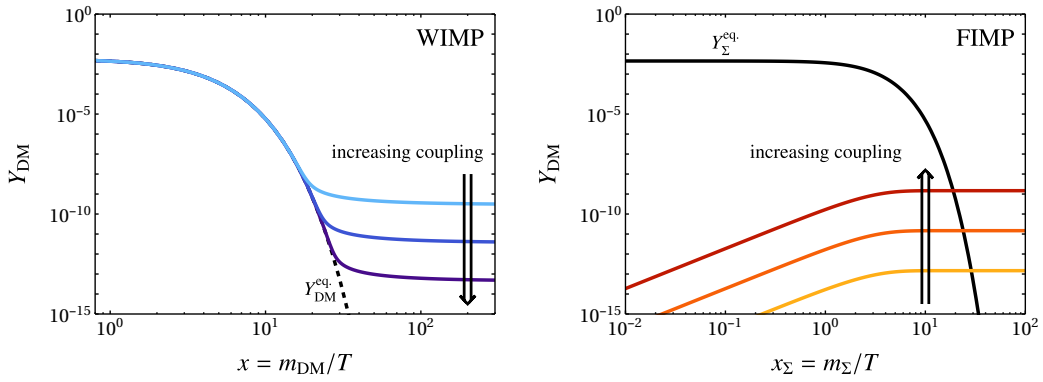

Figure 5.1: Characteristic abundance evolution during WIMP *(left)* and FIMP *(right)* production, illustrating the dependence on the coupling strength $Y_{\mathrm{WIMP}} \propto \langle\sigma v\rangle^{-1}$ and $Y_{\mathrm{FIMP}} \propto \Gamma_{\Sigma\to\mathrm{FIMP}}$.

5.4 Freeze-in of FIMP dark matter

Freeze-in [7] of "feebly interacting massive particle" (FIMP) dark matter is a scenario of dark matter production, where the relic abundance is calculable from thermal processes in the early Universe, but the dark matter candidate is never in thermal equilibrium. In contrast to freeze-out of WIMP dark matter, it is assumed that an initially negligible abundance of dark matter particles is increased gradually in the early Universe, through a coupling so "feeble" that the dark matter species never reaches equilibrium with the Standard Model bath.

The basic freeze-in mechanism is the same for all FIMP scenarios considered in this work and is recapitulated here for a general dark matter candidate ψ coupled to a standard model particle X and a heavy mediator particle Σ which we assume to be in thermal equilibrium with the Standard Model bath.[4] Freeze-in production assumes that ΛCDM cosmology with a thermal bath of Standard Model particles correctly describes nature up to temperatures of order of the dark matter candidate mass m_ψ and the mass m_Σ of the bath particle it interacts with. Additionally, it assumes that any initial or non-thermally produced abundance of the DM candidate is negligible compared to the observed dark matter abundance. This is in contrast to the WIMP mechanism, in which thermalisation of the dark matter candidate erases any previous history.

The time evolution of the dark matter number density is described by the integrated Boltzmann equation (see sec. 5.2):

$$\frac{dn_\psi}{dt} + 3Hn_\psi = C_{1\to 2} + C_{2\to 2} \,, \tag{5.46}$$

where H is the Hubble expansion rate, while $C_{1\to 2}$ and $C_{2\to 2}$ are collision terms accounting for $1 \to 2$ decay processes (such as $\Sigma \to \psi X$) and $2 \to 2$ scattering processes (such as $\Sigma X \to \psi X'$) respectively. Processes with larger number of final states become increasingly irrelevant in a perturbative theory. For simplicity, we assume that the phase space distributions for all particles except for the dark matter candidate and the mediator follow a Maxwell-Boltzmann distribution.[5] The $2 \to 2$ collision term $C_{2\to 2}$ is then the same as in eqn. (5.35), cast in terms of thermally averaged cross sections $\langle \sigma v \rangle_{ab\to\psi X}$, and the $C_{1\to 2}$ collision term (cf. eqn. 5.28) describing Σ decay can be cast as

$$C_{1\to 2}^{\text{feeble}} = \sum_X \int \frac{d^3 p_\Sigma}{(2\pi)^3} \frac{g_\Sigma f_\Sigma \Gamma_{\Sigma\to X\psi}}{E_\Sigma / m_\Sigma} \,, \tag{5.47}$$

where g_Σ and f_Σ are the number of degrees of freedom and the phase space density distribution of the particle Σ, respectively and $\Gamma_{\Sigma\to X\psi}$ is the decay rate for the process $\Sigma \to X\psi$. Here we have also used that the inverse process $\psi X \to \Sigma$ can be neglected, as the FIMP

[4] Note that three somewhat different freeze-in scenarios are possible, and many comments in this section do not apply to them: The first is freeze-in via a $\mathbb{Z}_2$-even light mediator, like a dark photon, see e.g. [138,139]. A second is when the dark matter candidate is not stabilised by a conserved symmetry and mixes with a SM particle, which is the case for sterile neutrinos, see e.g. [57]. The third is often called "UV freeze-in", where the feeble coupling is generated by a non-renormalisable interaction. In this case, the relic abundance is dominated by production at the highest temperatures, i.e. it depends on the reheating temperature and possible production during inflation [7]. The gravitino in supersymmetry is an example of this [56]. This thesis takes "freeze-in" to refer to IR-calculable production mechanisms only.

[5] The effects of the Bose/Fermi enhancement/suppression factors for the FIMP relic abundance have been discussed in [126] and can modify the results by $\mathcal{O}(1)$ factors. These do not result in qualitative differences in the case of FIMP production dominated by heavy particle decay.

number density n_ψ is by assumption much smaller than its equilibrium value while production is efficient.

When decay production via $\Sigma \to \psi X$ is kinematically allowed, it typically dominates over $2 \to 2$ production [7, 138] (see however [126, 140, 141]). In this case, the Boltzmann equation (5.46) can be rewritten as [7]

$$\frac{dY_\psi}{dx} = \sum_X \frac{g_\Sigma}{xH(T)s(T)} \Gamma_{\Sigma\to\psi X} \int \frac{d^3p_\Sigma}{(2\pi)^3} \frac{m_\Sigma}{E_\Sigma} f_\Sigma(p_\Sigma, T) \,, \tag{5.48}$$

in terms of the dimensionless abundance $Y \equiv n/s$ and temperature parameter $x \equiv m_\Sigma/T$ as introduced in section 5.2. The abundance evolution is illustrated in fig. 5.1.

Assuming that the effective number of degrees of freedom in the Standard Model bath does not vary during the epoch when FIMP production is most efficient, $T_{\rm prod} \sim \mathcal{O}(1) \times \max(m_\Sigma, m_\psi)$, this can be integrated to give the present relic abundance:

$$Y_\psi^{\rm today} = \frac{g_\Sigma m_\Sigma^3}{H(m_\Sigma)s(m_\Sigma)} \Gamma_{\Sigma\to\psi X} \mathcal{I}_\pm \,, \tag{5.49}$$

where $\mathcal{I}_\pm$ refers to the dimensionless integral

$$\mathcal{I}_\pm = \int_0^\infty dx x^4 \int_1^\infty \frac{d\gamma}{2\pi^2} \frac{\sqrt{\gamma^2-1}}{e^{\gamma x} \pm 1} \,, \tag{5.50}$$

which takes numerical values $\mathcal{I}_+ = 0.248$ (bosonic Σ) and $\mathcal{I}_- = 0.232$ (fermionic Σ). For a decaying boson, this yield results in (via eqn. 5.23):

$$\Omega_\psi h^2 = \left(\frac{\Gamma_{\Sigma\to\psi X}}{9.7\times10^{-25}\text{GeV}}\right)\left(\frac{m_\psi}{\text{GeV}}\right) g_\Sigma \left(\frac{m_\Sigma}{\text{GeV}}\right)^{-2} \left(\frac{g_{\rm eff}(T_{\rm prod.})}{106.75}\right)^{-3/2} . \tag{5.51}$$

Comparing with the observed dark matter density, $\Omega_{\rm DM}h^2 = 0.120$ [18] one obtains that the decay rate for the process $\Sigma \to \psi X$ that results in relic density Ω_ψ is:

$$\Gamma_{\Sigma\to\psi X} = 1.2\times10^{-25} g_\Sigma^{-1} \frac{m_\Sigma^2}{m_\psi} \left(\frac{g_{\rm eff}(T_{\rm prod.})}{106.75}\right)^{3/2} \frac{\Omega_\psi}{\Omega_{\rm DM}} \,. \tag{5.52}$$

This decay rate is to be multiplied by a factor 1/2 if $X = \psi$, since in this case the decay $\Sigma \to \psi\psi$ produces two dark matter particles. In the case where the mediator only has this single decay channel, eqn. (5.52) corresponds to a prediction for the decay length:

$$c\tau_\Sigma \simeq 1.6\,\text{m} \times g_\Sigma \left(\frac{m_\Sigma}{100\,\text{GeV}}\right)^{-2} \left(\frac{m_\psi}{10\,\text{keV}}\right) \left(\frac{g_{\rm eff}(T_{\rm prod.})}{106.75}\right)^{-3/2} \left(\frac{\Omega_\psi}{\Omega_{\rm DM}}\right)^{-1} , \tag{5.53}$$

which can lead to displaced vertices or anomalous charged tracks when the mediator Σ is produced at a collider.

Scattering processes can also contribute significantly to FIMP production in the considered scenario (see e.g. [7,138]), especially if the decay becomes kinematically suppressed [140] (see also the discussion in appendix A) or the mediator is $\text{SU}(3)_c$ charged and has many bath particles to scatter with [141]. A further complication can arise from the fact that freeze-in production is most efficient at comparatively high temperatures. While for WIMPs (see sec. 5.3) the relic abundance is set at temperatures $T \lesssim m_{\rm DM}/x_f$ with $x_f \sim 25$, freeze-in

production is most efficient around $T \sim m_\Sigma/\text{few}$ (as can be seen from the dx integrand in eqn. (5.50), growing with $x^4 \propto T^{-4}$ until it is cut off by the Boltzmann suppression at $x \sim$ few). Thus for $m_\Sigma \gtrsim$ few hundred GeV, electroweak symmetry restoration and thermal contributions to m_Σ can affect the result [142].

The couplings implied by FIMP scenarios are much smaller than for WIMPs, and standard WIMP searches can only be effective for some scenarios involving light mediators (e.g. [122]). The prediction of the mediator decay length, eqn. (5.53), has been advanced as a possible target for collider searches (e.g. [7, 113, 143, 144]), but it seems difficult to determine dark matter mass and mediator decay rate at the same time, since mediators decaying on detector length scales seem to imply a dark matter particle too light for a kinematical determination of its mass. Chapter 6 and section 7.1.1 of chapter 7 explore decay signals in multi-flavour models of FIMP dark matter.

Chapter 6

Multi-flavour Scalar FIMPs and Observational Signals

Freeze-in [7] of "feebly interacting massive particle" (FIMP) dark matter is a scenario of dark matter production, where the relic abundance is calculable from thermal processes in the early Universe. In contrast to freeze-out of WIMP dark matter, it is assumed that an initially negligible abundance of dark matter particles is increased gradually in the early Universe, through a coupling so "feeble" that the dark matter species never reaches equilibrium with the Standard Model bath.

The feeble coupling presents a challenge to detection of these dark matter candidates: the annihilation signatures expected for WIMP dark matter are very suppressed, and dark matter direct detection is only feasible in the case where a light mediator enhances the scattering cross section [122]. On the other hand, the feeble coupling to the Standard Model may be involved in making the dark matter cosmologically long lived. Rare dark matter decays could in this case lead to tests of freeze-in dark matter production. This is possible in the keV mass range for freeze-in dark matter, where the feeble coupling involved in dark matter production is sufficiently small to not violate X-ray bounds on present day dark matter decay [142]. For larger masses an approximate or exact symmetry needs to be introduced to suppress the decay rate, and testing the freeze-in mechanism becomes very challenging.

In the face of the complexity of the Standard Model sector with its three-generation structure, it is conceivable that the dark sector may also be complex; that there exist more than one dark matter candidate in the particle spectrum and that more than one dark matter species contribute to the relic density. This simple extension of the minimal scenario can result in new signals, not present in the single component case.

This chapter points out dark matter decay signals as a probe of multicomponent freeze-in dark matter: We assume that a dark sector, stabilised by an exact $\mathbb{Z}_2$ symmetry, contains multiple flavours of dark matter candidates, which are distinguished only by their mass. The coupling responsible for freeze-in generically produces all flavours of dark matter and at the same time leads to decay of the heavier flavours into the lightest one. The decay rate is related to the relic density, in analogy to the annihilation rate in the freeze-out scenario, leading to new possibilities for probing the freeze-in scenario.

In this chapter, we focus on the arguably simplest dark matter candidate, the real scalar singlet. As portals to the Standard Model, we consider coupling through the Higgs portal (section 6.1) or by coupling to a Standard Model fermion via a heavy mediator

(section 6.2). Scenarios of single component FIMP dark matter along these lines have been considered, *e.g.* in [126,127,145]. Section 7.1.1 of chapter 7 extends the results derived here to the case of fermionic dark matter. The considered multicomponent models lead to FIMP production via freeze-in (see section 5.4) and allow for the decay of the heavier FIMP species. In particular, we consider the tree-level or loop-induced decay $\phi_2 \to \phi_1\gamma\gamma$ into gamma rays, which gives rise to a very distinctive photon energy spectrum [105]. Such spectral features in the gamma ray sky can be effectively separated from the featureless astrophysical background, making them a golden channel for positive dark matter identification (see section 4.3). We investigate whether current gamma-ray instruments are sensitive enough to probe the decay rates expected from freeze-in production.

The results presented in this chapter have in large parts been published at [11].

6.1 Higgs portal FIMP

We add two real scalars $\phi_{1,2}$ to the Standard Model. Unless they are lighter than a few keV, their stability needs to be ensured by a stabilising symmetry, such as a global, discrete $\mathbb{Z}_2$, under which all SM particles are even and $\phi_{1,2}$ are odd. The renormalisable Lagrangian for the Standard Model with two added real scalars $\phi_{1,2}$ reads

$$\mathcal{L} = \mathcal{L}_{\rm SM} + \frac{1}{2}\partial_\mu\phi_i\partial^\mu\phi_i - \frac{1}{2}m_{ij}\phi_i\phi_j - \frac{1}{4!}\lambda'_{ijkl}\phi_i\phi_j\phi_k\phi_l - \frac{1}{2}\lambda'_{ij}\left(H^\dagger H\right)\phi_i\phi_j, \tag{6.1}$$

where summation over repeated indices is implied. The symmetry and Lorentz structure of the model allows for renormalisable self-interactions with coupling λ'_{ijkl} and the "Higgs-portal" coupling λ'_{ij}, which connects the dark scalars ϕ_i to the visible sector. As we are interested in the case where the interaction responsible for the relic abundance can be directly related to the present-day decay signature, we neglect modifications of the relic abundance by the self-interaction λ'_{ijkl}.[1]

The single component case of this archetypal dark matter model has been studied extensively, as WIMP freezing-out via the Higgs-portal (see e.g. [147–150]), as FIMP freezing in via the Higgs-portal (see e.g. [127, 142, 145, 151]) or as SIMP where the relic abundance is determined by the self-interaction (see e.g. [128]). In this model, the lightest dark matter candidate ϕ_1 is by construction absolutely stable: the $\mathbb{Z}_2$-odd initial state ϕ_1 can not decay to a final state consisting of $\mathbb{Z}_2$-even SM particles. We diverge from minimality by adding not one, but two real scalars $\phi_{1,2}$ to the Standard Model as a simple multicomponent DM model.

After electroweak symmetry breaking (writing $H = \left(H^+, (v+h)/\sqrt{2}\right)^T$), the relevant terms of the Lagrangian read in the mass basis of the scalars

$$\mathcal{L} \supset \frac{1}{2}\partial_\mu\phi_i\partial^\mu\phi_i - \frac{1}{2}m_1^2\phi_1^2 - \frac{1}{2}m_2^2\phi_2^2 - \frac{1}{2}\lambda_{ij}vh\phi_i\phi_j. \tag{6.2}$$

The free parameters of this model are the masses $m_2 \geq m_1$ and the couplings $\lambda_{11}, \lambda_{12}, \lambda_{22}$. In the near-degenerate scenario $m_2 \simeq m_1$, it is useful to introduce a mass degeneracy parameter Δ, which we define as $\Delta = 1 - m_1^2/m_2^2$.

[1] Generally, self-interactions can modify the abundance of a freeze-in produced dark matter candidate, see section 8.3.2 and [146]. Previous studies [142] find that self-interactions in the single DM flavor case do not *decrease* the relic abundance by more than a factor of 2 without being in conflict with the constraints discussed in section 4.2. Hence, they do not significantly affect our results on maximal possible signals calculated below.

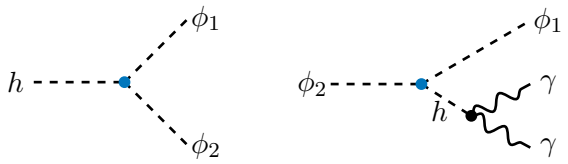

Figure 6.1: Production (*left*) and decay (*right*) processes for the multicomponent real scalar FIMP model coupled through the Higgs portal.

In this scenario, the coupling λ_{12}, alongside with $\lambda_{11}, \lambda_{22}$, can lead to freeze-in production of ϕ_1, ϕ_2 in the early Universe. At the same time, the coupling λ_{12} allows for decay of the heavier dark matter candidate ϕ_2 into the lighter ϕ_1 plus Standard Model particles. In particular, the decay $\phi_2 \to \phi_1\gamma\gamma$ is possible and produces a distinctive gamma ray spectrum. This opens up the possibility of signals of the otherwise elusive freeze-in production mechanism in the multicomponent setup of the model, as is also illustrated by the Feynman diagrams of the two processes, fig. 6.1. In the following, we relate the relic density and indirect detection signal strength in this model.

Dark matter indirect detection is introduced in section 4.3. In general, a dark matter decay signal is related to the source term at positions $\vec{r}$:

$$Q(E, \vec{r}) = \frac{\rho_{\phi_2}(\vec{r})}{m_2} \Gamma_{\phi_2 \to \phi_1 \gamma\gamma} \frac{dN_\gamma}{dE} \,, \tag{6.3}$$

where $\rho_{\phi_2}(\vec{r})/m_2$ is the number density of decaying particles at position $\vec{r}$, $\frac{dN_\gamma}{dE}$ is the gamma ray energy spectrum produced in a single decay and $\Gamma_{\phi_2 \to \phi_1\gamma\gamma}$ is the partial decay rate of the process $\phi_2 \to \phi_1\gamma\gamma$. The decay process has been calculated in [105], giving

$$\Gamma_{\phi_2 \to \phi_1\gamma\gamma} = \frac{1}{26880\pi^3} \left(\frac{\lambda_{12} c_{\gamma\gamma}}{m_h^2}\right)^2 m_2^5 \Delta^7 \, {}_2F_1\left(3, 4, 8; \Delta\right) , \tag{6.4}$$

and energy spectrum dN_γ/dE shown in Fig. 6.2. Here, $c_{\gamma\gamma} \simeq -2.03 \times 10^{-3}$ is the effective coupling of the Higgs to two photons, $\Delta = 1 - m_1^2/m_2^2$ parametrizes the mass difference between both FIMPs as introduced above, and ${}_2F_1\left(3, 4, 8; \Delta\right)$ is a hypergeometric function which takes values between 1 and 35 for Δ between 0 and 1. [105] look for this signal in the diffuse γ-ray flux reported by the INTEGRAL [152], COMPTEL [153], EGRET [154] and Fermi-LAT [155] instruments and calculate upper limits on the effective decay rate $\frac{\Omega_2}{\Omega_{\rm DM}} \Gamma_{\phi_2 \to \phi_1\gamma\gamma}$.

The relic abundance can be calculated using the analytical results for freeze-in via a heavy mediator from section 5.4.[2] Dark matter production is governed by the same coupling λ_{12} as dark matter decay, in conjunction with $\lambda_{11,22}$. The decay processes $h \to \phi_i\phi_j$ dominates production for $m_h > m_1 + m_2$, with decay rate given by:

$$\Gamma_{h \to \phi_i\phi_j} = \frac{\kappa \lambda_{ij}^2 v^2}{16\pi m_h} \sqrt{1 - \frac{4m_2^2}{m_h^2} + \frac{2m_2^2\Delta}{m_h^2} + \frac{m_2^4\Delta^2}{m_h^4}} \,, \tag{6.5}$$

[2] We have checked agreement with the numerical code micrOMEGAs [126], employing FeynRules [156] and CalcHEP [157] in the broken electroweak phase, extending our results into the scattering-dominated regime numerically where indicated.

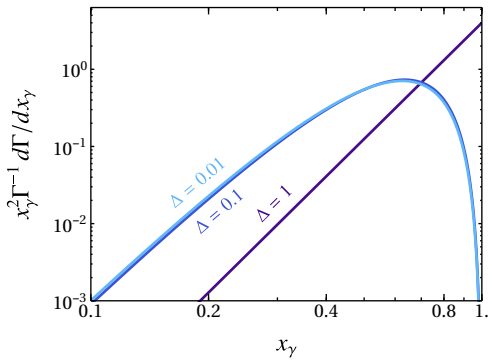

Figure 6.2: Energy spectrum of the decay $\phi_2 \to \phi_1\gamma\gamma$ [105]. Here $x_\gamma = 2E_\gamma/m_2\Delta$ is the gamma ray energy normalised to its maximum value. The spectra $\Gamma^{-1}d\Gamma/dx_\gamma$ are scaled with x_γ^2, illustrating how they stand out against power law astrophysical backgrounds that typically drop faster than E^{-2} (see sec. 4.3).

where $\kappa = 1/2$ for $i = j$ and $\kappa = 1$ otherwise. Using eqn. (5.52), and imposing the requirement $\Omega_{\phi_1} + \Omega_{\phi_2} \leq \Omega_{\rm DM}$, we obtain:

$$\lambda_{12} \lesssim 1.2 \times 10^{-11} \left(\frac{m_2(1+\sqrt{1-\Delta})}{\rm GeV}\right)^{-1/2} \left(1 - \frac{4m_2^2}{m_h^2} + \frac{2m_2^2\Delta}{m_h^2} + \frac{m_2^4\Delta^2}{m_h^4}\right)^{-1/4} , \qquad (6.6)$$

where this upper limit is saturated if FIMP production is dominated by the channel $h \to \phi_1\phi_2$. This upper limit implies an upper limit on the decay width, eqn. (6.4):

$$\Gamma_{\phi_2\to\phi_1\gamma\gamma} \lesssim \left(2 \times 10^{29}\,{\rm s}\right)^{-1} \left(\frac{m_2}{\rm MeV}\right)^4 \Delta^7\, {}_2F_1\left(3,4,8;\Delta\right) . \qquad (6.7)$$

This can be compared to the observed limits obtained in [105]. Fig. 6.3 shows the maximal attainable gamma ray signals as a lower limit on the inverse effective decay rate $\Gamma_{\rm eff}^{-1} = (\Gamma \times \Omega_2/\Omega_{\rm DM})^{-1}$ in terms of the mass m_2 of the decaying dark matter component for different values of the mass splitting parameter Δ. In the figure, the solid lines correspond to the analytical result eqn. (6.7), which agree well with the results obtained using MICROMEGAS (dashed). The numerical results extend into the scattering-production dominated regime at $m_1 + m_2 > m_h$. Limits are shown only for $\Delta = 1$ (very hierarchical spectrum) and $\Delta = 10^{-3}$ (very degenerate spectrum), as the limits are only mildly dependent on Δ in the degenerate case [105]. Fig. 6.3 shows that strong gamma ray signals from dark matter decay are possible in the multicomponent Higgs portal FIMP scenario for $m_2 \gtrsim$ MeV. The signals are expected if the decay rate $\Gamma_{\phi_2\to\phi_1\gamma\gamma}$ (eqn. 6.4) is not suppressed by a tiny mass splitting Δ, but even very degenerate scenarios can give rise to signals for larger m_2.

In addition to the $\phi_1 \to \phi_2\gamma\gamma$ decay channel, all other kinematically accessible decay channels of the off-shell Higgs involved in the $\phi_1 \to \phi_2$ decay are possible. This can offer additional signatures, of which an example is shown as the pink shaded region, which is excluded by anomalous energy injection during CMB decoupling [158] through the process $\phi_2 \to \phi_1 e^+e^-$ [105] only (the line shown is for the hierarchical $\Delta = 1$ case; in the degenerate case, the limit lies outside of the figure). This illustrates the possibility of multiple complementary probes.

The results displayed in Fig. 6.3 can be interpreted as gamma ray limits on the dark matter masses $m_{2,1}$, assuming $|\lambda_{11}|, |\lambda_{22}| \ll |\lambda_{12}|$ such that λ_{12} dominates FIMP production.

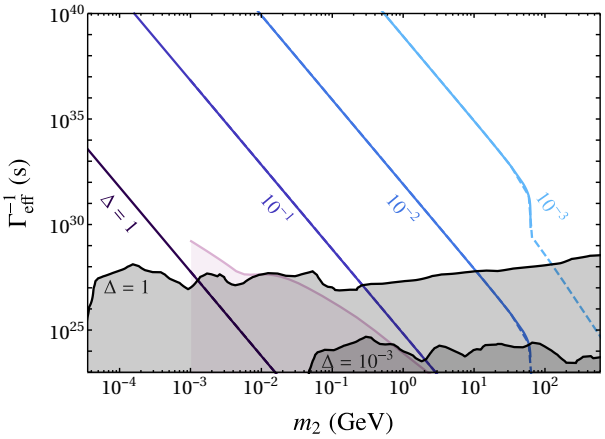

Figure 6.3: Maximal possible gamma ray signal in the Higgs-portal multicomponent FIMP scenario, in terms of a lower limit on the inverse decay rate for $\phi_2 \to \phi_1\gamma\gamma$, as a function of the mass of the decaying FIMP component m_2 for different values of the degeneracy parameter Δ. The gray regions correspond to the lower limit on the inverse decay rate from the non-observation of the associated sharp spectral feature in the isotropic diffuse photon flux [105]. In the pink region, gamma ray signals for $\Delta = 1$ are precluded by CMB limits on the associated decay into electrons, as described in the text.

In this case, $m_2 \gtrsim 1\,\text{MeV}$ is excluded for non-degenerate mass spectra, while gamma ray limits can be avoided in the near-degenerate case for $m_2 \lesssim 2\,\text{GeV}$, $m_2 \lesssim 55\,\text{GeV}$ or $m_2 \lesssim 800\,\text{GeV}$ when $\Delta = 10^{-1}$, $\Delta = 10^{-2}$ and $\Delta = 10^{-3}$ respectively. The limits are likewise relaxed when $|\lambda_{12}| \ll |\lambda_{11}|, |\lambda_{22}|$, such that the decay $\phi_2 \to \phi_1\gamma\gamma$ is suppressed or ϕ_2 is not the dominant dark matter component.

Finally, we note that the FIMP couplings with the Higgs doublet in eqn. (6.1) do not only lead to the cubic and quartic interactions with the physical higgs boson after electroweak symmetry breaking, but also contribute to the FIMP masses. For freeze-in production, the typical size of the couplings $\max(\lambda'_{ii}, \lambda'_{ij}) \sim 10^{-11}(m_i/\text{GeV})^{-1/2}$ would be associated to a contribution of the order $\delta m_{ij}^2 \sim \lambda'_{ij} v^2/2 \sim 3.5\,\text{MeV}$ to the scalar masses. Smaller FIMP masses correspondingly require special choices of the Lagrangian parameters in the unbroken theory. This further highlights the promise in looking for signals of scalar FIMPs in MeV gamma rays.

6.2 Leptophilic scalar FIMP

In this section, we consider a less-minimal model than the Higgs portal scenario discussed above, that will lead to qualitatively different results. We couple the dark matter candidates $\phi_{1,2}$ to the Standard Model by introducing a $\mathbb{Z}_2$-odd, charged SU(2)-singlet fermion Ψ, which allows for a renormalisable coupling of the scalars to the right-chiral leptons. The relevant term of the interaction Lagrangian reads

$$\mathcal{L}_\Psi = y_i \phi_i \bar{\Psi} P_R l + \text{h.c.}\,. \tag{6.8}$$

As in the previous section, we assume that the scalar self-interaction $\lambda'_{\phi,ijkl}\phi_i\phi_j\phi_k\phi_l$ is negligibly small and furthermore in this section also assume that the Higgs portal coupling

λ_{ij} contributes negligibly to both dark matter production and decay. For simplicity, and to avoid lepton flavour violation, we assume that Ψ only couples to one Standard Model lepton, $l = e, \mu, \tau$. This model has been considered before in the context of single-component freeze-in dark matter by [113, 126].

In this scenario, dark matter decay $\phi_2 \to \phi_1\gamma\gamma$ proceeds via a loop of the heavy fermion and a lepton (see fig. 6.4). The differential decay rate $d\Gamma_{\phi_2\to\phi_1\gamma\gamma}/dE_\gamma$ and the partial decay rate $\Gamma_{\phi_2\to\phi_1\gamma\gamma}$ have been calculated by [105]. They give rise to gamma ray spectral features similar to the Higgs-portal case shown in figure 6.2, which however depend on the masses m_Ψ, m_l of the particles in the loop. The decay rate depends on the mass of the heavy fermion m_Ψ, the mass of the lepton m_l and, most crucially, on the combination of couplings $\Gamma_{\phi_2\to\phi_1\gamma\gamma} \propto y_1^2 y_2^2$.[3] This combination of couplings is constrained by relic density considerations.

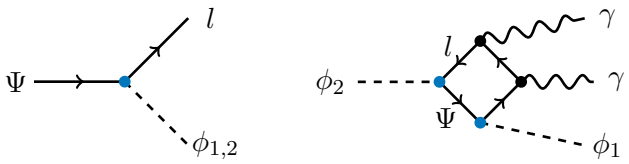

Figure 6.4: Production process (*left*) and an example diagram for the decay process into gamma rays (*right*) for the multicomponent real scalar FIMP model coupled to a SM lepton l by the charged fermion Ψ.

Relic density relations As in the previous section, the FIMP yield grows with larger portal couplings y_i, meaning that the decay rate of the process $\phi_2 \to \phi_1\gamma\gamma$ cannot be arbitrarily large without overproducing dark matter. The relic abundance of ϕ_1 and ϕ_2 generated in the decay $\Psi \to \phi_i l$ can be calculated from eqn. (5.52), using the Ψ decay rate given by:

$$\begin{aligned}\Gamma_{\Psi\to\phi_i l} &= \frac{|y_i|^2 m_\Psi}{32\pi}\left(1+\frac{2m_l}{m_\Psi}+\frac{m_l^2}{m_\Psi^2}-\frac{m_i^2}{m_\Psi^2}\right)\sqrt{1-\frac{2(m_l^2+m_i^2)}{m_\Psi^2}+\frac{(m_l^2-m_i^2)^2}{m_\Psi^4}} \\ &\simeq \frac{|y_i|^2 m_\Psi}{32\pi},\end{aligned} \tag{6.9}$$

where in the last line we have assumed $m_{\phi_i}, m_l \ll m_\Psi$. The requirement $\Omega_{\phi_1} + \Omega_{\phi_2} \leq \Omega_{\rm DM}$ then translates into a limit on the couplings:

$$|y_1|^2\frac{m_1}{m_\Psi} + |y_2|^2\frac{m_2}{m_\Psi} \leq 3.1\times10^{-24}\,. \tag{6.10}$$

This single constraint on the two independent couplings y_i allows for considerably more freedom than the constraint on the single portal coupling λ_{12} in the higgs portal case (eqn. 6.6). We are interested again in the maximal attainable gamma ray signal, $\Gamma_{\rm eff} = \Gamma \times \Omega_2/\Omega_{\rm DM} \propto$

[3] The full expression for the decay rate reads $\Gamma^{\Psi-\text{mediated}}_{\phi_2\to\phi_1\gamma\gamma} = \frac{\alpha^2}{128\pi^5}\,\mathrm{Re}(y_1 y_2^*)^2\left(\frac{m_l^4\Delta}{m_\Psi^2 m_2}\right)\int_0^1 dx_\gamma\, F_{\gamma\gamma}(x_\gamma)$ with $F_{\gamma\gamma} = \int_{z_{\rm min}}^\infty dz \frac{|\mathcal{I}(z)|^2}{z^2}$, where $z_{\rm min} = \frac{2m_l^2}{m_2^2}\frac{1-x\Delta}{(1-x)x\Delta^2}$ and $\mathcal{I}(x) = 1 + \frac{1}{2}(1-2x)\left[\mathrm{Li}_2\left(\frac{1+\sqrt{1-2x}}{x}\right) + \mathrm{Li}_2\left(\frac{1-\sqrt{1-2x}}{x}\right)\right]$. [105]

$y_1^2 y_2^2 \times y_2^2 \propto (\Omega_1/\Omega_{\rm DM})(\Omega_2/\Omega_{\rm DM})^2$, which is maximised for the couplings that give $\Omega_2 = 2\Omega_1$, independent of $m_{1,2}$.

The individual couplings can not be arbitrarily large before the freeze-in assumption of out-of-equilibrium evolution of $Y_{1,2}$ breaks down. Using $Y_i^{\rm fi} < Y_i^{\rm eq} \sim \frac{T^3 g_i/\pi^2}{g_{\rm eff}(T) T^3 2\pi^2/45}$, we require

$$|y_i| \ll 5 \times 10^{-9} \sqrt{\frac{m_\Psi}{\rm GeV}}, \tag{6.11}$$

to ensure that the DM abundances never thermalise. This implies lower limits for the FIMP masses. In particular, for Ω_2 to make up 2/3 of the observed dark matter density and Ω_1 1/3, one finds $m_1 \gtrsim 40\,{\rm eV}$, $m_2 \gtrsim 80\,{\rm eV}$.

In addition to freeze-in production, there is a contribution to the relic density arising from the fact that the mediator Ψ is $\mathbb{Z}_2$-odd: The charged fermion Ψ is in equilibrium with the SM bath in the early Universe, producing $\phi_{1,2}$ in rare decays via freeze-in as described in section 5.4. However, once annihilation reactions like $\Psi^+\Psi^- \to \gamma\gamma$ freeze out and cannot keep Y_Ψ at its equilibrium value, all remaining Ψ decay out-of-equilibrium into $\phi_{1,2}$, which is not taken into account in the freeze-in production of $\phi_{1,2}$ above. The relic density of $\phi_{1,2}$ obtained through this so-called "super-WIMP" mechanism [159, 160] is given by

$$\Omega_{\rm superWIMP} h^2 = \Omega_{\Psi,0} h^2 \times \frac{{\rm Br}(\Psi \to \phi_1) m_1 + {\rm Br}(\Psi \to \phi_2) m_2}{m_\Psi}, \tag{6.12}$$

where the frozen-out Ψ yield is roughly $\Omega_{\Psi,0} h^2 \sim 0.10$ for $m_\Psi = 650\,{\rm GeV}$, determined using MICROMEGAS [126], assuming the couplings to $\phi_{1,2}$ are too feeble to contribute to keeping Ψ in equilibrium and neglecting Sommerfeld enhancement. The super-WIMP contribution is included in the results below, but has negligible impact for the adopted parameters $m_1, m_2 \ll m_\Psi$.

Likewise in contrast to the Higgs-portal case, eqn. (6.10) has the interesting property that constraints on the couplings can be relaxed for small masses m_2 and m_1 individually, instead of only depending on the combination $m_2 + m_1$ (cf. eqn. 6.6). The maximal possible gamma ray signals here hence depend on bounds on the smallness the mass of the dark matter component that makes up the bulk of dark matter, as well as that of a potentially much lighter subdominant component.

Structure formation constraints on the dark matter mass The formation of structure in the Universe is sensitive to the velocity dispersion of dark matter: If the average velocity of dark matter particles is large, small-scale inhomogeneities are washed out by dark matter free streaming, and structure formation even at large scales may proceed very differently. In models of thermally produced dark matter, this puts a lower limit on the dark matter mass, depending on the dark matter velocity distribution generated by the particular production mechanism, as discussed in section 4.1.

The phase space distribution of FIMP dark matter decay is non-thermal, but warmness bounds on the mass of thermal dark matter [53] can be recast to bounds on the FIMP mass in the single component scenario $m_{\rm FIMP} > 15.6\,{\rm keV} \cdot (106.75/g_{{\rm eff}s}(T_{\rm max\ prod.}))^{1/3}$, using results from [161].[4] This is always satisfied for ψ_2 for the range of parameters that can give interesting gamma ray signatures.

[4] Kamada&Yanagi [161] have demonstrated an analytical mapping between thermal and freeze-in produced dark matter free-streaming signatures by matching their velocity dispersions. The define the warmness quantity $\tilde{\sigma} = \sqrt{\langle p^2 \rangle}/\tilde{T}$, with $\tilde{T}$ equal to the dark matter temperature in the case of thermal dark matter and

In the multicomponent scenario however, the lighter ψ_1 can constitute a subdominant but significant fraction of dark matter that is lighter and hence has a larger velocity dispersion. In [64], bounds on the fraction of non-cold dark matter $f_{\rm ncdm} = \Omega_{\rm ncdm}/(\Omega_{\rm cdm} + \Omega_{\rm ncdm})$ were obtained. They assume that the velocity distribution of non-cold dark matter is thermal with temperature equal to that of the standard model neutrinos, $T_{\rm ncdm} = T_\nu$. For relics of mass m with different temperature $T/T_\nu \neq 1$, their constraints are to be evaluated at $m_{\rm ncdm} = m\frac{T_\nu}{T}$ (see section 4.1). Accounting also for the non-thermal velocity dispersion of freeze-in produced ψ_1 [161], we find an equivalent temperature that gives rise to the same velocity dispersion: $T^{\rm eff}_{\text{decay FIMP}} = T_\nu \cdot (10.75/g_{{\rm eff}s}(T_{\text{max prod.}}))^{1/3} \cdot 0.82 \sim 0.4\, T_\nu$. The bounds on the fraction of non-cold dark matter derived in [64] are then satisfied for $\Omega_{\psi_1}/\Omega_{\rm DM} \lesssim 0.2$ at 3σ confidence level for $m_1 = 40\,\text{eV}$, and get weaker for larger m_1. For the values of parameters that result in the maximal gamma ray flux, $\Omega_{\psi_2} = 2\Omega_{\psi_1}$, the warmness constraints are therefore marginally satisfied for $m_1 = 40$ eV, but well satisfied for larger masses.

Constraints related to the charged fermion The mass of Ψ is constrained by collider searches: At the LHC, it can be pair-produced by Drell-Yan production, in which a quark-antiquark pair produces a $\Psi^+\Psi^-$ pair that subsequently decays to $\phi_i\phi_j l^+ l^-$. The decay of the charged fermion can either happen promptly, resulting in events with a pair of oppositely charged leptons and missing energy, or only after some travel time in the detector, resulting in anomalous charged tracks. In our analysis, we have fixed for concreteness $m_\Psi = 650$ GeV, which saturates the current lower limit on the mass of long-lived charged fermions, assuming Drell-Yan production [162]. Limits on more short lived Ψ were compared in [113], who find various weaker limits for Ψ that decay within the detector, rendering the adopted value a conservative estimate. The bounds on Drell-Yan produced, promptly decaying particles are comparable or weaker than the bounds on anomalous charged tracks in the case of long lived scalar particles (see section 7.2.3), so we consider this value to be also allowed in the case that Ψ decays promptly. Note that FIMP production constrains the combination of parameters y_i^2/m_Ψ depending on m_i (eqn. 6.10) and the decay rate $\Gamma_{\phi_2\to\phi_1\gamma\gamma}$ is proportional to $y_1^2 y_2^2/m_\Psi^2$, such that the expected gamma ray signal is rather independent of m_Ψ.

The successful prediction of light element abundances from Big Bang nucleosynthesis can be spoiled by exotic energy injection from decaying particles. Particles with lifetimes $\tau < 0.1\,\text{s}$ safely decay before BBN [163], and we find $\tau_\Psi \lesssim 10^{-3}\,\text{s}$ for all of the parameters adopted below.

Results Figure 6.5 shows results for the maximal possible gamma ray flux compatible with the FIMP relic density constraint in eqn. (6.10), as a lower limit on the inverse effective decay rate $\Gamma^{-1}_{\rm eff} = (\Gamma_{\phi_2\to\phi_1\gamma\gamma} \times \Omega_2/\Omega_{\rm DM})^{-1}$, depending on the mass m_2 of the decaying dark matter component for a set of values of the mass m_1 of the lighter dark matter component, adopting $m_\Psi = 650\,\text{GeV}$. The three panels show results for $l = e, \mu, \tau$, which due to their different masses give different decay rates [105]. Limits on $\Gamma^{-1}_{\rm eff}$ obtained in [105] are also shown (gray), analogous to those in figure 6.3. We show only the limit for $\Delta = 1$, as evidently only hierarchical scenarios can yield appreciable signals in the heavy fermion mediated

equal to $\tilde{T}_{\rm FIMP} = T\,(h_{\rm eff}(T)/h_{\rm eff}(T_D))^{1/3}$ with $T_D \sim m_\Psi/3$ the temperature of maximal FIMP production. Using their results, we find $\tilde{\sigma}_{\rm thermal} = 3.6$ while $\tilde{\sigma}_{\rm FIMP} \sim 2.95$ for FIMP production from the decay of a much heavier mediator, demonstrating that FIMPs from heavy particle decay are slightly colder than thermal dark matter decoupling at the same time as the FIMPs are produced. Bounds on the free-streaming scale can thus be translated to bounds on the FIMP mass using eqn. (4.2) with $T_{\rm DM} \sim \tilde{T}_{\rm FIMP} \cdot 2.95/3.6$.

case. As in Fig. 7.2, the purple regions indicate where a gamma ray signal is precluded by non-observation of exotic energy injection from the tree-level decay $\phi_2 \to \phi_1 l^+ l^-$ during CMB decoupling [158] (using the relations between the different decay channels determined by [105]).

The lines shown correspond to the maximal possible gamma ray signal for every combination of $m_{1,2}$. This corresponds to $\Omega_2 = 2\Omega_1$, independent of $m_{1,2}$ as discussed above. The maximal signal in all cases is possible for the smallest m_1, allowing for the largest relic abundance $Y_1 \propto \Omega_1/m_1$ and hence largest y_1, up to the thermalisation bound eqn. (6.11). For the signal-maximising $\Omega_1 = \Omega_{\rm obs}/3$, this bound is saturated for $m_1 = 40\,\text{eV}$.[5]

Figure 6.5 shows that gamma ray spectral features can be sensitive probes of decaying leptophilic scalar FIMP dark matter, if the decaying dark matter particle has a mass in the GeV range, and the lighter component has a much larger coupling $y_1 \gg y_2$, permissible to the relic abundance constraint due to its much smaller mass. The observational prospects in gamma rays are better if the dark sector couples to the μ or τ leptons than to the electron, due to the m_l dependence of the decay process. In the case of coupling to electrons, the correlated tree-level decay $\phi_2 \to \phi_1 e^+ e^-$ is much more sensitive, illustrating the potential of discerning between these scenarios using complementary search strategies.

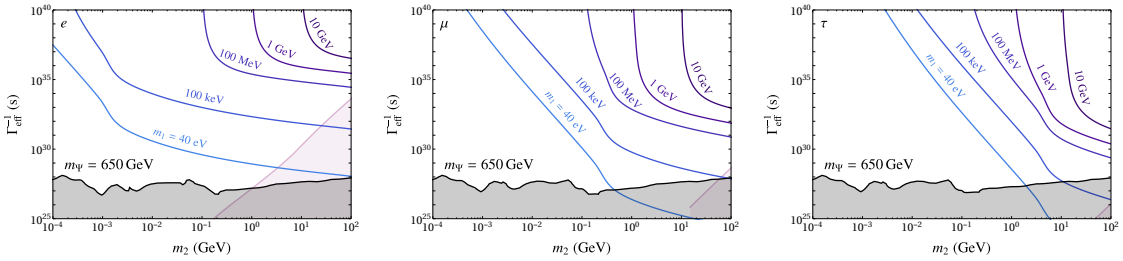

Figure 6.5: Maximal possible gamma ray signal in the heavy-charged-fermion mediated multicomponent FIMP scenario, in terms of a lower limit on the inverse decay rate for $\phi_2 \to \phi_1 \gamma\gamma$, as a function of the mass m_2 of the decaying FIMP component for different values of lighter FIMP mass m_1. The three panels, from left to right, correspond to the cases where the dark sector couples to the right-handed electron, muon and tau leptons. The gray regions correspond to the lower limit on the inverse decay rate from the non-observation of the associated sharp spectral feature in the isotropic diffuse photon flux [105]. In the pink region, gamma ray signals are precluded by CMB limits on the associated decay into leptons, as described in the text. The mass of the mediator Ψ has been fixed to 650 GeV.

6.3 Discussion

Dark matter production through freeze-in is a simple scenario for the origin of the dark matter relic density today. Though it requires stronger assumptions on the preceding cosmology, the simplest WIMP models can make for viable FIMP models for feeble values of the couplings between the particles charged under the SM gauge group and the DM candidates. In many models, however, the feeble couplings required make the FIMP scenario very hard to test. This has focused attention on decay of feebly coupled dark matter particles, where

[5] Larger couplings are possible for smaller masses, but this goes beyond the freeze-in scenario considered here. This "hot dark matter" regime is treated in detail for a similar model in section 7.1.2.

small individual decay rates may still result in appreciable production of energetic particles in the Galaxy today.

This chapter considered the possibility that the dark sector, just like the Standard Model sector, contains multiple flavours of particles, which share all quantum numbers except for their mass, and are all feebly coupled to the visible sector. We have argued that this allows for qualitatively new features compared to the single flavour scenario, indicating the possibility of gamma ray signals in an energy range not otherwise looked at in the context of FIMP searches.

Led by simplicity, we add two real scalar singlet particles $\phi_{1,2}$, odd under a $\mathbb{Z}_2$ dark matter parity, to the Standard Model. We study two qualitatively different scenarios, first considering their production and decay through the Higgs portal and second introducing a heavy charged fermion Ψ that couples them to a SM lepton. In the single component scenario, there is little hope for any observable signature in the Higgs portal case [145], and only searches for the mediator in the charged fermion case [113].

In the multicomponent scenario, the feeble couplings that determine the relic abundance generically lead to dark matter decay. Motivated by the special role that gamma-ray spectral features would have in positively identifying dark matter, we focus on the decay $\phi_2 \to \phi_1\gamma\gamma$ ($\phi_2 \to \phi_1\gamma$ being forbidden by angular momentum conservation). We have calculated the possible decay rates compatible with the relic abundance requirement, finding that some regions of parameter space are already ruled out by current experiments, allowing for gamma ray signals across the MeV range to the GeV range.

Feebly coupled single flavour dark matter models without stabilising symmetry also predict dark matter decay into gamma rays. In that case however, only keV-range X-rays are of interest, as the decay rates predicted by production already exceed observational limits in the MeV energy range [142,164]. This chapter motivates the search for dark matter decay at MeV energies, supporting the promise of future MeV-range gamma ray telescopes like the proposed AMEGO [165] or e-ASTROGAM [166,167] mission concepts.

The two scenarios of coupling the FIMP-candidates to the Standard Model differ in the typical predicted decay rates, owing to the decay topology: In the Higgs portal case, the $\phi_2 \to \phi_1\gamma\gamma$ decay involves only one feeble vertex (fig. 6.1), while in the leptophilic fermion mediated case, two vertices with feeble couplings enter the decay diagram (fig. 6.4). As a result, the decay rate in the Higgs portal case is relatively large, allowing for signals at the current experimental sensitivity down to $m_2 \sim \mathcal{O}(1)\,\mathrm{MeV}$ for hierarchical spectra $m_2 \gg m_1$ and also probing very degenerate scenarios (fig. 6.3). In contrast, the heavy fermion mediated case does not predict observable decay rates in the degenerate scenario $m_2 \sim m_1$. However, the relic density constraint on the coupling of the lighter DM candidate ψ_1 is relaxed for small $m_1 \sim \mathrm{eV} - \mathrm{keV}$, allowing for observable signals also in this scenario (fig. 6.5).

In this chapter, we have restricted our analysis of the two-flavour scenario to feeble couplings, for which the relic abundance of both dark matter candidates is determined by freeze-in. In the next chapter, a similar model where DM candidate fermions couple independently to a charged mediator is explored allowing any of the flavours to thermalise.

Chapter 7

Multi-flavour Fermionic Dark Matter and Observational Signals: A Full Analysis of a Leptophilic Toy Model

It is a peculiar feature of Nature that all fermions come in three flavours which share all gauge quantum numbers and differ only in their coupling to the Higgs field (and accordingly their mass). The origin of this is not understood. In cosmology and astrophysics, the first generation of all fermion families plays the dominant role, while the heavier, short-lived generations appear only on the sidelines. Standard Model relic particles from the early universe contain only first generation fermions, with the notable exception of neutrinos, for which cosmological observations tell us that three flavours are present today [18]. This chapter deals with the implications of the plausible presence of multiple flavours of Dark Matter fermions.

To this end, we add two fermions, ψ_1 and ψ_2, singlet under the SM gauge group to the Standard Model. As singlet fermions, they can be of Majorana-type (sticking to minimality in terms of degrees of freedom), with masses $m_2 > m_1$. To ensure stability of at least one dark matter candidate, we impose a $\mathbb{Z}_2$ symmetry under which ψ_1 and ψ_2 are odd, while all Standard Model particles are even.

In contrast to the singlet scalar dark matter candidate considered in Chapter 6, there are no renormalisable couplings between the visible sector and the $\mathbb{Z}_2$-odd fermions $\psi_{1,2}$. To couple the two sectors, we introduce a heavy scalar particle Σ, odd under the same $\mathbb{Z}_2$ symmetry, with mass $m_\Sigma > m_2, m_1$, and with SM gauge quantum numbers such that the Yukawa coupling $\bar{X}\psi_i\Sigma$ is allowed, with X a Standard Model fermion. Models along these lines have been investigated with both baryonic and leptonic X in single-component dark matter scenarios (see for example [107, 140, 141, 168–174]).

For concreteness and simplicity, we chose X to be a right-handed lepton. This model is often referred to as "leptophilic" dark matter, which has received a great deal of attention, first because it presents a challenge for detection in laboratory experiments (with the leading collider experiment being the LHC, a hadron collider, and leading direct detection experiments focusing on nuclear recoils, not electron recoils), and second because of cosmic ray anomalies that have driven dark matter studies in the past [107]. It can arise from a supersymmetric scenario where the lightest neutralino is the dark matter candidate and is

close in mass to the lightest slepton [107,174,175]. Choosing instead $X = L$ the left-handed Lepton doublet, one obtains the so-called *scotogenic model* for neutrino masses [176, 177]. Coupling to baryons instead results in much better sensitivity of collider and direct detection searches, and taking $\psi_{1,2}$ as Dirac fermions instead of Majorana ones can result in stronger constraints from DMID and DMDD [174]. Choosing coupling to right-handed leptons allows for the greatest freedom in choosing mass and coupling parameters.

The Lagrangian of the model contains the following terms

$$\mathcal{L} \supset (\mathcal{D}_\mu \Sigma)^\dagger (\mathcal{D}^\mu \Sigma) - m_\Sigma \Sigma^\dagger \Sigma - \lambda_{H\Sigma} |H|^2 |\Sigma|^2 + \left(\frac{1}{2} \overline{\psi_i} i \partial\!\!\!/ \psi_i - \frac{1}{2} m_i \overline{\psi_i^c} \psi_i - g_i \bar{l} P_L \psi_i \Sigma + \text{h.c.} \right) . \tag{7.1}$$

In general, we require $m_\Sigma > m_1$ to have an electrically neutral dark matter candidate and we concentrate on the scenario where also $m_\Sigma > m_2$, with $m_2 > m_1$, to have two potentially long lived dark matter candidates $\psi_{1,2}$.

ψ_1 is the lightest $\mathbb{Z}_2$-odd particle and hence absolutely stable, while the heavier ψ_2 can decay into ψ_1 and Standard Model particles through a virtual Σ, either at tree level $\psi_2 \to \psi_1 l^+ l^-$ or at one-loop level $\psi_2 \to \psi_1 \gamma$ (as well as $\psi_2 \to \psi_1 Z, h$ when kinematically allowed), see fig. 7.1. The decay rates into all these channels are proportional to $|g_1|^2 |g_2|^2$, such that ψ_2 can be cosmologically long-lived, if the couplings g_i are small enough. In that case, the $\psi_2 \to \psi_1 \gamma$ decay mode results in a monochromatic signal, which is routinely searched for in the gamma ray sky (e.g. [108, 178]). This allows for tests of the multicomponent dark matter scenario analogously to those explored in chapter 6.

The charged scalar Σ is expected to be in equilibrium with the SM bath in the early universe and is the portal connecting the dark and visible sectors. It decays with a lifetime much shorter than the age of the universe, since the decay rate is only proportional to $|g_i|^2$. The presence of this new charged particle in the theory can however lead to new signals at colliders, in the form of events with oppositely charged leptons and missing transverse energy if it decays promptly, or as highly ionizing charged tracks if it travels in the detector before decaying.

No connection is made to SM flavour physics, neither in terms of modeling the possible origin of the flavour structures of the dark and visible sectors, nor in terms of a detailed study of lepton flavour violation effects. Without introducing flavour symmetries, Σ couples to all leptons through the Yukawa term $g_{i\alpha} \bar{l}_\alpha P_L \psi_i \Sigma$, which generically leads to lepton flavour violating processes, such as $\mu \to e\gamma$, on which there exist thight experimental bounds. This can be prevented by postulating that Σ carries a global family quantum number, ensuring it only couples to one lepton family [171].[1] After specifying the lepton generation Σ couples to, $l = e, \mu, \tau$, the two-flavour model is then specified by three masses and two couplings

$$m_\Sigma,\ m_2,\ m_1,\ g_2,\ g_1\,.$$

This chapter discusses the effects of the presence of a second dark matter flavour on dark matter phenomenology and the possible identifiability of the model. Section 7.1.1 uses analytical results from section 5.4 for the scenario where $\psi_{1,2}$ are both FIMPs to predict possible signatures from dark matter decay. Realising that a subdominant component of

[1] [170] discusses SM-flavour implications in an analogous single-component model coupled to up-type quarks in their appendix. [174] calculates LFV constraints on $g_{i\alpha}$ in the single-component variant of the present model, finding that flavour off-diagonal Yukawa couplings must be much smaller than the couplings required for WIMP freeze-out.

dark matter may be relativistic, section 7.1.2 extends these results to the FIMP-HDM regime, where the relic abundance of ψ_2 is still determined by freeze-in, but the lighter ψ_1 is allowed to thermalise, resulting in a hot dark matter contribution. In section 7.1.3, a numerical treatment is used to calculate relic abundances for all possible combinations of couplings, where either or all of the fermions may thermalise, allowing for absence of chemical equilibrium between them. This completes the thermal relic picture in the two-flavour leptophilic fermion DM model. Signatures of the two-flavour setup are discussed in section 7.2, with an emphasis on dark matter indirect detection. Results are discussed in section 7.3.

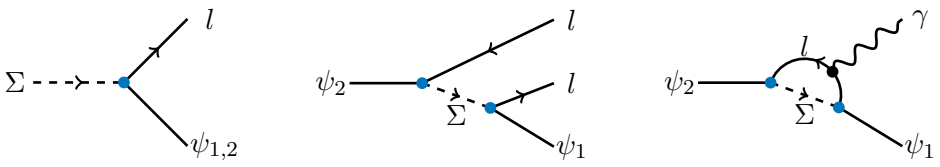

Figure 7.1: Production (*left*), three-body decay (*middle*) and two-body decay (*right*) processes in the multi flavour leptophilic fermion model.

7.1 Production regimes of multi flavour leptophilic fermion dark matter

The dark matter relic density is the most well measured dark matter observable, and the way the relic abundance is determined in the early universe characterises different dark matter scenarios. This section takes one particle physics model, the two-flavour leptophilic dark matter model defined by eqn. (7.1) and investigates which dark matter production scenarios are possible.

We restrict ourselves to scenarios that are calculable assuming the radiation-dominated era of standard cosmology extends to temperatures $T_{\mathrm{RH}} \gg \max(m_\Sigma, m_2)$. In particular, we do not consider $\psi_{1,2}$ production during inflation or reheating. In the case of small couplings (see eqn. 7.6), we assume that the dark matter contribution produced by thermal processes at $T < T_{\mathrm{RH}}$ dominates over any pre-existing abundance produced at earlier times.

We can then distinguish between three general mechanisms that can determine the dark matter relic abundance in the present model:

1. *FIMP, freeze-in:* Interactions between the thermal bath and a dark matter candidate ψ_i are rare, such that a small abundance $Y_{\psi_i} \equiv n_{\psi_i}/s$ is produced over time, never equilibrating with the thermal bath.

2. *HDM, relativistic freeze-out:* Interactions between the thermal bath and ψ_i are sufficient to keep Y_{ψ_i} at the equilibrium abundance $Y_{\psi_i}^{\mathrm{eq}}$ at high temperatures (erasing any previous history of Y_{ψ_i}), but are still small enough that they become rare before T drops below m_i, i.e. while ψ_i is still relativistic. To not exceed the observed abundance, the hot dark matter component produced this way must be very light.

3. *WIMP, non-relativistic freeze-out:* Interactions between the thermal bath and a dark matter candidate ψ_i are large enough to keep $Y_{\psi_i} \sim Y_{\psi_i}^{\mathrm{eq}}$ until $T \ll m_i$. Y_{ψ_i} freezes when ψ_i is already nonrelativistic and accordingly Boltzmann suppressed.

In the two-flavour model, combinations of these scenarios can be relevant in determining the total relic density.

Multi-flavour reeze-in was already discussed in detail in chapter 6 and the analytical results from section 6.2 for a leptophilic scalar are easily translated to the leptophilic fermion case where both $Y_{1,2}$ are determined by freeze-in (section 7.1.1). The analysis for the fermion case goes beyond that of chapter 6 by noting that the non-thermalisation requirement for the freeze-in mechanism is not a constraint, but a transition to the HDM regime, which is treated analytically in section 7.1.2. This covers the combinations where $\psi_2 - \psi_1$ are FIMP-FIMP and FIMP-HDM. To assess the viability of FIMP-WIMP/WIMP-FIMP/WIMP-WIMP production of $\psi_2 - \psi_1$, the Boltzmann equations are solved numerically for general combinations of couplings g_1, g_2 in section 7.1.3. Standard numerical codes like MICROMEGAS [126] are insufficient for this general study, due to the potential absence of chemical equilibrium between the dark sector species. Instead, we have implemented the coupled Boltzmann equations for $Y_\Sigma, Y_{1,2}$ in MATHEMATICA [179]. Nontrivial implementation details are outlined in appendix A.

7.1.1 Leptophilic multicomponent FIMP

For the purposes of this section, we assume that the couplings g_i are very small, such that both ψ_1 and ψ_2 never thermalise. The analysis of gamma ray signals from dark matter decay then proceeds in complete analogy to section 6.2.

The relic abundance of ψ_1 and ψ_2 is generated from $\Sigma \to \psi_i l$ decays, with rate

$$\begin{aligned}\Gamma_{\Sigma\to\psi_i\bar{l}} &= \frac{1}{16\pi m_\Sigma}|g_i|^2\left(m_\Sigma^2 - (m_l^2+m_i^2)\right)\sqrt{1-\frac{2(m_i^2+m_l^2)}{m_\Sigma^2}+\frac{2(m_i^2-m_l^2)^2}{m_\Sigma^4}} \\ &\simeq \frac{m_\Sigma|g_i|^2}{16\pi}.\end{aligned} \tag{7.2}$$

Using eqn. (5.52) for the relation between mediator decay rate and FIMP relic abundance, we find a relation between coupling and relic abundance:

$$|g_i|^2\frac{m_i}{m_\Sigma} \leq 2.9\times10^{-24}\left(\frac{\Omega_i}{\Omega_{\text{obs}}}\right), \tag{7.3}$$

in complete analogy to the scalar case. This can be taken as a conservative limit on the couplings from avoiding dark matter overproduction, in the sense that additional contributions to the freeze-in abundance from scattering or a super-WIMP contribution would further tighten this limit. The super-WIMP contribution from out-of-equilibrium decay of frozen-out Σ particles (see eqn. 6.12) is negligible for the adopted parameters and the scattering contribution is subdominant for $m_\Sigma \gg m_i$ [140] (see also fig. A.1 in appendix A).

7.1.1.1 Gamma ray signatures in the FIMP-FIMP case

To facilitate comparison with the results in chapter 6 we proceed here directly to the associated gamma ray signals before discussing other production mechanisms. Similar to the heavy fermion mediated scalar FIMP case, the gamma ray signal is proportional to $\Gamma_{\psi_2\to\psi_1\gamma}\Omega_2 \propto |g_1|^2|g_2|^4$, with g_i constrained by eqn. (7.3) (see also fig. 7.1). Using the expression for $\Gamma_{\psi_2\to\psi_1\gamma}$ given below (eqn. 7.15) and eqn. (7.3) results in the following upper

limit on the decay rate for $\psi_2 \to \psi_1\gamma$ from freeze-in production:

$$\Gamma_{\psi_2\to\psi_1\gamma} \lesssim \left(8\times10^{30}\,\mathrm{s}\right)^{-1}\left(1-\frac{m_1^2}{m_2^2}\right)^3\left(1-\frac{m_1}{m_2}\right)^2\left(\frac{m_{\psi_1}}{\mathrm{GeV}}\right)^{-1}\left(\frac{m_{\psi_2}}{\mathrm{GeV}}\right)^4\left(\frac{m_\Sigma}{\mathrm{GeV}}\right)^{-2}\frac{\Omega_{\psi_1}\Omega_{\psi_2}}{\Omega_{\mathrm{DM}}^2}\,. \tag{7.4}$$

As discussed in section 6.2, the maximal gamma ray flux is possible in the scenario where $\Omega_{\psi_2} = 2\Omega_{\psi_1}$, corresponding to the values of the couplings

$$\begin{aligned} g_2 &= 1.4\times10^{-12}\sqrt{m_\Sigma/m_2}\,,\\ g_1 &= 9.9\times10^{-13}\sqrt{m_\Sigma/m_1}\,. \end{aligned} \tag{7.5}$$

However, these couplings cannot be chosen arbitrarily large without violating the out-of-equilibrium assumption $Y_i^{\mathrm{fi}} \ll Y_i^{\mathrm{eq}} \sim \frac{T^3 g_i/\pi^2}{g_{\mathrm{eff}}(T)T^3 2\pi^2/45}$ that is central to the freeze-in calculation:

$$|g_i| \lesssim 5\times10^{-9}\left(\frac{m_\Sigma}{\mathrm{GeV}}\right)^{1/2}\,, \tag{7.6}$$

which, using eqn. (7.5), translates into lower limits on the FIMP masses $m_1 \gtrsim 40\,\mathrm{eV}$, $m_2 \gtrsim 80\,\mathrm{eV}$. The dark matter warmness constraints on $m_{1,2}$ are analogous to those in section 6.2.

Figure 7.2 shows the maximal obtainable gamma ray signal, in terms of a lower limit on the inverse decay rate, for the process $\psi_2 \to \psi_1\gamma$ obeying the requirement that the relic density generated via freeze-in does not exceed the measured dark matter density, as a function of a mass of the decaying FIMP, m_2, for fixed values of the lighter FIMP mass m_1. The mass of the charged scalar Σ is fixed at $m_\Sigma = 430\,\mathrm{GeV}$ for concreteness (see section 7.2 for a discussion of bounds). These results are the same for all $l = e, \mu, \tau$.

The obtainable signals are contrasted with exclusion limits from the non-observation of a line in the isotropic gamma-ray flux [108, 178] or from constraints on exotic energy injection into the SM plasma during CMB decoupling [158] (see section 7.2.1). We find that the multicomponent fermionic FIMP scenario can be probed by current experiments, if the stable DM component is much lighter than the decaying one, $m_1 \ll m_2$. Concretely, we require *e.g.* $m_2 \gtrsim 3\,\mathrm{GeV}$ for $m_1 = 40\,\mathrm{eV}$, $m_2 \gtrsim 40\,\mathrm{GeV}$ for $m_1 = 100\,\mathrm{MeV}$, or $m_2 \gtrsim 90\,\mathrm{GeV}$ for $m_1 = 1\,\mathrm{GeV}$ for gamma ray signals at the reach of current experiments to be possible.

Note that nothing stops us from considering masses $m_1 < 40\,\mathrm{eV}$. The non-thermalisation requirement (eqn. 7.6) for the freeze-in calculation to be applicable just implies that in this case $\Omega_1^{\mathrm{FIMP}} \ll \Omega_{\mathrm{obs}}$. The following section considers couplings beyond the non-thermalisation value.

7.1.2 Thermalisation of the lighter species: FIMP + HDM

For couplings larger than the thermalisation bound (eqn. 7.6), the dark matter abundance Y_i reaches its equilibrium value Y_i^{eq} during its evolution in the early universe. The relic density is then determined not by freeze-in as considered up to here, but by *freeze-out*, i.e. the time when Y_i stops tracking the equilibrium abundance. Two regimes of freeze-out can be separated: relativistic freeze-out and non-relativistic freeze-out. In the relativistic case, the interactions between ψ_i and the SM bath are so weak that they freeze out long before the temperature drops below m_i. This implies that Y_i freezes at its relativistic equilibrium value (eqn. 5.40, repeated here for convenience)

$$Y_i^{\mathrm{eq,rel}} = \frac{n^{\mathrm{eq,rel}}(T_{\mathrm{fo}})}{s(T_{\mathrm{fo}})} \sim 0.42\cdot h_{\mathrm{eff}}^{-1}(T_{\mathrm{fo}})\,, \tag{7.7}$$

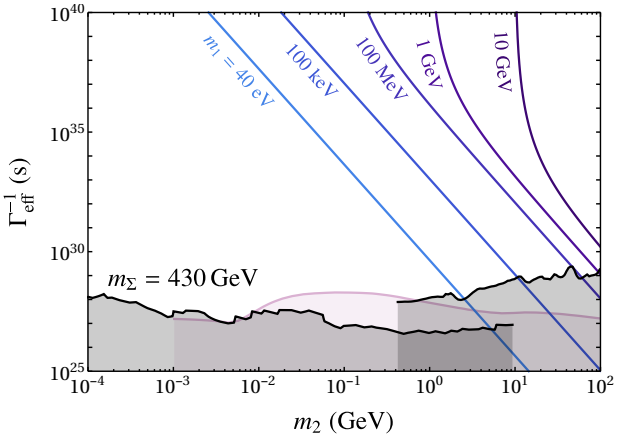

Figure 7.2: Maximal possible gamma ray signal in the fermionic multicomponent FIMP scenario, in terms of a lower limit on the inverse decay rate for $\psi_2 \to \psi_1\gamma$. This is shown as a function of the mass m_2 of the decaying FIMP component for different masses m_1 of the lighter component. The grey regions correspond to the lower limit on the inverse decay rate from the non-observation of a gamma ray line in the isotropic diffuse photon flux ([178] (left), [108] (right)). In the pink region, gamma ray signals in the model coupling to electrons, $l = e$, are precluded by CMB limits on the three body decay, as described in the text.

which results in the relic density (see eqn. 5.41)

$$\frac{\Omega_{1,\rm HDM}}{\Omega_{\rm DM,obs}} = 0.96 \left(\frac{m_1}{\rm eV}\right) h_{\rm eff}^{-1}(T_{\rm fo})\,, \tag{7.8}$$

assuming m_1 is large enough for ψ_1 to have become non-relativistic by the time of CMB decoupling. For larger coupling g_1, ψ_1 stays in equilibrium longer, resulting in a lower $T_{\rm fo}$, and finally a larger HDM abundance as $h_{\rm eff}(T)$ drops as the SM bath cools. Upper limits on the HDM relic density hence result in upper limits on the coupling g_1 and the decay rate $\Gamma_{\psi_2\to\psi_1\gamma}$.

Substituting the maximal $h_{\rm eff}^{\rm max} = 106.75$ attainable in the SM plasma into eqn. (7.8) results in an upper bound on the dark matter mass $m_1^{\rm HDM} \lesssim 110\,{\rm eV}$ from overabundance. This is significantly tightened by structure formation bounds on the fraction of hot dark matter: In [64], bounds on the fraction of non-cold dark matter $f_{\rm ncdm} = \Omega_{\rm ncdm}/(\Omega_{\rm cdm} + \Omega_{\rm ncdm})$ were obtained as function of the non-cold relic mass $m_{\rm ncdm}$. In the derivation of their bounds, they assume that the velocity distribution of non-cold dark matter is thermal with temperature equal to that of the Standard Model neutrinos, $T_{\rm ncdm} = T_\nu$, and prescribe to evaluate their constraints at $m_{\rm ncdm} = m\frac{T_\nu}{T}$ for dark matter of mass m with temperature T (i.e. at equal free-streaming length, see section 4.1), which in the case of HDM is related to the freeze-out temperature by $T_\nu/T = (h_{\rm eff}(T_{\nu-\rm dec})/h_{\rm eff}(T_{\rm fo}))^{-1/3}$. The resulting lower bound on the freeze-out temperature from the 3σ limits on $f_{\rm ncdm}$ obtained by [64] is shown in fig. 7.3. This implies an upper bound on the HDM mass, $m_1^{\rm HDM} \lesssim 20\,{\rm eV}$.

For very small m_1, ψ_1 contributes as dark radiation to the energy density,

$$\frac{\rho_{1,\rm DR}}{\rho_\gamma} = \frac{7}{8}\frac{T_{\psi_1,0}^4}{T_{\gamma,0}^4} = \frac{7}{8}\left(\frac{h_{\rm eff}(T_0)}{h_{\rm eff}(T_{\rm fo})}\right)^{4/3}\,, \tag{7.9}$$

using that $g_\gamma = 2$. Bounds on dark radiation are customarily given in terms of an equivalent excess number of neutrino species ΔN_{eff} [18]:

$$\Delta N_{\text{eff}} = \frac{8}{7}\left(\frac{11}{4}\right)^{4/3}\frac{\rho_1}{\rho_\gamma} = \left(\frac{11}{4}\right)^{4/3}\left(\frac{h_{\text{eff}}(T_0)}{h_{\text{eff}}(T_{\text{fo}})}\right)^{4/3} < 0.30\,. \tag{7.10}$$

This is satisfied if ψ_1 decouples before the QCD phase transition, $T_{\text{fo}} \gtrsim 160\,\text{MeV}$.

For both the HDM and DR cases, the relic density is inversely proportional to $h_{\text{eff}}(T_{\text{fo}})$. Bounds on the HDM/DR relic density hence relate to a lower bound on T_{fo}, which implies an upper bound on the coupling strength between the HDM/DR candidate and the SM bath. Freeze-out of ψ_1 is governed by the cross section $\sigma(\psi_1\psi_1 \to l^+l^-)$. We calculate this cross section numerically and find the thermally averaged cross section $\langle\sigma v\rangle \sim \frac{T^2 g_1^4}{4\pi m_\Sigma^4}$ for the relevant temperature range $m_l < T < m_\Sigma$. From the freeze-out condition $n_1(T_{\text{fo}})\langle\sigma v\rangle|_{T_{\text{fo}}} = H(T_{\text{fo}})$ (eqn. 5.39), we find:

$$T_{\text{fo}} = m_\Sigma \cdot 1.3\cdot 10^{-6}\left(\frac{m_\Sigma}{\text{GeV}} g_1^{-4}\sqrt{g_{\text{eff}}(T_{\text{fo}})}\right)^{1/3} \simeq 1.3\cdot 10^{-6}\,\text{GeV}\left(\frac{m_\Sigma}{\text{GeV}}\right)^{4/3} g_1^{-4/3} g_{\text{eff}}(T_{\text{fo}})^{1/6} \tag{7.11}$$

Using eqn. (7.11) together with the relic density results (7.8) and (7.10), upper bounds on the HDM fraction or ΔN_{eff} can be converted to upper bounds on the coupling g_1 as function of m_1. This is shown in Figure 7.3. Note that eqn. (7.11) assumes $m_l \ll T_{\text{fo}}$; if Σ couples to τ, the bound on g_1 can be relaxed due to the Boltzmann suppression of $\psi_1\psi_1 \to \tau\tau$ at $T < m_\tau$.

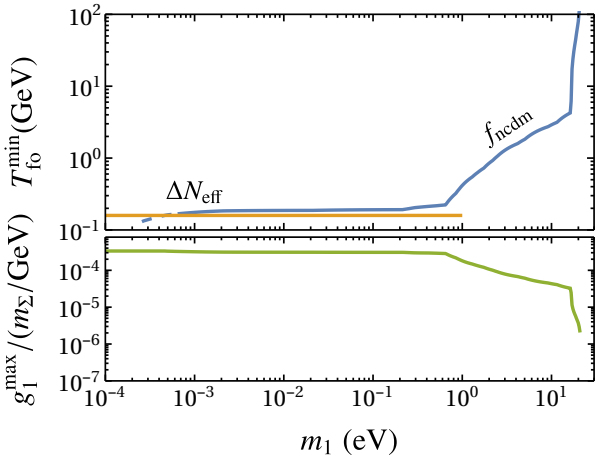

Figure 7.3: This plot shows the minimal allowed freeze-out temperature $T_{\text{fo}}^{\text{min}}$ (*top*) and the corresponding maximal allowed coupling g_1/m_Σ (*bottom*) as function of the dark matter mass m_1, for the case where ψ_1 decouples while relativistic. The bound from ΔN_{eff} [18] (orange) applies if ψ_1 is still relativistic at the time of CMB decoupling, and agrees well with the bounds on the fraction of non-cold dark matter (blue) obtained by [64] where applicable.

Using $g_1^{\text{max}}(m_1)$, we can extend the FIMP-FIMP results for the decay rate into gamma rays from Fig. 7.2 to the FIMP-HDM regime, where Ω_2 is determined by freeze-in and makes up the bulk of the dark matter density, while ψ_1 constitutes a subdominant hot dark matter component or contributes as dark radiation. The maximal attainable gamma-ray signals in

the FIMP-HDM scenario are shown in figure 7.4, using eqns. (7.3), (7.8) and (7.15). We find that allowing ψ_1 to thermalise and freeze-out as HDM allows for much larger FIMP decay rates, extending the range of m_2 (and correspondingly E_γ) for which dark matter decay signals at the reach of current experiments can be expected down to $m_2 \gtrsim 30\,\mathrm{MeV}$ for the largest allowed HDM mass, $m_1 = 20\,\mathrm{eV}$, and down to $m_2 \gtrsim 4\,\mathrm{MeV}$ for effectively massless ψ_1.

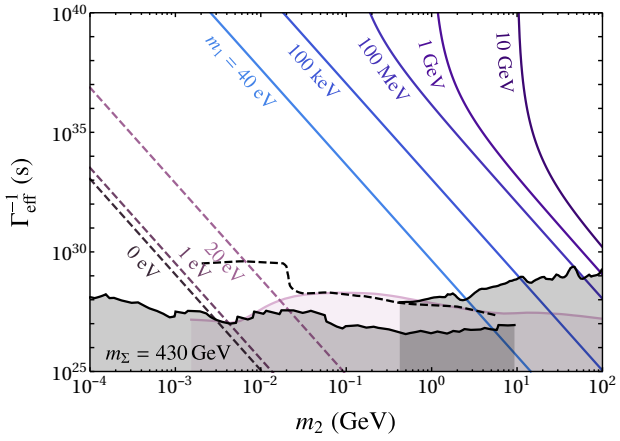

Figure 7.4: Maximal possible gamma ray signal in the fermionic multicomponent FIMP-FIMP (line) and FIMP-HDM (dashed) scenarios, in terms of a lower limit on the inverse decay rate for $\psi_2 \to \psi_1\gamma$. The lines correspond the maximal signals for fixed masses m_1 of the lighter component. The limits shown are the same as in Fig. 7.2, adding a sensitivity forecast for eASTROGAM [166] (black dashed).

This section has operated under the assumption of relativistic freeze-out, which implied $\lesssim \mathcal{O}\,(\mathrm{eV})$ masses (eqn. 7.8) for ψ_1 and resulted in couplings g_1 that exceed those associated with FIMP production by orders of magnitude. This can give rise to strong gamma ray signals from $\psi_2 \to \psi_1\gamma$ decay. In the following, we consider general couplings $g_{1,2}$, from values relevant to FIMP production up to the limit of the applicability of perturbation theory, $g_{1,2} < \sqrt{4\pi}$.

7.1.3 General relic abundances from FIMP to WIMP

In this section, we want to calculate the relic densities $\Omega_{1,2}$ for arbitrary values of the model parameters m_Σ, m_2, m_1, g_2, g_1. This necessitates treating the dark sector particles on equal footing, allowing for any combination of them to be out of chemical equilibrium with the others. The evolution of Σ and $\psi_{1,2}$ in the early Universe is determined by three coupled Boltzmann equations. Assuming kinetic equilibrium of all species involved[2], n_{Σ,ψ_2,ψ_1} obey

[2] The validity of this assumption in a related single-component DM model has been studied by [172], who find that the impact of deviations from kinetic equilibrium on the relic abundance is small (see however [180]).

the Boltzmann equations (see section 5.2)

$$\begin{aligned}\frac{dn_i}{dt} + 3Hn_i = &- \sum_j \langle\sigma v\rangle^{\text{ann}}_{ij\to AB}\left(n_i n_j - n_i^{\text{eq}} n_j^{\text{eq}}\right) \\ &- \sum_j \langle\sigma v\rangle^{\text{sca}}_{iA\to jB}\left(n_i n_A^{\text{eq}} - n_j n_B^{\text{eq}} \frac{n_i^{\text{eq}}}{n_j^{\text{eq}}}\right) \\ &- \sum_j \tilde{\Gamma}_{i\to j}\left(n_i - n_j \frac{n_i^{\text{eq}}}{n_j^{\text{eq}}}\right),\end{aligned} \tag{7.12}$$

where i, j refer to particle species in the dark sector while A, B refer to standard model particles that are assumed to form an equilibrium thermal bath. All particle distribution functions are approximated by Maxwell Boltzmann distributions. The $\langle\sigma v\rangle^{\text{ann}}_{ij\to AB}$ term describes annihilations of $\mathbb{Z}_2$-odd particles into Standard Model bath particles, while the $\langle\sigma v\rangle^{\text{sca}}_{iA\to jB}$ and $\tilde{\Gamma}_{i\to j}$ terms describe conversion processes between $\mathbb{Z}_2$-odd particles. Here $\langle\sigma v\rangle$ is the thermally averaged cross section (see section 5.2) and $\tilde{\Gamma}_{i\to j} = \Gamma_{i\to j}/\langle\gamma\rangle = \Gamma_{i\to j}\frac{K_1(m_i/T)}{K_2(m_i/T)}$ is the thermally averaged decay rate. As initial condition, $n_i(t \to 0) = 0$ is chosen to accommodate the freeze-in scenario discussed in the previous sections. In the WIMP scenario, there is no dependence on the initial condition, as the large (inverse) annihilation rate quickly equilibrates the WIMP species with the SM bath at $T > m_{\text{WIMP}}$.

In the freeze-out scenario, eqn. (7.12) is often simplified by asserting chemical equilibrium between the dark sector species,

$$n_i = n_{\text{dark}} \frac{n_i^{\text{eq}}(T)}{n_{\text{dark}}^{\text{eq}}(T)}, \tag{7.13}$$

where $n_{\text{dark}} = n_\Sigma + n_1 + n_2$, allowing to describe the whole system by a single differential equation for n_{dark}. Conversion terms in this summed Boltzmann equation drop out, and the annihilation terms can be summarised into a single $\langle\sigma v\rangle_{\text{eff}}$ that includes "coannihilation" contributions from all dark sector particles according to their relative abundances [137]. Since we want to calculate the dark matter relic abundance from the FIMP to the WIMP regime, the assumption of chemical equilibrium is not in general applicable, and the treatment here needs to go beyond that of standard numerical codes used in the calculation of relic abundances, like MICROMEGAS [126] or DARKSUSY [181].

7.1.3.1 Numerical solution of the Boltzmann equations

Eqn. (7.12) can be hard to solve numerically for several reasons. First, the particle densities n_i vary over many orders of magnitude. This can be remedied in part by considering instead an equivalent set of equations in terms of the abundances $Y_i = n_i/s$ as functions of $x = m_1/T$ (see section 5.2):

$$\begin{aligned}\frac{d\ln Y_i}{dx} = &- \sum_j \left[\frac{\langle\sigma v\rangle^{\text{ann}}_{ij\to AB} s Y_i \frac{Y_j^{\text{eq}}}{Y_i^{\text{eq}}}}{x\tilde{H}}\right]\left(\frac{Y_j}{Y_i}\frac{Y_i^{\text{eq}}}{Y_j^{\text{eq}}} - \frac{Y_i^{\text{eq}\,2}}{Y_i^2}\right) \\ &- \sum_j \left[\frac{\langle\sigma v\rangle^{\text{sca}}_{iA\to jB} s Y_A^{\text{eq}}}{x\tilde{H}} + \frac{\tilde{\Gamma}_{i\to j}}{x\tilde{H}}\right]\left(1 - \frac{Y_j}{Y_i}\frac{Y_i^{\text{eq}}}{Y_j^{\text{eq}}}\right).\end{aligned} \tag{7.14}$$

Second, some of the collision processes may happen on a much shorter timescale than the expansion of the Universe, leading to stiff differential equations. If a type of process [...] is fast compared to the Hubble expansion, it forces the associated abundances (...) to adopt a quasistatic equilibrium. Fast annihilations of particle i into bath particles fixes Y_i to follow its equilibrium abundance. Fast conversion processes between two particle species i, j ensure chemical equilibrium between them, $Y_i/Y_j = Y_i^{\mathrm{eq}}/Y_j^{\mathrm{eq}}$.

We can use these equilibrium relations to simplify the system eqn. (7.14): If conversion processes between two species are efficient, chemical equilibrium is ensured. Their abundances can be obtained by solving the summed Boltzmann equation for $d(Y_i + Y_j)/dx$ as $Y_i = Y_{i+j} \frac{Y_i^{\mathrm{eq}}}{Y_i^{\mathrm{eq}}+Y_j^{\mathrm{eq}}}$. This cancels any fast conversion rates and amounts to the usual coannihilation treatment [137]. As different combinations of species come into or drop out of chemical equilibrium with each other, the numerical code automatically determines whether to solve for their individual abundances $d\ln Y_i/dx$ or the summed Boltzmann equation for $d(Y_i + Y_j)/dx$.

The thermally averaged cross sections were calculated using FeynRules [156], CalcHEP [157] and micrOMEGAS [126]. Further details related to the numerical solution of the Boltzmann equations are discussed in Appendix A. In the following section, relic abundance results in the freeze-out scenario are presented, before discussing other constraints and signatures in the two component leptophilic dark matter scenario in section 7.2.

7.1.3.2 Production regimes of multiflavour leptophilic dark matter

Figure 7.5 shows relic abundance contours in the plane of couplings $g_{1,2}$ for the mass benchmark $m_\Sigma = 430\,\mathrm{GeV}$, $m_1 = 100\,\mathrm{GeV}$, $m_2 = 120\,\mathrm{GeV}$, illustrating the different mechanisms that can determine the final relic abundance.

Freeze-in vs. freeze-out One can clearly distinguish the regions where freeze-in or freeze-out determine the relic abundance of ψ_1 and ψ_2:

(A) *FIMP-FIMP:* In the lower left of the plot, both g_1,g_2 are below the thermalisation threshold eqn. (7.6) and their relic abundance is set by freeze-in.

(B) *FIMP-WIMP:* ψ_1 does not thermalise and behaves as FIMP, while ψ_2 does thermalise and freezes-out.

(C) *WIMP-FIMP:* ψ_2 does not thermalise and behaves as FIMP, while ψ_1 does thermalise and freezes-out.

(D) *WIMP-WIMP:* In the upper right of the plot, the couplings $g_{1,2}$ are large enough for both $\psi_{1,2}$ to thermalise and freeze-out.

In the FIMP-FIMP regime, the two abundances $Y_{1,2}$ evolve independently from one another, which has been discussed analytically in detail in section 7.1.1. We find good aggreement between the numerical and analytical solutions.

In the FIMP-WIMP regimes, the $Y_{1,2}$ evolution is not independent, but their interaction effects are rather simple: The feebly coupled partner does not affect WIMP freeze-out, but the thermalised component can affect the FIMP abundance if its coupling is very large. This can be understood from phase space arguments: In the analytic calculation in section 7.1.1, only two-body decays $\Sigma \to l\psi_i$ were assumed to contribute to freeze-in production. The

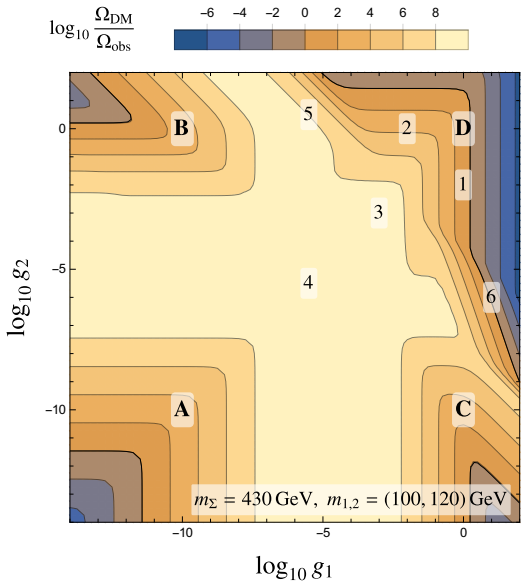

Figure 7.5: Relic abundance depending on the couplings g_1, g_2 for a benchmark choice of dark sector masses, $m_{1,2} = 100, 120$, $m_\Sigma = 430\,\text{GeV}$, evaluated at the time of CMB decoupling. Note that the plot extends beyond the range of validity into the non-perturbative regime ($g_{1,2} > \sqrt{4\pi}$) to highlight the different depletion mechanisms, which can result in the observed relic abundance with perturbative values for the couplings for different mass choices. The regimes labeled by letters A-D and numbers 1-6 are described in the text.

numerical treatment also includes conversion processes, such as $\psi_2 l \to \psi_1 l$, which can be seen to increase the relic abundance for very large coupling g_2. This is expected: The scattering contribution is suppressed wrt. the two-body decay one by a phase space factor and an additional coupling. When the coupling $g_{\rm WIMP}$ is larger than one, it can compensate the phase space suppression and $\sigma(\psi_{\rm WIMP} l \to \psi_{\rm FIMP} l) \propto g_1^2 g_2^2$ can dominate FIMP production.

The WIMP-WIMP scenario (D) exhibits several different regimes, indicated by numbers in fig. 7.5, which are discussed in detail in the following.

Production regimes of thermalised multiflavour leptophilic Dark Matter Several regimes can be distinguished, starting from those for which chemical equilibrium is maintained throughout freeze-out:

1. χ_1 *annihilation:* vertical contours at rather large g_1 for wide range of g_2. In this regime, the presence of ψ_2 is irrelevant to the relic abundance and the result is the same as in the standard single flavour textbook WIMP case, $\Omega_{\rm DM} \propto \langle\sigma v\rangle_{11}^{-1} \propto g_1^{-4}$ [1].

2. χ_2 *coannihilation:* horizontal contours at rather large g_2 for wide range of smaller g_1. $\psi_2\psi_2$-annihilation is the dominant dark sector depletion mechanism, leading to $\Omega_{\rm DM} \propto \langle\sigma v\rangle_{22}^{-1} \propto g_2^{-4}$ [137].

3. Σ *mediator coannihilation:* For small values of $g_{1,2}$, neither $\psi_2\psi_1$ nor $\psi_1\psi_1$ annihilation is efficient. Instead, mediator coannihilation depletes the dark sector, which can be efficient if the mediator mass is not too far from $m_{1,2}$ [137]. The relic density here is determined by the SM gauge couplings and roughly independent from $g_{1,2}$.

In these regimes, chemical equilibrium between the dark sector particles holds during freeze-out. We have compared results with MICROMEGAS [126], finding good agreement. The dedicated numerical treatment allows us to study relic abundances beyond chemical equilibrium, which affects the following regimes:

4. *Mediator conversion driven freeze-out:* The coannihilation plateau is bounded towards low couplings by rising relic abundances that are the result of ψ_i dropping out of chemical equilibrium with Σ before the dark matter abundance can be significantly depleted through Σ-coannihilations. This was first considered in [172, 180] and allows for thermalised dark matter with very small couplings, if the mass splitting between dark matter and the mediator is small.

5. $\psi_1 \to \psi_2$ *conversion driven freeze-out:* Likewise, the ψ_2 coannihilation region is bounded towards small g_1 by ψ_1 dropping out of chemical equilibrium with ψ_2 before ψ_2-driven coannihilation can effectively deplete the ψ_1 abundance. The relic abundance here depends on the conversion rate $\propto g_1^2 g_2^2$, resulting in the diagonal contours.

6. $\psi_2 \to \psi_1$ *conversion driven freeze-out:* At small g_2, ψ_2 becomes long lived and the dominant reaction depleting the relic abundance is $\psi_1\psi_1$ annihilation. The relic abundance results from an interplay of $\psi_2 \to \psi_1$ conversion, out-of-equilibrium decay of ψ_2 and ψ_1 annihilation.

The effect of departure from chemical equilibrium is shown in Figure 7.6, illustrating how decoupling of conversion processes in regimes 4-6 makes the depletion of dark matter abundance less effective, leading to larger relic densities. The abundance evolution $Y_i(x)$ for several illustrative benchmark points is shown in Figure 7.7.

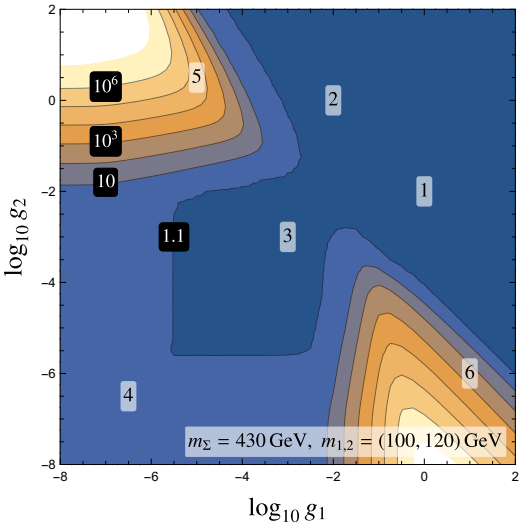

Figure 7.6: Effect of departure from equilibrium on the relic abundance in the WIMP-WIMP scenario, showing $(\Omega_{\mathrm{full-calc}}/\Omega_{\mathrm{assumed-CE}})$-contours (black boxes). The mass benchmark is the same as in fig. 7.5. This plot illustrates chemical equilibrium conditions to be fulfilled in production regimes 1-3, while in regimes 4-6 deviation from chemical equilibrium among the dark sector particles can be very important.

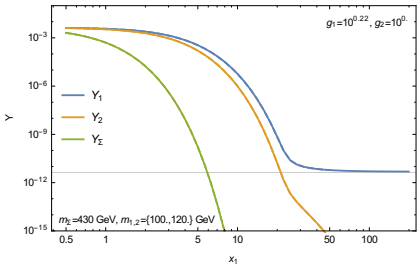

(a) *Standard WIMP:* Chemical equilibrium holds throughout.

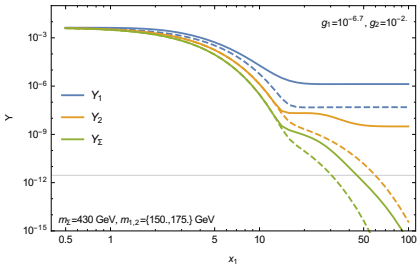

(b) *Mediator conversion freeze-out:* The relic abundance is determined by the rate of $\psi_i \to \Sigma$ conversion.

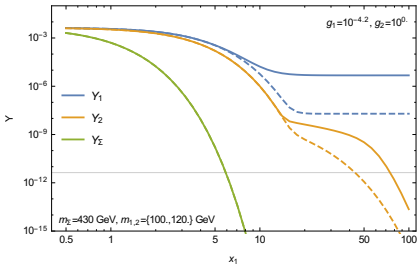

(c) $\psi_1 \to \psi_2$ *conversion:* The relic abundance is determined by the rate of conversion from the lighter to the heavier flavour.

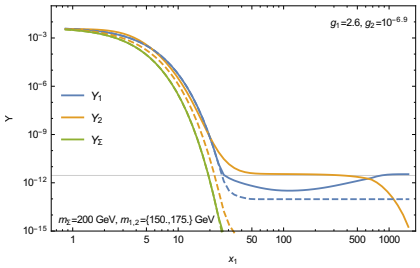

(d) $\psi_2 \to \psi_1$ *conversion:* The relic abundance is determined by the rate of conversion from the heavier to the lighter flavour. The abundance evolution illustrates that this effect goes beyond late decay of ψ_2.

Figure 7.7: Abundance evolution $Y_i(x)$ for several benchmark points, illustrating the WIMP-WIMP production regimes discussed in the text. Dashed contours assume chemical equilibrium to indicate where departure from CE becomes important. The left column uses the same mass benchmark as fig. 7.5, the right column assumes a more compressed mass spectrum to highlight conversion processes.

Discussion Processes 1-3 are the domain of standard numerical codes, and process 4 has been described in detail in the literature [140, 172, 180]. The regimes 5 and 6 are specific to the two-flavour setup. χ_2-conversion driven freeze-out (5) is a straightforward extension of mediator-conversion driven freeze out (4).

The interplay of several processes determines the relic abundance in regime 6: Contributions to the relic abundance from a late-decaying particle have been considered before. If the decay of ψ_2 happens long after ψ_1 has frozen out and does not revive ψ_1 annihilation, the effect of ψ_2 is a simple additive contribution to the freeze-out Ω_1 result (akin to the super-WIMP contribution [159, 160] in the FIMP case, see eqn. (6.12) in section 6.2). This limit has been investigated in a 2-component WIMP scenario without scattering conversion by [182]. Fig. 7.7d shows that out-of-equilibrium conversion and decay of $\psi_2 \to \psi_1$, as well as ψ_1-annihilation need to be considered together to determine the relic abundance in regime 6.

Summarising the relic abundance calculation, we find that several different processes can be crucial in determining the result for two-flavour leptophilic dark matter. Compared to the single flavour case, the additional freedom in the model results on one hand in reduced predictivity, while on the other hand leading to novel signatures that cannot appear in the single flavour case. From the relic abundance calculation alone, it is already possible to point out one such qualitative difference: For freeze-out in regime 6, obtaining the correct relic abundance implies larger coupling g_1 than in the single flavour case, potentially explaining observations of annihilating dark matter in our galaxy that require $\langle\sigma v\rangle > \langle\sigma v\rangle_{\text{std.WIMP}}$. This was investigated in a related setup as a possible explanation of the PAMELA positron excess in [182] and is discussed in detail in section 7.2.2.2.

7.2 Signatures of multi-flavour leptophilic Dark Matter

This study of multi flavour Dark Matter in the leptophilic fermion model was motivated in the beginning by the possibility of decay signals in the FIMP framework in a model that is notoriously hard to probe, in analogy to multiflavour scalar dark matter considered in chapter 6. Dark matter decay is discussed in section 7.2.1, addressing in particular the question under which circumstances dark matter today can consist of multiple components. Consequences of the two-flavour setup for standard WIMP searches for dark matter annihilation in the Galaxy are explored in section 7.2.2. Finally, the presence of the second flavour in the theory can affect signatures at collider experiments, which is explored in section 7.2.3, where other laboratory constraints are also discussed.

7.2.1 Dark matter decay

In investigating how the second flavour affects dark matter phenomenology, a central question is under what circumstances both dark matter candidates can be present at a given time. This is related both to the initially produced abundances and to the ψ_2 lifetime, i.e. whether an abundance of ψ_2 produced in the early universe survives to the time of BBN, recombination or today.

We consider both the tree-level three-body decay $\psi_2 \to \psi_1 l^+ l^-$, which generally dominates the total decay rate, as well as the one-loop decay $\psi_2 \to \psi_1 \gamma$, which leads to monochromatic gamma rays that can be easily separated from astrophysical background fluxes and would constitute a smoking-gun signature of BSM particle physics processes, if observed. Feynman diagrams for both processes are shown in fig. 7.1. The decay rate for the one-loop

decay $\psi_2 \to \psi_1\gamma$ in the limit $m_{\psi_2} \ll m_\Sigma$ reads [183]:

$$\Gamma_{\psi_2\to\psi_1\gamma} = \frac{e^2|g_1 g_2|^2}{2^{15}\pi^5}\frac{m_{\psi_2}^5}{m_\Sigma^4}\left(1-\frac{m_1^2}{m_2^2}\right)^3\left(1-\frac{m_1}{m_2}\right)^2 , \tag{7.15}$$

producing gamma rays at energy

$$E_\gamma = \frac{m_{\psi_2}}{2}\left(1-\frac{m_{\psi_1}^2}{m_{\psi_2}^2}\right) . \tag{7.16}$$

The three-body decay rate in the limit $m_l \ll m_{\psi_2} \ll m_\Sigma$ is given by [183]

$$\Gamma_{\psi_2\to l^+l^-} = \frac{|g_1 g_2|^2}{2^{10}\pi^3 3}\frac{m_{\psi_2}^5}{m_\Sigma^4}\left(F_1(m_{\psi_1}^2/m_{\psi_2}^2)+2F_2(m_{\psi_1}^2/m_{\psi_2}^2)\right) , \tag{7.17}$$

with

$$F_1(x) = (1-x^2)(1-8x+x^2) - 12x^2\ln(x) \tag{7.18}$$

$$F_2(x) = \sqrt{x}\left[(1-x)(1+10x+x^2)+6x(1+x)\ln(x)\right] . \tag{7.19}$$

Depending on the dark matter lifetime, different signatures are of interest:

- $10^{-12}\,\mathrm{s} \lesssim \tau_{\psi_2} \lesssim 10^{-5}\,\mathrm{s}$: ψ_2 can leave displaced signatures at colliders ($1\,\mathrm{mm} \lesssim c\tau_{\psi_2} \lesssim 1\,\mathrm{km}$). At smaller decay lengths, ψ_2 effectively decays promptly, while at larger decay lengths, it escapes undetected.

- $\tau_{\psi_2} \ll 1\,\mathrm{s}$: ψ_2 decays well before BBN and leaves no signature except as a contribution to the ψ_1 abundance.

- $\tau_{\psi_2} \gtrsim 1\,\mathrm{s}$: exotic energy injection from particle decay can modify the primordial abundances of light elements in Big Bang Nucleosynthesis [163] and lead to (for $\tau_{\psi_2} \gtrsim 10^6\,\mathrm{s}$) spectral distortions of the CMB [184].

- $\tau_{\psi_2} \gtrsim 10^{12}\,\mathrm{s}$: ψ_2 is long lived enough to contribute to the dark matter relic density measured by the CMB, and its decay products can modify the ionization history between recombination and reionisation, affecting CMB angular power spectra [158, 185].

- $\tau_{\psi_2} \gtrsim 10^{18}\,\mathrm{s} \sim t_{\mathrm{Univ}}$: ψ_2 is cosmologically long lived and can be a relevant component of dark matter today. Its decay products can potentially be observed as gamma/cosmic rays.

In the following, we look at bounds on the pre-BBN abundance of ψ_2 depending on τ_{ψ_2}.

Exotic energy injection in the early universe Big Bang nucleosynthesis describes the formation of light nuclei when the SM bath has cooled down far enough to allow formation to dominate over dissociation. Given information on the nuclear reaction rates, the resulting 'primordial' abundance of light elements can be predicted within standard cosmology and compared to the abundances observed in situation where modification through astrophysical processes is considered not to have taken place. Theoretical predictions and observations

for ^{2}H, ^{3}He and ^{4}He agree well and are compatible with the baryon abundance determined from the CMB, which is the earliest cosmic evidence for ΛCDM [163] (see sec. 2.2).

Energetic particles produced in BSM particle physics processes during BBN can modify the neutron to proton ratio or dissociate nuclei, leading to deviations from the successful predictions of standard Big Bang nucleosynthesis. Limits on the abundance Y_X of decaying particles X producing SM particles of energy ϵ with decay rate τ_X have been computed e.g. by [163, 186].

Similarly, energetic particles present during CMB decoupling can induce deviations from the black body spectrum, on which there exist tight constraints [184]. The CMB angular power spectrum is affected by the ionisation history of the universe, which can be modified by energetic particles through ionisation and heating of the primordial gas. Constraints on exotic energy injection from decaying dark matter during the cosmic dark ages have been derived in [158, 185]. These constraints extend to lifetimes much longer than the age of the Universe.

Figure 7.8 shows limits on exotic energy injection from dark matter decay in terms of the pre-decay abundance Y_X and the energy ϵ injected into $e^{\pm}$ per decay, as a function of the lifetime τ_X of the decaying particle.

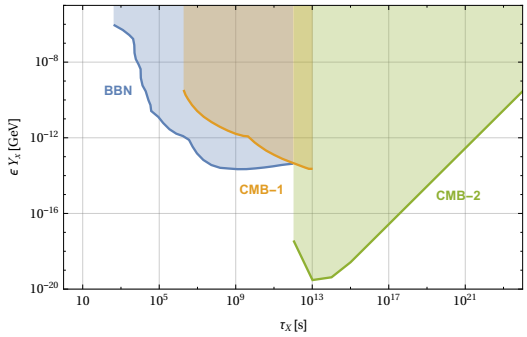

Figure 7.8: Limits on exotic energy injection from dark matter decay, in terms of an upper limit on the pre-decay abundance Y_X of a particle decaying with lifetime τ_X, injecting energy ϵ into electrons/positrons. *Blue:* BBN limit [186] for $\epsilon = 10\,\mathrm{GeV}$ (slightly weaker limits result for $\epsilon \ll$ GeV). *Orange:* Limits from CMB spectral distortion [184] (via [185]). *Green:* Limit from exotic energy injection after CMB decoupling [185] (taking the least constraining limits). These limits are rather general and only very mildly dependent on the electron/positron energy.

Gamma ray line search Going beyond the cosmological constraints on fairly generic exotic energy injection discussed above, features in the gamma ray or positron spectra observed today may serve as smoking-gun evidence of dark matter decay or annihilation (see section 4.3).

In particular, the process $\psi_2 \to \psi_1\gamma$ results in a gamma ray line that easily stands out against the smooth power law spectra typical of astrophysical sources. We consider limits on dark matter decay into monochromatic gamma rays calculated in [178] based on measurements by the INTEGRAL [152], COMPTEL [153], EGRET [154] and Fermi-LAT [155] instruments, as well as a dedicated line-search by the Fermi-LAT collaboration [108]. Future gamma-ray telescopes like the proposed AMEGO [165] or e-ASTROGAM [166, 167] mission concepts can improve the sensitivity by an order of magnitude in the $\sim 0.3 - 30\,\mathrm{MeV}$ mass range.

Figures 7.2 and 7.4 illustrate the prospects of detecting gamma rays from decaying dark matter in the FIMP-FIMP and FIMP-HDM scenarios, respectively. These results are in direct analogy to those found for scalar multicomponent FIMPs found in chapter 6. Shown are lower limits on the effective inverse decay rate $\Gamma_{\text{eff}}^{-1} = (\Gamma\Omega_2/\Omega_{\text{DM}})^{-1}$, i.e. maximal obtainable gamma ray signals.

These can be compared to constraints on the associated three body decay $\psi_2 \to \psi_1 e^+ e^-$. In Figs. 7.2, 7.4, the pink shaded are indicates where gamma ray signals are ruled out in the present setup with $l = e$ by limits on the rate of the associated three body decay $\psi_2 \to \psi_1 e^+ e^-$ from the non-observation of exotic energy injection into the SM plasma during CMB decoupling [158] (recast to the associated gamma ray decay rate using results from [183]). We note that at mass differences $m_2 - m_1 \gtrsim 10\,\text{GeV}$, searches for the associated spectral feature in the spectrum of cosmic ray positrons are promising (see e.g. [187, 188] for existing searches for positron spectral features) and complementary to the gamma ray signatures we focus on here.

Discussion Constraints on the dark matter decay rate throughout cosmic history are shown in fig. 7.9, together with the overabundance constraint for the adopted mass benchmark, as well as the perturbativity requirement $g_i \lesssim \sqrt{4\pi}$. The parts of parameter space where only one of the two flavours thermalises are severely constrained by perturbativity and BBN constraints. Only if the decaying dark matter fraction is suppressed by a small FIMP production rate (lower right of plot) can this mixed production be viable. Perturbativity bounds imply that out of the six different processes that can be responsible for setting the WIMP-WIMP relic abundance, only ψ_1-annihilation driven and $\psi_2 \to \psi_1$-conversion driven dark matter depletion are compatible with the abundance constraint for this mass benchmark. As already expected from fig. 7.2, γ-ray searches are not yet sensitive to the FIMP-FIMP regime for the adopted particle masses.

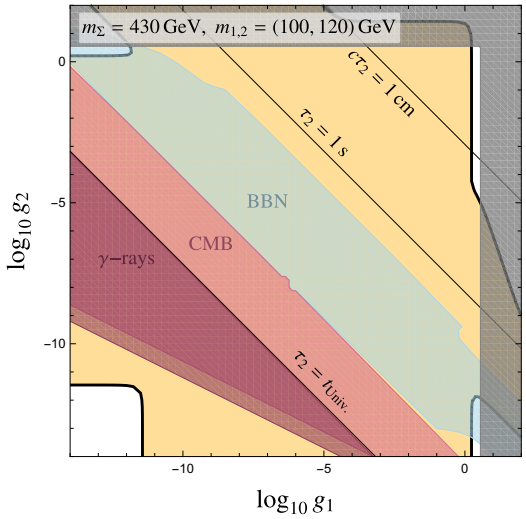

Figure 7.9: Overabundance constraints from fig. 7.5, with decay constraints (BBN, CMB, γ-ray flux), as well as perturbativity requirements $g_i \lesssim \sqrt{4\pi}$ (gray) superimposed.

7.2.2 Dark matter annihilation signatures

Dark matter annihilation in overdense regions in the Universe today is a central prediction of the WIMP framework, while it is of little relevance in the FIMP scenario. In the WIMP-WIMP regime, the ψ_2 lifetime is short[3] and dark matter today consists exclusively of ψ_1. The dark matter annihilation signature is then expected to be qualitatively similar to the single flavour case, however with striking quantitative differences. In the following, the single-flavour annihilation signatures are reviewed briefly, before investigating the role of ψ_2 in the range of possible annihilation signals.

7.2.2.1 Annihilation signatures in the leptophilic model

The leptophilic model we discuss has been investigated in detail for its possible annihilation signatures (see e.g. [107,168,174]), motivated in part by the possibility of distinctive gamma-ray signatures.

The dominant annihilation process in determining the relic abundance in the freeze-out regime is the $2 \to 2$ annihilation $\psi_1\psi_1 \to l^+l^-$. While the dark matter particles are only mildly non-relativistic at freeze-out, typical velocities in galaxies today are small, and the velocity-weighted annihilation cross section can be expanded in relative (center-of-mass) velocity [107]:

$$(\sigma v)^{\text{non-rel.}}_{\psi_1\psi_1\to l^+l^-} \simeq \underbrace{\frac{g_1^4}{32\pi m_1^2}\frac{m_l^2}{m_1^2}\frac{1}{(1+m_\Sigma^2/m_1^2)^2}}_{s-\text{wave}} + \underbrace{v^2\frac{g_1^4}{48\pi m_1^2}\frac{1+m_\Sigma^2/m_1^2}{(1+m_\Sigma^2/m_1^2)^4}}_{p-\text{wave}} . \tag{7.20}$$

Note that the s-wave term is strongly helicity suppressed,[4] and while the velocity suppression of the p-wave contribution is not very strong during freeze-out ($\langle v_{\text{rel}}^2\rangle \sim 0.3$ at $x \sim 20$ [189]), it amounts to a strong suppression in our Galaxy today ($v \sim 10^{-3}$) [190]. For this reason, the strong constraints from cosmic ray positron data on dark matter annihilation into l^+l^- (e.g. [187,188]) do not translate into strong constraints on g_1.

Stronger constraints are instead obtained by considering the concurrent emission of a photon, $\psi_1\psi_1 \to l^+l^-\gamma$ from the t-channel Σ particle (virtual internal bremsstrahlung, VIB), which removes the helicity suppression of the s-wave process and moreover can give rise to distinctive signals in the form of sharp gamma ray spectral features if the mediator mass is close to the dark matter mass, $\mu \equiv m_\Sigma^2/m_1^2 \simeq 1$ [107,191]. The formula for the annihilation cross section into two massless fermions and one VIB photon reads [107]:

$$\begin{aligned}(\sigma v)_{\text{VIB}} \simeq \frac{\alpha g_1^4}{64\pi^2 m_1^2}\Bigg((1+\mu)\left[\frac{\pi^2}{6} - \log\left(\frac{1+\mu}{2\mu}\right) - 2\,\text{Li}_2\left(\frac{1+\mu}{2\mu}\right)\right] \\ + \frac{4\mu+3}{1+\mu} + \frac{4\mu^2-3\mu-1}{2\mu}\log\left(\frac{\mu-1}{\mu+1}\right)\Bigg) .\end{aligned} \tag{7.21}$$

This annihilation signature has been searched for by Bringmann et.al. [107] in the gamma ray sky observed by Fermi-LAT [86], obtaining limits and an indication of a signal at $m_{\text{DM}} \simeq$

[3] As the dark matter decay rate depends sensitively on the mass splitting, this is not necessarily the case for very degenerate mass spectra, which are an interesting target for future work.

[4] This can be understood from angular momentum conservation: The Majorana fermions in the s-wave initial state need to have opposite spins, i.e. zero angular momentum. The Yukawa interaction couples to the right-chiral leptons, needing one mass insertion on a final state lepton to result in same-helicity products and conserve angular momentum. [174]

150 GeV, $\langle\sigma v\rangle^{\rm obs}_{\rm VIB} \sim 6\times10^{-27}\,{\rm cm}^3\,{\rm s}^{-1}$. This is about two orders of magnitude larger than what would be expected from reproducing the observed relic abundance in the present framework, raising questions about its possible dark matter origin. In the time since the analysis of [107], more data has been collected, finding that this particular signal (which could also be explained by a gamma ray line at 130 GeV) is not significant any more [108]. Below, we take this now-gone statistical fluctuation as illustration for the possibility of boosting dark matter annihilation in the present scenario.

If the mass of the mediator is much larger than the dark matter particle, loop-induced annihilation into a photon pair may dominate the annihialtion signal today with annihilation cross section [171]

$$(\sigma v)_{\gamma\gamma} = \frac{\alpha^2 g_1^4}{256\pi^3 m_1^2}\left[{\rm Li}_2\left(-\frac{m_1^2}{m_\Sigma^2}\right) - {\rm Li}_2\left(\frac{m_1^2}{m_\Sigma^2}\right)\right]^2 , \tag{7.22}$$

which is not yet constraining for perturbative values of g_1 for the mass benchmarks considered [108].

7.2.2.2 Annihilation boosts from a second DM flavour

Signals from dark matter annihilation into high energy particles are a key prediction of the thermal freeze-out scenario. In the standard WIMP framework, the velocity averaged annihilation cross section $\langle\sigma v\rangle_{\rm today}$ in overdense structures today is related directly to the thermally averaged annihilation cross section $\langle\sigma v\rangle_{\rm freeze-out}$, either by equality (in the case of s-wave annihilation) or by the velocity dependence in a given model. It is then a nontrivial question to ask whether a tentative dark matter signal is compatible with the "thermal" value $\langle\sigma v\rangle_{\rm WIMP} \simeq 3\times10^{-26}\,{\rm cm}^3\,{\rm s}^{-1}$ (see sec. 5.3), or whether the WIMP framework is ruled out if upper limits exclude this value.

There are a multitude of ways in which the annihilation signal could be decreased below the thermal value, masking a WIMP from annihilation searches. The simplest are velocity suppression of the annihilation cross section, or the presence of multiple annihilation channels that decrease the cross section into the SM final states of interest to a given search [192]. Another way is if there are multiple dark sector species that can deplete the dark matter abundance through co-annihilation channels if they are close in mass [137], as is possible in the present model.

Conversely, it is also interesting to ask whether a dark matter annihilation signal today can exceed the canonical WIMP expectation. The most prominent example is the positron excess observed by PAMELA [193] and ATIC [194], which required a *boost factor* of several orders of magnitude to be compatible with a dark matter origin [195, 196]. This has focused interest on the expected astrophysical boost factor from dark matter substructure, $\langle\rho^2\rangle \geq \langle\rho\rangle^2$ (found to be very unlikely to amount to the necessary boost in Galactic DM searches [197]), and established the importance of Sommerfeld enhancement in dark matter relic abundance and annihilation signal studies (e.g. [198–200]).

These boosting strategies directly affect the dark matter annihilation rate today. As we have seen in figure 7.5, the presence of the second dark matter flavour in the theory can strongly affect the relations between the relic abundance and the coupling g_1 that is central to the WIMP annihilation signature today. This is illustrated in Figure 7.10 for the (now gone) gamma ray signal [107] introduced in the previous section, where the cross section that is implied by reproducing the observed relic abundance in the single flavour model falls short of what was needed to explain the excess by orders of magnitude. In the

two-flavour scenario however, the $\psi_2 \to \psi_1$ conversion freeze-out dominated regime (regime 6 in section 7.1.3.2) results in larger predicted g_1, making the signal compatible with a dark matter origin.

The idea of boosting the dark matter annihilation rate compatible with the relic abundance through a late decaying particle has been investigated by [182], motivated by the PAMELA excess. Their treatment assumes the absence of scattering conversion between dark matter species, treating ψ_1 and ψ_2 freeze-out, as well as ψ_2 decay as independent. In constrast, in the present two-flavour realisation of this general idea, all possible $\psi_i\psi_j$ annihilation and decay processes are linked by the same two couplings $g_{1,2}$. Fig. 7.7d explicitly shows a benchmark case reproducing the observed relic abundance and the gamma ray signal found by [107], illustrating the importance of scattering conversion.

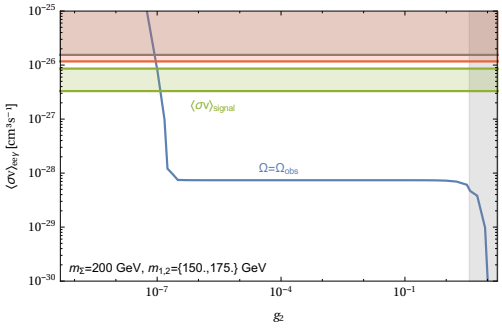

Figure 7.10: Example for annihilation boosts obtainable in the two-flavour framework for benchmark parameters that can explain the spurious signal found in [107]. The blue contour shows the prediction for $\langle\sigma v\rangle_{\rm VIB}$ from the relic abundance requirement, as a function of g_2. The central plateau corresponds to the ψ_1-annihilation freeze-out regime, where the relic abundance is unaffected by the presence of ψ_2. At large g_2, ψ_2 co-annihilation becomes relevant, suppressing the expected signal. At small ψ_2, larger couplings g_1 are required to deplete the out-of-equilibrium ψ_2 particles, accommodating the large observed annihilation signal today (green). The upper limit for $\langle\sigma v\rangle_{\rm VIB}$ is shown in red [107]; grey areas mark couplings exceeding the perturbativity limit $g_i < \sqrt{4\pi}$. The abundance evolution for a benchmark point compatible with the observed signal is shown in Figure 7.7d.

7.2.3 Laboratory searches

While the focus of this work is on implications of the multi-flavour scenario on dark matter indirect detection, collider searches set a lower limit for the mass of the charged mediator and can potentially directly probe dark matter in the laboratory. In section 7.2.3.1 we outline the basic strategies to search for leptophilic dark matter or the charged mediator at colliders and how these searches are affected by the presence of the second DM flavour. We comment on non-collider laboratory tests of the model in section 7.2.3.2.

7.2.3.1 Collider searches

Direct dark matter production Pair production of dark sector particles can be probed at colliders by looking for events where Standard Model particles recoil against missing transverse momentum carried away by the dark matter candidate. The two dark matter flavours can contribute separately, and monophoton searches at LEP [111] can be sensitive

to ψ_i if their mass is within its kinematic reach, $m_i \lesssim 100\,\text{GeV}$.[5]

At hadron colliders, tree-level production of leptophilic dark matter needs to proceed through pair production of the charged mediator Σ, which is very suppressed if the mediator cannot go on mass shell. If the mediator is at the kinematic reach of the collider, searches for new charged particles can be a sensitive probe of the leptophilic scenario.

Prompt searches for the mediator The collider signatures of the charged scalar Σ depend crucially on its decay length (eqn. 7.2)

$$c\tau_\Sigma \sim 10^{-16}\,\text{m}\,\left(\frac{m_\Sigma}{100\,\text{GeV}}\right)^{-1}(\max[g_1,g_2])^{-2} \tag{7.23}$$

which can be enhanced in the case of mass degeneracy $m_i \sim m_\Sigma$. Comparing this to the minimal coupling that leads to thermalisation of ψ_i in the early universe, eqn. (7.6), indicates that Σ may decay promptly if at least one species ψ_i thermalises in the early Universe, while it is long-lived on collider scales in the FIMP-FIMP regime.

At the LHC, searches for supersymmetric partners of leptons, *sleptons* $\tilde{l}$, have been conducted [115,116,201–206]. These are directly applicable to the leptophilic charged scalar Σ, which can be pair-produced from virtual photons/Z-bosons in pp-collisions. These searches look for oppositely charged, same-flavour leptons produced in association with missing transverse momentum p_T^{miss}. Selection cuts on the transverse momentum of the produced leptons (e.g. $p_T > 50(20)\,\text{GeV}$ for the (next-to) highest p_T lepton [115]) imply that this strategy is only sensitive to Σ decays for sufficiently split $m_\Sigma - m_i \gtrsim 50\,\text{GeV}$. A CMS search [115] using $35.9\,\text{fb}^{-1}$ of data at 13 TeV bounds $m_{\tilde{e}}^R \gtrsim 240\,\text{GeV}$ unless $m_{\text{LSP}} \gtrsim \min(70, m_{\tilde{e}} - 110)\,\text{GeV}$ and $m_{\tilde{\mu}}^R \gtrsim 210\,\text{GeV}$ unless $m_{\text{LSP}} \gtrsim \min(70, m_{\tilde{\mu}} - 100)\,\text{GeV}$. This translates directly to constraints on $m_\Sigma = m_{\tilde{l}}^R$, $m_i = m_{\text{LSP}}$, assuming Σ dominantly decays into ψ_i, $\text{Br}(\Sigma \to \psi_i l) \sim 1$. A corresponding ATLAS search [116] finds similar limits up to $m_{\tilde{l}} \lesssim 500\,\text{GeV}$ but only reports the results assuming $\tilde{e}_{R,L}, \tilde{\mu}_{R,L}$ to be degenerate in mass. As τ decays predominantly hadronically, a different search strategy is required for $l = \tau$. An ATLAS search for staus [205] uses $139\,\text{fb}^{-1}$ of luminosity collected at 13 TeV, excluding degenerate stau masses up to $m_{\tilde{\tau}_{LR}} \lesssim 390\,\text{GeV}$ in the limit of small dark matter mass.

All these searches assume prompt Σ decay into dark matter plus a visible final state particle with sufficient energy to pass selection criteria. They quickly loose sensitivity if the masses of decay products in the dominant decay channel approach m_Σ (in practice, already for $m_\Sigma - m_\psi \lesssim 100\,\text{GeV}$).[6] In the two-flavour setup, either dark matter flavour may dominate the decay rate of Σ, and it is possible that a large decay rate into ψ_2 with $m_2 \sim m_\Sigma$ hides the charged mediator from LHC detectability.

Long-lived mediator searches If all dark matter flavours are only feebly coupled to Σ, the mediator is stable on collider timescales and bounds on anomalously heavy charged particles apply[7]. Long-lived charged scalars produced by direct pair production are constrained

[5] The authors of [111] find that thermal Dirac fermion dark matter can be constrained for masses up to 50 GeV for coupling to electrons, indicative of the possible bounds for Majorana dark matter considered here. Dark matter coupling exclusively to μ, τ can not be produced at tree-level at LEP.

[6] Separate strategies are applied to target the mass-degenerate region [203].

[7] Bounds on the charged mediator mass depending on $c\tau$ have been compared in detail by [113] for a fermionic charged mediator. They include bounds on searches for displaced leptons dominant at $c\tau \sim$ cm scales, searches for disappearing charged tracks dominant at $c\tau \sim$ m and heavy stable charged particles (HSCPs) at $c\tau \gtrsim$ m. Here we contend ourselves with HSCP bounds, as these are the most relevant for FIMP dark matter scenarios with $m_{\text{FIMP}} \gtrsim \mathcal{O}(100\,\text{keV})$ [113].

to be more massive than $m_\Sigma > 430\,\text{GeV}$ [117]. This is currently the strongest constraint on m_Σ, and we take it as benchmark value for many of the results above.

Freeze-in production in the present model is directly linked to the mediator lifetime by eqn. (5.52). This has prompted hope for direct tests of the freeze-in scenario at colliders by observing the Σ decay length [113]. However, the relatively large decay rate implied by decay within the LHC detectors implies dark matter overproduction, unless the FIMP mass is in the keV range [113,207,208][8]. This seems to thwart hopes to positively identify freeze-in via heavy SM-charged mediators at the LHC by inferring the dark matter abundance from the mediator decay length and the invisible particle mass from the displaced vertex event kinematics (e.g. [144, 209]).

Long-lived neutral particles In the two-flavour scenario, displaced decays of the heavier dark matter candidate to the lighter one can be searched for at colliders. Displaced e^+e^-, $\mu^+\mu^-$ pairs have been looked for at ATLAS [210–212] and CMS [213]. They are sensitive to mm $\lesssim c\tau_{\chi_2} \lesssim 10^2\,\text{m}$ if $m_2 - m_1$ is sufficient to pass cuts on the lepton energy. The search for $\psi_2 \to \psi_1 l^+ l^-$ is complementary to the search for the mediator Σ in the sense that they are sensitive to different mass spectra, with similar reach in production cross section. Further work is necessary to determine whether these searches, possibly extended to larger $c\tau_{\psi_1} \sim$ km by MATHUSLA [214] in the future, can probe relevant parameter space in the two-flavour leptophilic dark matter model.

7.2.3.2 Dark matter direct detection and SM precision tests

Besides indirect signatures of dark matter in cosmological/astrophysical settings and collider production of the particles that make up dark matter, other laboratory probes of the leptophilic model exist.

Dark matter direct detection experiments look for galactic dark matter scattering off detector material. Current constraints on dark matter - electron scattering [215], which is possible at tree-level in the leptophilic scenario, are not sensitive enough to surpass perturbativity requirements for non-degenerate mass spectra. At loop-level the leptophilic Majorana fermions ψ_i may scatter with nuclei through an anapole moment, which can yield relevant constraints for very degenerate $m_\Sigma^2 \lesssim 1.1 m_{\text{DM}}^2$ [174].

Independently from the dark matter nature of $\psi_{1,2}$, their presence in the theory modifies lepton precision observables. We impose that Σ couples to only one lepton flavour to avoid lepton flavour violation. This flavour diagonal coupling can then still modify the lepton magnetic moments, giving a contribution to the $(g_l - 2)/2$ of

$$\Delta a_{l,i}^{\text{DM}} = -\frac{g_i^2}{16\pi^2}\frac{m_l^2}{m_i^2}\frac{2 + 3\mu_i - 6\mu_i^2 + \mu_i^3 + 6\mu_i \log \mu_i}{6(\mu_i - 1)^4} \tag{7.24}$$

with $\mu_i = m_\Sigma^2/m_i^2$ [107], which for the benchmark $m_\Sigma = 430\,\text{GeV}, m_i = 100\,\text{GeV}$ gives $\Delta a_{e,i} \sim g_i^2 \cdot 4 \cdot 10^{-14}$ and $\Delta a_{\mu,i} \sim g_i^2 \cdot 1.8 \cdot 10^{-9}$ for coupling to electrons or muons respectively. This is to be compared to the agreement between the Standard Model theoretical and experimental value up to the (absolute) precision of 10^{-12} in the case of the electron [216] and 10^{-9} in the case of the muon [14].[9] Demanding that this agreement is not spoiled

[8] This conclusion can be avoided if the reheating temperature T_{RH} is below the mass of the mediator [113].

[9] In the case of the muon, theory and experiment disagree significantly at higher precision. This $g_\mu - 2$ problem cannot be addressed in the present model, as the correction in eqn. (7.24) has the wrong sign. The

in the case of the electron or not made significantly worse in the case of the muon yields insignificant constraints on the couplings g_i if Σ couples to electrons, but can affect the parameter space when coupling to muons [107, 174].

7.3 Summary

In this chapter, we have explored effects of adding a second dark matter flavour to a simple dark matter model, the leptophilic Majorana fermion model. We have characterised the possible mechanisms that determine the relic abundance in the early Universe and identified consequences of the two-flavour scenario for dark matter indirect detection and collider searches.

For very small couplings, neither of the dark matter candidates thermalise. In the single-flavour case, one can then only hope to detect the mediator, which is unlikely to yield much information about the properties of freeze-in dark matter by itself. In the two-flavour case, as found also in chapter 6 for the case of scalar dark matter, dark matter decay can be an informative signature. The monochromatic γ-rays produced by $\psi_2 \to \psi_1\gamma$ would constitute a smoking gun signature of dark matter decay and tell about the mass scale of dark matter, which in the freeze-in case is hard to infer from processes involving the mediator alone.

Going beyond the treatment in the previous chapter, we consider general couplings $g_{1,2}$, allowing for both freeze-in and freeze-out production of dark matter. If ψ_1 is light, $m_1 \lesssim 20\,\text{eV}$, it may freeze-out while relativistic, contributing as hot dark matter or dark radiation to the energy density of the universe. This allows for much larger gamma ray signals from ψ_2 decay than in the scenario where both dark matter candidates are FIMPs, potentially resulting in detectable gamma ray fluxes down to the MeV range (see fig. 7.4). This is particularly interesting in view of future MeV gamma ray telescopes like the AMEGO [165] or e-ASTROGAM [166, 167] mission concepts.

For GeV-scale masses, ψ_i may still be produced by freeze-in if they are feebly coupled, or thermalise and subsequently freeze-out when they become non-relativistic as WIMPs. We explore the full g_1, g_2 parameter space, identifying the different regimes that lead to the relic abundance today. As necessary in the case of less-than-WIMP couplings, we do not assume chemical equilibrium between the dark sector particles, but solve their coupled Boltzmann equations numerically. As a result, we find six distinct regimes of WIMP freeze-out in the two-flavour scenario, including the canonical WIMP freeze out of $\psi_1\psi_1$ annihilations, coannihilation regimes dominated by $\psi_2\psi_2$ or $\Sigma\Sigma$ annihilations, as well as three conversion driven freeze-out regimes that deviate strongly from results that would be obtained assuming chemical equilibrium (see fig. 7.5). Much of the parameter space is ruled out by overabundance, and the regimes where only one of the two dark matter candidates thermalises are strongly constrained from constraints on dark matter decay during BBN (see fig. 7.9).

The production regimes beyond the canonical WIMP mechanism can result in striking consequences at standard WIMP searches, potentially "boosting" the present-day dark matter annihilation rate by orders of magnitude (see fig. 7.10). This indicates that even where indirect dark matter searches are not yet sensitive to the canonical WIMP annihilation cross section [171], signals are possible and in an optimistic scenario could happen any time.

In our analysis, we focused on non-degenerate dark sector masses. Coannihilation and

tension between the SM prediction and experimental determination makes a meaningful bound on $\Delta a_{\mu,i}^{\text{DM}}$ difficult to define.

conversion-driven freeze-out processes work especially well for compressed spectra. This would open up the parameter space at small couplings otherwise constrained by overabundance, while at the same time enhancing many signatures for small mediator-DM mass splitting. In addition, the $\psi_2 \to \psi_1 l^+ l^-$ decay rate is suppressed in the case of small mass splitting $m_2 - m_1 \ll m_2$. This may allow for a significant relic abundance of ψ_2 WIMPs if $\psi_2 \to \psi_1$ conversion freezes out early enough, which could have interesting signatures. Multi-flavour dark matter models with near-degenerate mass spectra promise to be an interesting direction of future work.

We focused here on the leptophilic model, which is particularly interesting in the light of dark matter indirect detection through gamma rays. However, analogous models can be constructed that couple the dark matter fermions to the quarks, via a colored mediator. These would have stronger signatures in dark matter direct detection experiments and at the LHC. A detailed exploration of the effects of multi-flavour scenarios coupled to hadrons on dark matter direct detection and collider searches is an interesting endeavour (see also [217]) and is left to future work.

Chapter 8

Thermal Production of Self-interacting Sterile Neutrinos

The simplest fermionic dark matter candidate is a Majorana fermion χ, singlet under the Standard Model gauge group. A singlet fermion fits neatly into the Standard Model of Particle Physics, acting as right-chiral partner to the SM neutrinos, the only left-chiral species that goes without right-chiral partner in the SM. This has earned them the names *right-handed neutrino* or *sterile neutrino* and can lead to a host of implications for neutrino phenomenology.

This chapter explores sterile neutrinos as *strongly interacting massive particle* (SIMP) dark matter, whose relic abundance is determined by freeze-out of number changing interactions $\chi\chi\chi\chi \to \chi\chi$. This is a novel production mechanism for sterile neutrinos, whose usual phenomenology is briefly reviewed in section 8.1.

This work can also be read in the context of a systematic exploration of SIMP models, considering for the first time a Majorana SIMP dark matter candidate. Section 8.2 first introduces general concerns in SIMP dark matter production, before calculating the relic abundance of SIMP sterile neutrino dark matter in an EFT approach. Section 8.3 replaces the effective interaction by a scalar mediator, which completes the picture of dark matter freeze-out in a decoupled dark sector that can be initially populated by freeze-in.

8.1 Sterile neutrinos

One of the simplest extensions of the Standard Model is to add a gauge-singlet fermion, χ, to its matter content. Gauge and Lorentz symmetries then allow for a Majorana mass term, as well as Yukawa couplings to the SM lepton doublet L:

$$\mathcal{L}_\chi = \frac{1}{2}\overline{\chi^c} i\partial\!\!\!/ \chi - \frac{1}{2} m_\chi \overline{\chi^c}\chi - y_\chi \overline{L}\widetilde{H}\chi + \text{h.c.}\,, \tag{8.1}$$

where $\widetilde{H} = i\tau_2 H^*$, with H the Standard Model Higgs doublet. In the literature, these Majorana singlets are often referred to as "right handed neutrinos" or "sterile neutrinos" due to the phenomenology arising from their Yukawa coupling to the active neutrinos ν in the lepton doublet $L = (\nu, e_L)$. In particular, they can explain the small observed active neutrino masses through the see-saw mechanism after electroweak symmetry breaking [218–222]. As a new neutral massive particle, the sterile neutrino can be a viable dark matter candidate. Reviews of sterile neutrinos as dark matter can be found at [223–225].

Its coupling to active neutrinos allows for the decay $\chi \to \nu\bar{\nu}\nu$, and requiring that the lifetime of dark matter sterile neutrinos exceeds the age of the universe puts a constraint on the model parameters (m_χ, y_χ) [223]:

$$y_\chi \lesssim 3 \cdot 10^{-17} \left(\frac{m_\chi}{\text{GeV}}\right)^{-3/2} \quad \text{(cosmological stability)} \tag{8.2}$$

This in turn constrains the dark matter production mechanism: If the sterile neutrino was in thermal equilibrium with the Standard Model bath in the early universe, the relic abundance left over after freeze-out of annihilations (i.e. in the WIMP mechanism) would be too large. Instead, in frameworks of sterile neutrino dark matter it is usually assumed that the initial abundance of sterile neutrinos at some very high temperature $T \gg m_\chi$ was negligible. This can result e.g. if reheating after inflation only produces Standard Model particles and their coupling to sterile neutrinos is small. The out-of-equilibrium production of sterile neutrinos in the early universe is then a special case of the FIMP mechanism, the Dodelson&Widrow (DW) mechanism [57]. If there is a large lepton asymmetry present while sterile neutrinos are being produced, the yield can be increased, as explored by Shi&Fuller (SF) [226].

The most stringent constraints on sterile neutrino dark matter produced through their Yukawa coupling to SM leptons come from X-ray telescopes: Instead of decaying to three active neutrinos, sterile neutrinos can also decay radiatively via an electron-W-boson loop into an active neutrino and a photon. Limits on the decay rate from X-ray observations exclude DW-production as the only production mechanism and require new physics beyond the DM sterile neutrino to create the large lepton asymmetry necessary to make SF-production viable [227]. On the other hand, there is a persistent hint for a signal in X-ray data at 3.5 keV that could be explained by sterile neutrino dark matter decay (e.g. [224, 228, 229], see however [230–232]). In addition to X-ray constraints putting upper limits on the coupling to SM leptons, structure formation constraints from Lyman-α forest observations and Milky-Way satellite counts put lower limits on the sterile neutrino mass [62, 233] (see section 4.1).

Taken together, the remaining parameter space for sterile neutrino dark matter is already tightly constrained. On top of that, while the minimal model in eq. (8.1) can potentially accommodate active neutrino masses, baryogenesis through leptogenesis and sterile neutrino dark matter, the combinations of parameters (m_χ, y_χ) that give rise to the correct dark matter relic abundance through the DW or SF mechanisms do not simultaneously explain anything but dark matter. This has motivated studies beyond the minimal model of eq. (8.1), introducing e.g. an additional production channel through the decay of a scalar singlet [234–237] or thermalising the sterile neutrinos by coupling them to a self-interacting scalar [238]. The work presented in this chapter follows the same rationale and investigates the possibility of sterile neutrino self-interactions as the dark matter production mechanism.

8.2 Majorana SIMPs

Motivated by the preceding discussion, we examine the dark matter phenomenology of the Majorana singlet χ independently from its possible couplings to the Standard Model. The part of the Lagrangian involving only the sterile neutrino field, including operators up to dimension six, reads:[1]

$$\mathcal{L}_{\text{DM}} = \frac{1}{2}\overline{\chi^c} i\partial\!\!\!/ \chi - \frac{1}{2} m_\chi \overline{\chi^c}\chi + \frac{1}{4!\Lambda^2}(\overline{\chi^c}\chi)(\overline{\chi^c}\chi) + \text{h.c.}\,. \tag{8.3}$$

[1] Note that different Lorentz structures for the spinor bilinears of the dim-6 operator are possible. We investigate only the scalar interaction for simplicity.

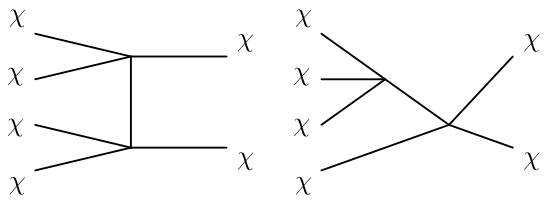

Figure 8.1: Topologies for the 4-to-2 annihilation process $\chi\chi\chi\chi \to \chi\chi$ in the effective theory of dark matter self-interactions.

In the following, we will assume that all portal interactions between this dark sector and the visible sector (i.e. at dimension 4: the Yukawa coupling $y_\chi \overline{L}\widetilde{H}\chi$) have negligible strength. This ensures that they play no role in determining the χ relic abundance and that χ is cosmologically long-lived.

The dimension-6 self-interaction leads to dark matter 2-to-2 scattering with cross section

$$\sigma_{2\to2} = \frac{1}{72\pi}\frac{m_\chi^2}{\Lambda^4}\,. \tag{8.4}$$

This self-scattering process has been invoked in the literature to alleviate small scale problems of the ΛCDM paradigm (see section 4.2) while on the other hand being constrained by observations of merging galaxy clusters to be $\sigma_{2\to2}/m_\chi \lesssim 1\,\mathrm{cm}^2/\mathrm{g}$ [84]. 2-to-2 interactions do not change the dark matter number density , but the self-interaction also gives rise to number-changing processes: For fermionic dark matter, $3 \to 2$ processes are forbidden by angular momentum conservation, but the $4 \to 2$ process $\chi\chi\chi\chi \to \chi\chi$ induced by the diagrams shown in fig. 8.1 is allowed and can deplete the dark matter abundance in the early Universe to the small value observed today (eqn. 5.23).

Depletion of the dark matter abundance by number-changing interactions among itself was first considered by [8] and subsequent discussion in the literature focused primarily on consequences for structure formation (e.g. [239]). The topic has received a boost in attention in the context of the search for scenarios of dark matter production beyond the WIMP paradigm, inspiring the acronym "SIMP" for strongly-interacting-massive-particle [240]. Since then, SIMP dark matter models have been systematically explored in the literature for pseudoscalar [9,241], scalar [242–248], spin 1/2 Dirac fermion [246–248], spin 1 vector boson [248–250] or spin 2 boson [251] dark matter candidates. The present work also falls into this line of investigation, considering for the first time spin 1/2 Majorana fermions as SIMP dark matter [10].

The SIMP heat problem While all references above share the feature that the dark matter abundance is depleted by $3 \to 2$ or $4 \to 2$ annihilations of the dark matter candidate, one can distinguish between two ways in which they solve a problem of the original model [8]. As will be discussed shortly (sec. 8.2.1.2), number-changing interactions in a decoupled dark sector are not very effective at depleting the dark matter number density, since they heat the dark matter relative to the SM bath, leading to a slower drop in their abundance than if they would follow the SM bath temperature. This can lead to requiring excessively large self-interaction in violation of present day bounds [239].

The innovation in [240] is to couple the dark and visible sectors through a portal, so that the excess heat produced in the DM number changing interactions is dumped to the SM bath and the DM abundance drops quickly, requiring only moderate self-interaction

strength to keep number changing interactions active to the time when the DM abundance is sufficiently depleted. This coupling between DM and the visible sector leads to interesting signatures in this type of models. Possible portals through which to realise this mechanism have been explored extensively, see e.g. [9,241–244,252,253]. Dumping the heat produced in self-annihilations to the SM bath does however not work for models relying on $4 \to 2$ annihilations, since they require smaller masses in this scenario than $3 \to 2$ annihilations, leading to energy injection into the SM bath at late times, violating BBN and CMB bounds [240].

The other way to avoid large final dark matter temperatures is to start out colder [245], which has been used e.g. in [246–251,254]. If interactions between the dark and visible sectors are rare, the dark sector temperature T' may differ from the visible sector temperature T. If initially $T' < T$, the dark matter abundance is already suppressed before it is depleted by number changing interactions when dark matter becomes non-relativistic. Smaller self-interaction strengths are hence required to achieve the observed relic density, at the cost of introducing a dependence of the dark matter relic density on the cosmological history at large temperatures $T \gtrsim m_{\mathrm{DM}}$.

In the case of Majorana SIMPs, we need to make use of this second solution to the self-heating problem, as $4 \to 2$ interactions are the dominant number changing process. We determine the relic abundance in the effective interaction approach of eq. (8.3), taking the relation between dark and visible sector temperatures T'/T as free parameter in the following section 8.2.1, before discussing a possible UV-completion of the model that offers a complete picture of the cosmological history in section 8.3.

8.2.1 Relic abundance calculation

The phase space density of Majorana SIMPs is governed by the general Boltzmann equations (5.24) introduced in section 5.2. To simplify these, we assume in the following that at early times, the interaction between dark matter particles is sufficiently large to allow them to attain chemical equilibrium with themselves, so that their phase space distribution can be characterised by a temperature T'. Since we assume negligible interaction with the SM bath, the dark sector temperature T' may be different from the temperature T of the SM bath. We further assume Maxwell-Boltzmann statistics, restricting our analysis to non-relativistic freeze-out.[2] Under these assumptions, the evolution of the dark sector is determined by the following coupled system of Boltzmann equations for the dark sector number density and energy density:[3]

$$\frac{dn_\chi}{dt} + 3Hn_\chi = -\langle \sigma v^3 \rangle \left(n_\chi^4 - n_\chi^2 n_\chi^{\mathrm{eq}\,2} \right), \tag{8.5}$$

$$\frac{d\rho_\chi}{dt} + CH\rho_\chi = 0\,. \tag{8.6}$$

Here, H is the Hubble parameter, $\langle \sigma v^3 \rangle$ is the thermally averaged cross section for the 4-to-2 process, n_χ^{eq} is the dark matter number density in equilibrium and C accounts for the transition from the ultra-relativistic ($C = 4$) to the non-relativistic ($C = 3$) regime. Going through these one by one, the Hubble parameter is given by (see also section 5.1):

$$H^2 = \frac{8\pi}{3} G_N \Big(\rho(T) + \rho'(T') \Big)\,, \tag{8.7}$$

[2] For a starting point on extending the calculation to relativistic freeze-out, see [128] who consider real scalar dark matter depleted through $4 \to 2$ interactions.

[3] The equation for the evolution of $\rho(t)$ is obtained from the first moment of the Boltzmann equation (5.24).

where G_N is the gravitational constant, and $\rho(T)$ and $\rho'(T')$ are the energy densities in the visible and dark sectors, respectively:

$$\rho(T) = g_{\text{eff}}(T)\frac{\pi^2}{30}T^4 \,, \qquad \rho'(T') = g'_{\text{eff}}(T')\frac{\pi^2}{30}T'^4 \,, \tag{8.8}$$

with $g_{\text{eff}}(T)$ and $g'_{\text{eff}}(T')$ the effective number of degrees of freedom in the corresponding sector (see section 5.1, eqn. (5.14)). In the present study, we neglect the contribution of ρ' to the total energy density, since $T' \ll T$ in the relevant part of parameter space. In contrast, the dark matter equilibrium number density n_χ^{eq} depends only on the dark sector temperature T' (cf. eqn. 5.11):

$$n_\chi^{\text{eq}} = \frac{m_\chi^2 T'}{\pi^2} K_2\left(\frac{m_\chi}{T'}\right) \,, \tag{8.9}$$

where $K_n(x)$ is the modified Bessel function of the second kind of order n. The thermally averaged cross section is defined in eqn. (5.32) and for the $4 \to 2$ process can be obtained in the non-relativistic limit using [255]

$$\langle\sigma v^3\rangle \equiv \frac{\int d^3v_1\, d^3v_2\, d^3v_3\, d^3v_4\, \left(\sigma v^3\right) \delta^3(\vec{v}_1+\vec{v}_2+\vec{v}_3+\vec{v}_4) e^{-\frac{m_\chi}{2T'}\left(v_1^2+v_2^2+v_3^2+v_4^2\right)}}{\int d^3v_1\, d^3v_2\, d^3v_3\, d^3v_4\, \delta^3(\vec{v}_1+\vec{v}_2+\vec{v}_3+\vec{v}_4) e^{-\frac{m_\chi}{2T'}\left(v_1^2+v_2^2+v_3^2+v_4^2\right)}} \,, \tag{8.10}$$

with $\vec{v}_i$ the velocities of the initial state particles. The $4 \to 2$ annihilation cross section can be obtained from the invariant amplitude $\mathcal{M}$ from

$$\left(\sigma v^3\right) = \frac{\sqrt{3}}{6144\pi m_\chi^4} \int \frac{d\Omega}{4\pi} \overline{|\mathcal{M}|^2} \,, \tag{8.11}$$

where $d\Omega$ is the solid angle of any of the final state particles. We have calculated the invariant amplitude from the Feynman diagrams depicted in Fig. 8.1, using FeynCalc [256,257].[4] The resulting expression is not illuminating and hence not shown here, but physical insight can be gained by expanding in velocities $\vec{v}_i$ $(i = 1,2,3,4)$, where one finds that the leading terms are proportional to fourth-order invariants of the velocities (*e.g.* v_i^4, $v_i^2 v_j^2$, $(\vec{v}_i \cdot \vec{v}_j)^2$), i.e. the cross-section is d-wave suppressed. This behavior is expected for an initial state of four identical Majorana fermions from the Pauli exclusion principle: Each initial fermion is specified by its spin $s_i = \pm 1/2$ and orbital angular momentum $\ell_i = 0, 1, \ldots$. In a partial wave expansion, the state where all particles have $\ell_i = 0$ is incompatible with the Pauli exclusion principle, since this would require two of the fermions to also have the same spin quantum number. The lowest order term in the partial wave expansion must hence contain two fermions with $\ell = 0$ and two fermions with $\ell = 1$, resulting in an overall d-wave suppression of the cross section. This d-wave suppression could be lifted if the fermions had an additional internal quantum number (e.g. family number) or higher spin, and the argument can be generalised to other number changing processes involving self-interactions of Dirac or Majorana fermions. Finally, the result for the thermally averaged annihilation cross section reads:

$$\langle\sigma v^3\rangle = \frac{1201}{245760\sqrt{3}\pi\Lambda^8}\frac{T'^2}{m_\chi^2} \,. \tag{8.12}$$

[4] The calculation of the invariant amplitude and thermally averaged cross section was performed by Takashi Toma.

Looking at the terms that appear in the Boltzmann equation (8.5) for $n_\chi(t)$ above, it becomes clear that they depend on both the SM temperature T ($s(T)$ and $H(T)$) and the dark sector temperature T' ($n_\chi^{\mathrm{eq}}(T')$ and $\langle\sigma v^3\rangle(T')$). The full evolution of the dark sector temperature can be obtained from solving eqns. (8.5) and (8.6) together, which is done numerically in section 8.2.1.2. However, if one is only interested in the final relic abundance, further simplifying assumptions can be made to obtain a reasonably accurate analytical result, which is done in the following.

8.2.1.1 Instantaneous freeze-out approximation

The instantaneous freeze-out approximation assumes that the dark matter abundance $Y_\chi = n_\chi/s$ follows its equilibrium value until freeze-out of number-changing interactions and remains constant afterwards,

$$Y_\chi|_{\mathrm{today}} \simeq Y_\chi|_{\mathrm{FO}} \simeq Y_\chi^{\mathrm{eq}}\big|_{\mathrm{FO}} \,. \tag{8.13}$$

Freeze-out is determined by the time t_{fo} (or equivalently photon temperature T_{fo}, see sec. 5.2) when the annihilation rate per particle drops below the expansion rate

$$\Gamma_{4\to2}(T'_{\mathrm{fo}}) = H(T_{\mathrm{fo}}) \,, \tag{8.14}$$

where T'_{fo} is the dark sector temperature at time t_{fo}. The annihilation rate per particle is given by

$$\Gamma_{4\to2}(T'_{\mathrm{fo}}) = \langle\sigma v^3\rangle(T'_{\mathrm{fo}})\, n_\chi^3(T'_{\mathrm{fo}}) \simeq \langle\sigma v^3\rangle\Big|_{T'=m_\chi} \left(\frac{T'_{\mathrm{fo}}}{m_\chi}\right)^2 n_\chi^{\mathrm{eq}\,3}(T'_{\mathrm{fo}}) \,, \tag{8.15}$$

using that the d-wave suppressed thermally averaged cross section is proportional to T'^2. Given the particle physics input of $(m_\chi, \langle\sigma v^3\rangle)$ and taking the ratio between visible and dark sector temperatures $T_{\mathrm{fo}}/T'_{\mathrm{fo}}$ at freeze-out as a further input parameter, these relations determine the resulting relic abundance today, $Y_{\chi,0}$.

Comparing to the observed dark matter density (eqn. (2.11)), we can obtain constraints on the model parameters. The dark matter density today is related to the dark matter abundance by

$$\Omega_\chi = \frac{m_\chi s_0}{\rho_c} Y_{\chi,0} \,, \tag{8.16}$$

where $s_0 = 2890\,\mathrm{cm}^{-3}$ and $\rho_c = 10.54h^2\,\mathrm{GeV/m}^3$ are the present time visible sector entropy density and critical density. $Y_{\chi,0}$ is the present dark matter abundance, which in the instantaneous freeze-out approximation is equal to the equilibrium dark matter abundance at freeze-out:

$$Y_{\chi,0} \simeq Y_\chi^{\mathrm{eq}}(T_{\mathrm{fo}}) = \frac{n_\chi^{\mathrm{eq}}(T'_{\mathrm{fo}})}{s(T_{\mathrm{fo}})} \,, \tag{8.17}$$

using the standard relations for entropy density (eqn. 5.18) and equilibrium number density (eqn. 5.8).

From eqns. (8.13, 8.16), requiring that the dark matter density reproduce the value measured by Planck, $\Omega_{\mathrm{DM}}h^2 \simeq 0.12$ [18], gives a condition on the the dark sector freeze-out temperature:

$$\left(\frac{T'_{\mathrm{fo}}}{m_\chi}\right)^{-1} \approx 7.7 + \log\left[\left(\frac{m_\chi}{30\,\mathrm{MeV}}\right)\left(\frac{T_{\mathrm{fo}}/T'_{\mathrm{fo}}}{10}\right)^{-3}\left(\frac{T'_{\mathrm{fo}}}{m_\chi}\right)^{-3/2}\left(\frac{10}{h_{\mathrm{eff}}(T_{\mathrm{fo}})}\right)\right] \,. \tag{8.18}$$

This depends on the dark matter mass and on the ratio between the temperatures of the visible and dark sectors at freeze-out. The freeze-out condition (8.13) then determines the corresponding value of the thermally averaged annihilation cross section $\langle\sigma v^3\rangle_0 \equiv \langle\sigma v^3\rangle\Big|_{T'=m_\chi}$:

$$\langle\sigma v^3\rangle_0 = 6.3\times10^9\,\mathrm{GeV}^8\left(\frac{\mathrm{GeV}}{m_\chi}\right)^4\left(\frac{T'_{\mathrm{fo}}}{m_\chi/10}\right)^{-9}\left(\frac{T_{\mathrm{fo}}/T'_{\mathrm{fo}}}{10}\right)^{-7}\sqrt{\frac{g_{\mathrm{eff}}(T_{\mathrm{fo}})}{10}}\left(\frac{h_{\mathrm{eff}}(T_{\mathrm{fo}})}{10}\right)^{-3}. \tag{8.19}$$

Finally, substituting eqn. (8.12) into eqn. (8.19), the value of the suppression scale of the dimension six operator resulting in the observed dark matter relic density is obtained as:

$$\Lambda \approx 25\,\mathrm{MeV}\left(\frac{m_\chi}{\mathrm{GeV}}\right)^{1/2}\left(\frac{T_{\mathrm{fo}}/T'_{\mathrm{fo}}}{10}\right)^{7/8}\left(\frac{T'_{\mathrm{fo}}}{m_\chi/10}\right)^{9/8}\left(\frac{g_{\mathrm{eff}}(T_{\mathrm{fo}})}{10}\right)^{-1/16}\left(\frac{h_{\mathrm{eff}}(T_{\mathrm{fo}})}{10}\right)^{3/8}. \tag{8.20}$$

The value of the suppression scale leading to the measured dark matter abundance is shown in Fig. 8.3 for different values of the ratio of the freeze-out temperatures $T_{\mathrm{fo}}/T'_{\mathrm{fo}} = 10, 25, 50, 200$, along with constraints on the parameter space, which are discussed in section 8.2.2 in detail.

Note on the accuracy of the instantaneous freeze-out approximation Before starting the numerical treatment in the following section, we briefly look how the instantaneous freeze-out approximation for $4 \to 2$ annihilating SIMP dark matter arises from the full Boltzmann equation (8.5). Approximating $Y_\chi^{\mathrm{eq}} = 0$ after freeze-out (motivated by the fact that it drops exponentially), one can write for the late-time evolution of Y_χ:

$$\frac{dY_\chi}{dx} \simeq -\frac{s^3}{Hx}\langle\sigma v^3\rangle Y_\chi^4, \tag{8.21}$$

where we have switched to the formulation in terms of (Y_χ, x) instead of (n_χ, t), as described in section 5.2 (cf. eqn. (5.36), neglecting changes in h_{eff}). This can be integrated from freeze-out to the present to give

$$Y_{\chi,\infty} = \left(\frac{1}{Y_\chi(x_f)^3} + 3\int_{x_f}^{\infty} dx\,\frac{s^3}{Hx}\langle\sigma v^3\rangle\right)^{-1/3} \tag{8.22}$$

The first term of this equation corresponds to the abundance of χ at freeze-out, and in the instantaneous freeze-out approximation is taken as $Y_\chi(x_f) = Y_\chi^{\mathrm{eq}}(x_f)$. The second term accounts for depletion due to residual annihilations after freeze out.

There are two sources of error in this approximation. First, at the time when the freeze-out condition eqn. (8.14) is fulfilled, the χ abundance Y_χ already deviates slightly from its equilibrium value Y_χ^{eq}. Second, residual annihilations after the freeze-out time are neglected. They are relevant for the case of WIMP DM, to the extent that the $Y_\chi(x_f)$ term in eq. (8.22) has sometimes been neglected entirely in the literature [1]. For freeze-out of $4 \to 2$ annihilations however, the annihilation term in eq. (8.22) is subdominant, as the integrand $\frac{s^3}{Hx}\langle\sigma v^3\rangle \simeq \frac{s(m)^3}{H(m)}\langle\sigma v^3\rangle_0 x'^{-2}x^{-8}$ decreases very sharply with x (compared to $\frac{s}{Hx}\langle\sigma v\rangle \sim \frac{s(m)}{H(m)}\langle\sigma v\rangle_0 x^{-2}$ for s-wave $2 \to 2$-annihilating WIMPs).

We have confirmed the goodness of the approximation by solving the coupled Boltzmann equations (8.5), (8.6) numerically for some selected values of the parameters as described in the following section. The result differs by at most 10% from the one obtained with the instantaneous freeze-out approximation.

8.2.1.2 Numerical solution of the Boltzmann equation

The coupled Boltzmann equations (8.5), (8.6) can be solved numerically to get a full picture of the dark sector evolution and to check the accuracy of the instantaneous freeze-out approximation used above. First, the standard procedure described in section 5.2 is used to cast the Boltzmann equation in terms of $x = m_\chi/T$ as the time parameter:

$$\frac{dY_\chi}{dx} = \frac{s^3\langle\sigma v^3\rangle_{4\to2}}{xH/\tilde{g}} Y_\chi^4 \left(1 - \frac{Y_\chi^{\mathrm{eq}\,2}}{Y_\chi^2}\right) \tag{8.23}$$

$$\frac{d\rho_\chi}{dx} = -\frac{1}{x} C(x')\tilde{g}\rho_\chi \tag{8.24}$$

where we now need the explicit form of the dilution factor C that interpolates between the regime where ρ_χ redshifts as radiation and the regime where it redshifts as non-relativistic matter [1, 238]:

$$C\,(x) = \frac{1}{\rho}(3\rho + 3\mathcal{P}) = 3\left(1 + \frac{1}{x}\frac{K_2(x)}{K_1(x) + 3K_2(x)/x}\right), \tag{8.25}$$

where $K_{1,2}$ are modified Bessel functions of the second kind of 1st and 2nd order. $\tilde{g}$ accounts for the variation of $h_{\mathrm{eff}}(T)$ with time, which affects the $t \leftrightarrow x_{\mathrm{DM}}$ relation (see section 5.2):

$$\tilde{g} = 1 + \frac{1}{3}\frac{T}{h_{\mathrm{eff}}}\frac{dh_{\mathrm{eff}}}{dT}. \tag{8.26}$$

The equations for n_χ and ρ_χ are coupled via the dark sector temperature T' (or equivalently x') that enters $Y_\chi^{\mathrm{eq}}(T')$ and $C(T')$. It is related to the average energy per particle of mass m by

$$\frac{\rho}{n} = m\left(\frac{K_1(x')}{K_2(x')} + \frac{3}{x'}\right). \tag{8.27}$$

This relation can be numerically inverted to give $x'\,(\rho/nm)$. We now have all the necessary ingredients to numerically trace the evolution of Y_χ and T' in the early universe.

We have numerically solved eqns. (8.23), (8.24) for a range of m_χ and $\langle\sigma v^3\rangle_0$ for different initial temperature ratios T/T'. Figure 8.2 shows an example for the abundance and temperature evolution. For a given mass and coupling benchmark, starting from a cosmological initial condition specified by the temperature ratio T/T' while the dark matter is still relativistic, this illustrates the temperature and abundance evolution in three phases:

1. When $T' > m_\chi$, the dark matter is relativistic. Its temperature drops like that of the SM bath (approximately, up to changes in h_{eff}).

2. When T' drops below m_χ, Y_χ^{eq} starts to drop and $4 \to 2$ annihilations come to dominate over $2 \to 4$ processes. This release of energy delays the cooling of the dark sector, and T' decreases more slowly than T. As a consequence, Y_χ^{eq} drops only slowly, delaying the depletion of the dark matter abundance.

3. Finally, $4 \to 2$ processes become insufficient to keep Y_χ close to Y_χ^{eq} at freeze-out, and Y_χ approaches its final constant value. The temperature of the dark matter particles now goes as $T' \propto v^2 \propto T^2$, as appropriate for a decoupled, nonrelativistic species.

To compare to the analytical results derived in terms of $T'/T|_{\mathrm{fo}}$, we define x_f and the temperature ratio at freeze-out T/T' by $Y_\chi(x_f) = 1.1 \times Y_{\chi,\mathrm{eq}}(x'_f)$. We find that the resulting relic abundances agree within 10% with the corresponding analytical result.

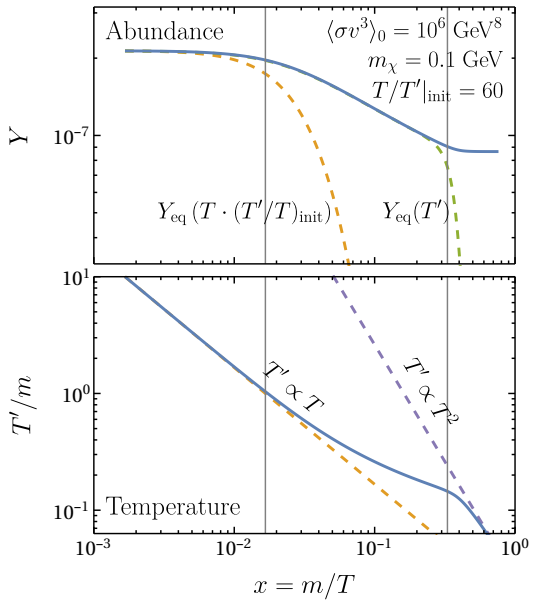

Figure 8.2: Characteristic abundance and temperature evolution. Blue lines show the solution of Y_χ and T' determined from eqns. (8.23), (8.24), and (8.27). For comparison, the upper panel also shows the evolution of the equilibrium abundance $Y_\chi^{\rm eq}$ (green), as well as the equilibrium evolution that would result if the dark sector would not heat up (orange), illustrating the delayed dark matter depletion in the self-annihilation scenario. The bottom panel shows the dark sector temperature evolution as discussed in the text. The two vertical gray lines mark the time when dark matter becomes non-relativistic $T' = m_\chi$ and the time when it freezes out $T = T_{\rm fo}$.

8.2.2 Results and constraints

Contours of model parameters (m_χ, Λ) that result in the correct relic abundance for given cosmological initial conditions (specified by the temperature ratio $T/T'|_{\rm fo}$ at freeze-out) are shown in Figure 8.3. We choose $T/T'|_{\rm fo}$ as the cosmological free parameter, which makes the analytical result (8.20) particularly simple.[5]

In our analysis we conservatively disregard the region of the parameter space where $T'_{\rm fo} > m_\chi/3$. There, χ would not be non-relativistic during freeze-out, invalidating the Maxwell-Boltzmann approximation used in obtaining the integrated Boltzmann equation (8.5) as well as the thermally averaged cross-section (8.10).[6] This gives an m_χ-dependent upper limit for the suppression scale Λ we can consider, shown as an orange region in Figure 8.3.

The requirement of EFT-validity puts a lower limit to the suppression scale Λ: At energy scales larger than Λ, one expects both significant contributions from higher dimensional operators (in addition to the dimension-6 operator we consider here, eqn. (8.3)), as well as contributions from whatever high-scale physics UV-completes the model. This is not a very sharp criterion. As the energy scale of non-relativistic dark matter annihilation is $\sim m_\chi$, we take $\Lambda \sim m_\chi$ as an indicative lower bound to the range of sensible values, shown as a gray

[5] As Figure 8.2 shows, the temperature ratio T/T' is not constant, such that $T/T'|_{\rm fo}$ depends both on the cosmological initial conditions as well as on the particle physics parameters of the model. Separating these is left to section 8.3, where we introduce a UV completion to the particle physics model that can also give a complete picture of the cosmological history in the present setup.

[6] The equivalent calculation including relativistic freeze-out for a $4 \to 2$-annihilating real scalar dark matter candidate has recently been done by [128].

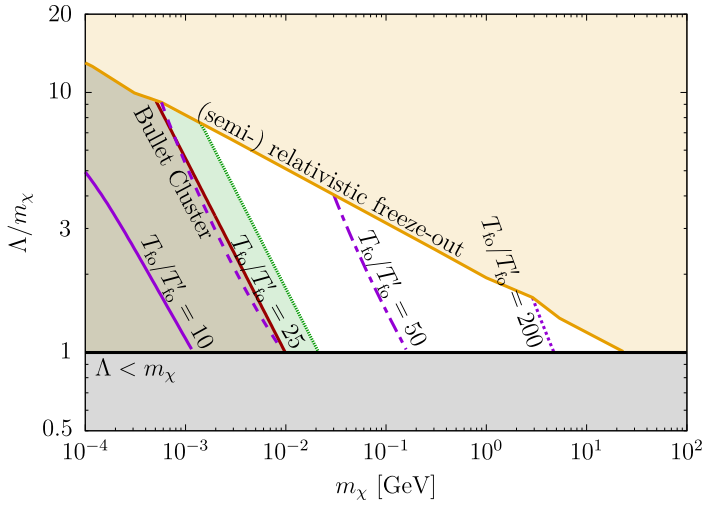

Figure 8.3: Model parameters leading to the observed relic density for fixed values of the temperature ratio between the dark sector and the visible sector at freeze-out. The parameter space calculable in our non-relativistic treatment is bounded by the orange line. The region below the black line cannot be analyzed with our set-up, as the effective theory description is not valid. The brown region is excluded by limits on the $2 \to 2$ scattering cross section, and the green region can potentially alleviate the small scale problems of the cold dark matter paradigm.

region in Figure 8.3.

As the model discussed so far may be completely decoupled from the visible sector, there are no dark matter direct detection or indirect detection constraints. However, dark matter self annihilations imply large self-interaction cross sections, eqn. (8.4), which is constrained by observations of colliding galaxy clusters to be $\sigma_{2\to2}/m_\chi \lesssim 1\,\mathrm{cm}^2/\mathrm{g}$ [84]. This constraint translates into the lower limit $\Lambda \gtrsim 6\left(\frac{m_\chi}{\mathrm{MeV}}\right)^{1/4}$ MeV, shown in brown in figure 8.3. The self-interaction could provide a solution to the small scale structure problems (see Section 4.2) if $\sigma_{2\to2}/m_\chi \gtrsim 0.1\,\mathrm{cm}^2/\mathrm{g}$ [66]; this region of parameter space is shown in green in the figure.

The observed dark matter abundance can be reproduced in this framework and is compatible with all constraints for dark matter masses in the range $500\,\mathrm{keV} \lesssim m_\chi \lesssim 20\,\mathrm{GeV}$ for visible-to-hidden sector temperature ratio at freeze-out $25 \lesssim T_{\rm fo}/T'_{\rm fo} \lesssim 400$. The scale Λ of the dimension-6 operator takes values between m_χ and $10\,m_\chi$ to reproduce the correct abundance.

Before these results are discussed in detail in section 8.4, we want to highlight two issues of the present model that are addressed in the following. First, the required values of Λ are close to m_χ, and it is an important question whether such strong couplings can be accommodated in a reasonable UV-completion of the model. Second, we have so far contended ourselves with parameterising the relative amounts of dark sector and visible sector thermal bath contents by the temperature ratio T/T' at freeze out, without discussing its origin and significance. In the next section, we address both issues by considering a UV-complete model for the sterile neutrino self-interaction.

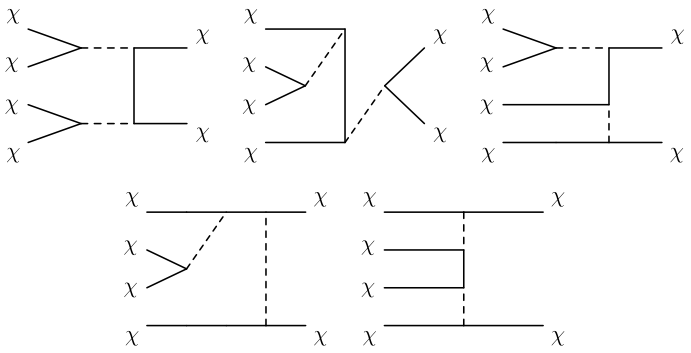

Figure 8.4: Topologies for the 4-to-2 annihilation process $\chi\chi\chi\chi \to \chi\chi$ in the toy model for dark matter self-interactions through scalar singlet exchange.

8.3 A toy model of dark matter self-interactions

In this section, we consider a UV-complete toy model that features strong sterile neutrino self-interactions. In addition to the sterile neutrino χ, we add a scalar singlet φ with $m_\varphi > m_\chi$. It interacts with the sterile neutrino by a Yukawa coupling of the form

$$\mathcal{L}_{\text{int}} = -\frac{y_\varphi}{2}\varphi\overline{\chi^c}\chi. \tag{8.28}$$

At energy scales $\mu \ll m_\varphi$, the scalar can be integrated out and one recovers the effective interaction in eqn. (8.3) with $\Lambda = \frac{m_\varphi}{\sqrt{3}y_\varphi}$. In the following, we first use the analytical results for the relic abundance derived in the previous section and apply them to the toy model (section 8.3.1), before obtaining a complete picture of the thermal evolution of the dark sector (section 8.3.2).

8.3.1 SIMP results in the toy model

The self-annihilation process $\chi\chi\chi\chi \to \chi\chi$ is induced by the diagrams in Fig. 8.4. The thermally averaged cross-section can be calculated from eqns. (8.10), (8.11) and away from resonances ($2m_\chi \not\approx m_\varphi$ and $4m_\chi \not\approx m_\varphi$) reads

$$\langle\sigma v^3\rangle = \frac{27\sqrt{3}y_\varphi^8 \sum_{n=0}^{8} a_n \xi^n}{245760\pi m_\chi^8 (16-\xi)^2(4-\xi)^4(2+\xi)^6 x'^2}, \tag{8.29}$$

where $\xi \equiv m_\varphi^2/m_\chi^2 > 4$, and the coefficients a_n are given by

$$\begin{aligned} a_0 &= 2467430400, & a_1 &= -1648072704, \\ a_2 &= 491804416, & a_3 &= -25463616, \\ a_4 &= 4824144, & a_5 &= -1528916, \\ a_6 &= 473664, & a_7 &= -35259, \\ a_8 &= 1201. \end{aligned}$$

This can be applied to relate the relic abundance result on the thermally averaged cross

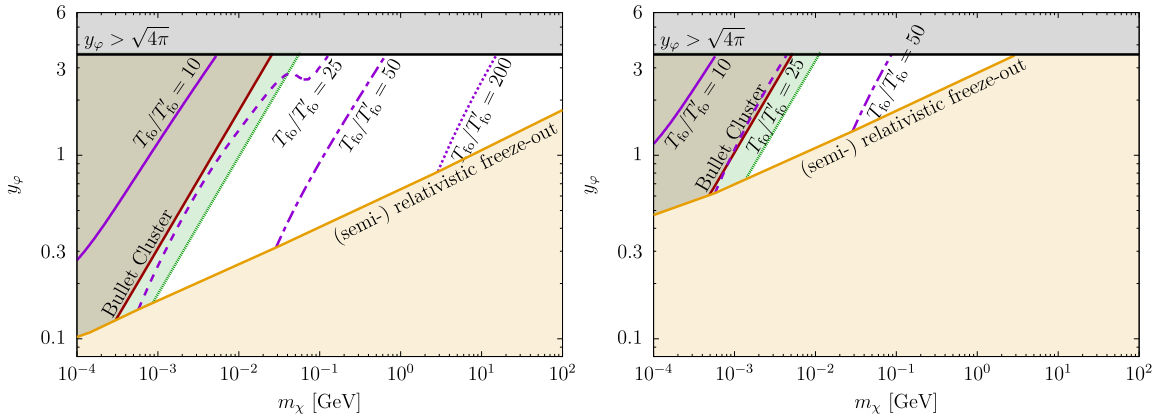

Figure 8.5: Contours of the ratio of visible sector to dark sector temperatures at freeze-out leading to the observed dark matter density for given values of mass m_χ and coupling y_φ in the toy model where the dark matter self-interaction is mediated by singlet scalar φ with mass $m_\varphi = 3m_\chi$ (left panel) or $10m_\chi$ (right panel). The parameter space calculable in our approach is limited by non-perturbativity (gray region) and non-relativistic freeze-out (orange). Self-interaction constraints are shown in brown. In the green region, the self-interaction can have interesting astrophysical consequences (see text).

section from eqn. (8.19) to the toy model parameters m_χ, y_φ that yield the correct relic abundance for a given scalar mass m_φ and cosmological initial conditions specified by $T/T'|_{\rm fo}$, using eqns. (8.29) and (8.19). The results are shown in Fig. 8.5, taking $m_\varphi/m_\chi = 3$ (left panel) and 10 (right panel). As in Figure 8.3, the regions of parameter space where our calculation cannot be applied are indicated as gray and orange regions. Our perturbative calculation requires $y_\varphi < \sqrt{4\pi}$ to be valid, and non-relativistic freeze-out requires $T'_{\rm fo} < m_\chi/3$. The self-scattering constraint $\sigma_{2\to2}/m_\chi \lesssim 1\,{\rm cm}^2/{\rm g}$ [84] translates into the upper limit on the Yukawa coupling $y_\varphi \lesssim 0.1\left(\frac{m_\chi}{\rm MeV}\right)^{3/4}\left(\frac{m_\varphi}{m_\chi}\right)$, shown in brown.

We find that the sterile neutrino abundance determined by its self-interactions mediated by the scalar φ can match the observed relic density if the sterile neutrino mass is in the range $300\,{\rm keV} \lesssim m_\chi \lesssim 3\,{\rm TeV}$ ($500\,{\rm keV} \lesssim m_\chi \lesssim 3\,{\rm GeV}$), the Yukawa coupling is $y_\varphi \gtrsim 0.12$ (0.6) and the visible-to-hidden sector temperature ratio at freeze-out is $20\,(24) \lesssim T_{\rm fo}/T'_{\rm fo} \lesssim 2000\,(200)$ for $m_\varphi/m_\chi = 3$ (10). As in the effective operator description, there are points in the parameter space where the small scale problems of cold dark matter can be addressed by self-interactions with strength compatible with the SIMP mechanism. Comparing the two panels, we see that the parameter space compatible with all constraints shrinks for larger m_φ (i.e. smaller overall annihilation cross sections) and allows for a smaller range of of values for $T_{\rm fo}/T'_{\rm fo}$. In order to have a sufficiently large annihilation cross section, an increase in m_φ/m_χ must be compensated by an increase in y_φ, which for very large m_φ eventually conflicts with the perturbativity requirement $y_\varphi < \sqrt{4\pi}$. This sets an upper limit on the singlet scalar mass $m_\varphi \lesssim 55\, m_\chi$.

The preceding discussion shows that the large couplings necessary for sufficient dark matter depletion through $4 \to 2$ interactions can be accommodated in a simple toy-model. In the following, we address how the introduced scalar singlet can explain the origin of the cool dark sector with $T/T' > 1$.

8.3.2 Thermal dark sector from freeze-in

The presence of the scalar singlet in the model opens new portals between the dark sector and the Standard Model bath. The scalar potential includes coupling terms to the Standard Model Higgs H:

$$-\mathcal{L}_{\text{scalar portal}} = \mu_{\varphi H}\,\varphi|H|^2 + \frac{1}{2}\lambda_{\varphi H}\,\varphi^2|H|^2. \tag{8.30}$$

These interactions must be weak enough to not equilibrate the two sectors, as we found that $T' < T$ is required to reproduce the correct relic abundance. They can however offer a mechanism for the origin of the dark sector population through rare Higgs-decays in the spirit of the FIMP mechanism discussed in section 5.4 [245]: After electroweak symmetry breaking, the model contains a real scalar h, which is mostly composed of the Standard Model Higgs boson and has a small scalar singlet φ contribution, which we parameterise by the mixing angle $\sin\theta$. In the early Universe, at temperatures comparable to the Higgs mass, the Higgs boson is in thermal equilibrium with the rest of the Standard Model bath and can populate the dark sector via freeze-in by its decays $h \to \varphi\varphi, \chi\chi$, induced by the interaction terms $\frac{1}{\sqrt{2}}\lambda_{\varphi H}\langle H^0\rangle h\varphi^2$ and $\frac{1}{2}y_\varphi \sin\theta h\overline{\chi^c}\chi$. In the following we describe how to infer the resulting SIMP abundance, based on simple arguments of energy and entropy conservation. First we describe how the initial dark sector energy density is generated, before using entropy conservation to connect it to the $4 \to 2$ freeze-out results derived in the previous section.

The evolution of the energy density ρ' of the dark sector is described by adding the production term to the Boltzmann equation (8.6) (cf. eqn. 5.48):

$$\frac{d\rho'}{dt} + CH\rho' = \frac{g_i}{(2\pi)^3}\int f_h(p)E_h(p)\Gamma_h\left(E_h(p)\right)d^3p = \Gamma_{h\to\text{dark}}m_h n_h(T), \tag{8.31}$$

where production modes other than Higgs decay have been neglected. This can be rewritten as [138]

$$\frac{d\left(\rho'/\rho\right)}{dT} = -\frac{1}{HT\rho}\Gamma_{h\to\text{dark}}m_h n_h(T)\,, \tag{8.32}$$

assuming that all dark sector particles are relativistic while freeze-in production through the Higgs portal is efficient. $\Gamma_{h\to\text{dark}}$ is the total decay rate into hidden sector particles:

$$\Gamma_{h\to\text{dark}} \equiv \Gamma_{h\to\varphi\varphi} + \Gamma_{h\to\chi\chi} = \frac{\lambda_{\varphi H}^2\langle H^0\rangle^2}{16\pi m_h}\sqrt{1-\frac{4m_\varphi^2}{m_h^2}} + \frac{m_h}{16\pi}y_\varphi^2\sin^2\theta\left(1-\frac{4m_\chi^2}{m_h^2}\right)^{3/2}. \tag{8.33}$$

Eqn. (8.32) can now be solved, taking $\rho'/\rho = 0$ as boundary condition at high temperature and integrating down to $T = 10\,\text{GeV}$, below which energy transfer through the Higgs portal is very suppressed. We can now use the standard expressions for the energy density and entropy density in thermal equilibrium[7] given in section 5.1 to determine T'_{fi} at the end of freeze-in production

$$T'_{\text{fi}} = T_{\text{fi}}\left(\frac{g_{\text{SM}}(T_{\text{fi}})}{g_{\text{dark}}(T'_{\text{fi}})}\cdot\left.\frac{\rho'}{\rho}\right|_{\text{fi}}\right)^{1/4} \tag{8.34}$$

[7] To use an equilibrium description, we need to assume that $2 \to 4$ number changing interactions have equilibrated the dark sector before it becomes non-relativistic. This results in a lower limit on the coupling strength, which is weaker than that from requiring non-relativistic freeze-out and hence always satisfied for the parameters we consider.

and correspondingly the entropy ratio

$$\zeta \equiv \frac{s}{s'} = \left(\frac{T}{T'}\right)^3 \frac{h_{\text{eff}}(T)}{h'_{\text{eff}}(T')}\Big|_{T=10\,\text{GeV}} \simeq 4.5\times 10^5 \left(\frac{\lambda_{\varphi H}}{10^{-10}}\right)^{-3/2} + 7.4\times 10^5 \left(\frac{y_\varphi \sin\theta}{10^{-10}}\right)^{-3/2}, \tag{8.35}$$

where we have taken $h_{\text{eff}} = 86.3$ and $h'_{\text{eff}} = 2.75$ at $T = 10$ GeV, where energy transfer through the Higgs portal is completed.

Specifying the relation between visible and dark sector thermal baths by the entropy ratio $\zeta \equiv \frac{s}{s'}$ has the advantage that it is conserved when the sectors are decoupled [8, 245].[8] Having determined ζ after the freeze-in of the dark sector energy density is complete, we can calculate the temperature at any time t or SM temperature T by solving eqn. (8.35) with the appropriate expressions for the number of effective degrees of freedom in either sector $h_{\text{eff}}(T)$ and $h'_{\text{eff}}(T')$. This could be used to recast the instantaneous freeze-out result for the relic abundance eqn. (8.19) in terms of ζ instead of the T/T' parameter. Or simpler, we can apply the instantaneous freeze-out approximation introduced in eqn. (8.13) directly to find:

$$Y_{\chi,0} = \frac{n^{\text{eq}}_\chi(T'_{\text{fo}})}{s(T_{\text{fo}})} = \frac{45}{4\pi^4}\frac{g_\chi}{h_{\text{eff}}(T_{\text{fo}})}\left(\frac{T'_{\text{fo}}}{T_{\text{fo}}}\right)^3\left(\frac{m_\chi}{T'_{\text{fo}}}\right)^2 K_2\left(\frac{m_\chi}{T'_{\text{fo}}}\right) = \frac{1}{\zeta}F\left(\frac{m_\chi}{T'_{\text{fo}}}\right) \tag{8.36}$$

where

$$F(x) \equiv K_2(x)/[xK_1(x) + 4K_2(x)] \tag{8.37}$$

follows from the effective number of degrees of freedom (eqn. 5.19) contributing to the hidden sector entropy density at freeze-out

$$h'_{\text{eff}}(T'_{\text{fo}}) = \frac{45}{4\pi^4} g_\chi \left[\left(\frac{m_\chi}{T'_{\text{fo}}}\right)^3 K_1\left(\frac{m_\chi}{T'_{\text{fo}}}\right) + 4\left(\frac{m_\chi}{T'_{\text{fo}}}\right)^2 K_2\left(\frac{m_\chi}{T'_{\text{fo}}}\right)\right]. \tag{8.38}$$

Here, we have used the non-relativistic form of the equilibrium abundance n and s as introduced in section 5.1 and used that the scalar φ does not contribute significantly to s' at the time of freeze-out.

Equation (8.36) is a general result that applies to any decoupled dark sector, independent of the cosmological history that led to the entropy ratio ζ or the type of number changing interactions that keeps the dark sector in chemical equilibrium until T'_{fo}. Similar results have been obtained by [245] in the case of a real scalar SIMP, and the generality of eqn. (8.36) has subsequently been pointed out by [146].

Taking the result for the dark sector entropy from eqn. (8.35), we can use eqn. (8.36) and the freeze-out condition $\Gamma_{4\to 2}(T'_{\text{fo}}) = H(T_{\text{fo}})$ to calculate the self-interaction strength $\langle\sigma v^3\rangle$ necessary to obtain the observed relic abundance after freeze-out of $4 \to 2$ annihilations. This is shown in fig. 8.6, an analog to fig. 8.5 but showing contours of the portal terms $\lambda_{\varphi H}$ or $\sin\theta$ necessary to reproduce the observed dark matter abundance in the (m_χ, y)-plane (assuming only one of the portals is non-vanishing). This paints a complete picture of the dark matter production mechanism, determining the relic abundance in terms of fundamental parameters of the theory, rather than $T_{\text{fo}}/T'_{\text{fo}}$.

[8] This holds unless entropy is produced in either sector, e.g. from a late-decaying particle or first-order phase transition. Throughout this thesis, it is assumed that the early Universe at the temperatures considered is described by standard cosmology plus the explicitly added degrees of freedom, where no significant entropy production occurs at the temperatures considered.

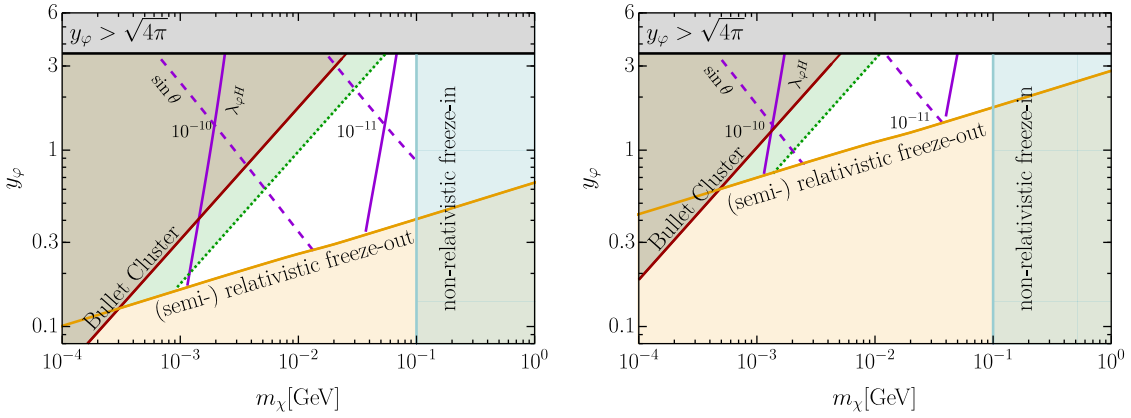

Figure 8.6: Contours of the portal interaction strength leading to the observed dark matter abundance for given values of the Yukawa coupling and the dark matter mass. The light-blue region where energy transfer from the visible to the dark sector can continue while the dark sector is already becoming non-relativistic is disregarded in our analysis. The meaning of the other colored regions is as in Fig. 8.5.

In addition to the previous restrictions to the parts of parameter space where the Yukawa coupling is perturbative and the $4 \to 2$ interaction only decouples after the dark matter has become non-relativistic, we here restrict our analysis to values of the dark matter mass $\leq 0.1\,\text{GeV}$ to ensure that the hidden sector particles are relativistic during freeze-in and the Boltzmann equation eqn. (8.32) holds. Under these assumptions, and imposing the constraints on the strength of the self-interaction from cluster collision observations, reproducing the observed dark matter abundance requires $3(3) \times 10^{-12} \lesssim \sin\theta \lesssim 3(0.4) \times 10^{-9}$, or $6(6) \times 10^{-12} \lesssim \lambda_{\varphi H} \lesssim 3(2) \times 10^{-10}$, for $m_\varphi/m_\chi = 3\,(10)$.

8.4 Discussion

In this chapter, we have introduced sterile neutrinos as dark matter candidates and investigated their production through the SIMP mechanism, where their relic abundance is determined by self-interactions. In the following we review the general SIMP phenomenology illustrated by the above results, before comparing the Majorana fermion case to other SIMP studies in the literature. Finally, we discuss synergies and differences of the proposed production mechanism with other phenomenology generally associated with sterile neutrinos.

Self-annihilating decoupled dark sectors The WIMP mechanism of dark matter production relates the dark matter relic density to the strength of dark matter annihilation into Standard Model particles, which concrete WIMP models relate to signal expectations at dark matter direct detection, indirect detection and collider experiments. The SIMP mechanism of dark matter production in contrast relates the dark matter density today to the strength of number-changing processes within the dark sector, related to the present day observable of dark matter self-interactions. Some support is lent to the SIMP scenario by the possible role of DM self scattering in addressing the small scale puzzles of the ΛCDM paradigm (see section 4.2).

The original self-interacting dark matter proposal [8] suffered from problems of erasure of small scale structure and too strong self-interactions, which can be successfully avoided if the dark sector is either kinetically connected to the SM bath or the initial entropy in the dark sector is much smaller than in the visible sector (see introduction in sec. 8.2). Only the latter is possible for $4 \to 2$ annihilating dark matter, such as fermionic SIMPs, illustrating a difficulty for fermionic SIMP candidates: $4 \to 2$ interactions are rare, and they decouple relatively early, i.e. at relatively small $T'/m_{\rm DM}$, even if couplings are close to the perturbativity limit. The depletion of an initial self-thermal dark matter abundance is hence relatively inefficient (cf. eqn. (8.36) and illustrative discussion in [254]), and in the present setup, we require an already dilute dark sector before the final abundance is determined by SIMP freeze out (for example, we need $s'/s \in [10^{-10}, 10^{-5}]$ in the EFT scenario of sec. 8.2.2).

On the other hand, from the perspective of other production mechanisms, like freeze-in or dark matter production associated to inflation, the SIMP mechanism can open parameter space where dark matter would otherwise be underproduced [146] or have too large velocity dispersion. Self-thermalisation can in these cases enhance the number density, reduce the velocity dispersion, as well as relate the final abundance to a low scale process observable today: dark matter self scattering.

Majorana fermions as SIMPs We have for the first time considered the scenario of Majorana SIMPs, where the relic abundance of a Majorana fermion dark matter candidate is determined by its self-interactions, which we have described by a a dimension-six operator suppressed by the scale Λ. To calculate the relic abundance, we have assumed negligible interactions between this dark sector and the bath of Standard Model particles. This allows for a dark sector that is thermalised at temperature $T' < T$, but introduces a dependence on the cosmological initial condition which can be parameterised by the temperature ratio at freeze-out, $T/T'|_{\rm fo}$, or the entropy ratio between the two sectors.

We have shown that the Majorana fermions can account for the observed dark matter relic density with their relic abundance determined by the freeze-out of $4 \to 2$ interactions in section 8.2.2. Imposing that the DM particles are non-relativistic at freeze-out, that self-interaction constraints are observed and that the suppression scale of the dimension-6 operator $\Lambda \leq m_\chi$, our results indicate that Majorana SIMPs are viable for $500\,\text{keV} \lesssim m_\chi \lesssim 20\,\text{GeV}$, for a suppression scale of $5\,\text{MeV} \lesssim \Lambda \lesssim 20\,\text{GeV}$, and that the ratio of temperatures between the visible and dark sectors at freeze-out is required to be $25 \lesssim T_{\rm fo}/T'_{\rm fo} \lesssim 400$. For some of these choices of parameters, the self-scattering can be strong enough to lead to observable effects on astrophysical scales, while structure formation constraints related to dark matter free streaming are never of relevance for the relevant mass range and low dark matter temperatures.

To check the viability of the EFT description, we also considered a toy model where the dimension-6 operator is generated by the exchange of a scalar singlet in section 8.3. In this case, reproducing the correct relic abundance requires the Yukawa coupling between the singlet scalar and the sterile neutrinos to be larger than 0.12(0.6) and the Majorana fermion mass to be in the range $300\,\text{keV} \lesssim m_\chi \lesssim 3\,\text{TeV}$ ($500\,\text{keV} \lesssim m_\chi \lesssim 3\,\text{GeV}$) when the scalar mass is 3 (10) times larger than the dark matter mass. This toy model allows for population of the dark sector via freeze-in through the Higgs-portal, which we have investigated in section 8.3.2. Here, rare invisible decays of the SM Higgs transfer energy to the dark sector, illustrating a possible origin of the low-temperature dark sector bath.

Sterile neutrinos as SIMPs The gauge singlet fermion χ allows for the portal coupling $y_\chi \bar{L}\tilde{H}\chi$ to the Standard Model lepton doublet, as introduced in section 8.1. Having ignored this coupling to focus on the effect and origin of self-interactions above, we now comment on its implications for sterile neutrino SIMP dark matter.

The neutrino portal can induce dark matter decay, producing a flux of high energy particles that could be detected by terrestrial or satellite experiments. In particular, the loop-induced decay into a photon and an active neutrino $\chi \to \nu\gamma$ results in monochromatic gamma rays with energy $E_\gamma = m_\chi/2$ at the rate [223]

$$\Gamma_{\chi\to\nu\gamma} = \frac{9\alpha_{\mathrm{em}} G_F^2 m_\chi^5}{(4\pi)^4} \left(\frac{y_\nu \langle H\rangle}{m_\chi}\right)^2 , \tag{8.39}$$

where α_{em} is the electromagnetic fine structure constant, G_F is the Fermi constant and $\langle H\rangle = 174$ GeV is the vacuum expectation value of the SM Higgs doublet. These monoenergetic gamma rays are searched for at gamma ray telescopes (see section 4.3), and limits on their fluxes can be translated into a limit on the Yukawa coupling (see e.g. [178]), roughly approximated by

$$y_\chi \lesssim 10^{-16} \left(\frac{\mathrm{MeV}}{m_\chi}\right)^{3/2} , \tag{8.40}$$

for $100\,\mathrm{keV} \lesssim m_\chi \lesssim 100\,\mathrm{GeV}$. Future gamma-ray telescopes like the proposed AMEGO [165] or e-ASTROGAM [167] concepts can improve the sensitivity by an order of magnitude in the mass range $\sim 0.3-30\,\mathrm{MeV}$, which is of particular interest to sterile neutrino SIMPs that can have astrophysically relevant self-interaction cross sections (cf. 8.3). This conjunction of the observation of dark matter self-interactions in astronomical structures and the observation of a line signal in the energy range $250\,\mathrm{keV} \lesssim E_\gamma \lesssim 10\,\mathrm{GeV}$ in the gamma ray sky would lend support to the scenario where sterile neutrino SIMPs make up the dark matter of the Universe.

As discussed in section 8.1, the bound in eqn. (8.40) already implies that the sterile neutrino dark matter candidate χ contributes no more than $10^{-15}\,\mathrm{eV}(m_\chi/\mathrm{MeV})^{-4}$ to the active neutrino masses. This is negligible compared to the observed mass splittings $\sqrt{\Delta m_{21}^2} \sim 0.01\,\mathrm{eV}$, meaning that they must be generated by other fermion singlets or a different mechanism.

In the discussion of sterile neutrino production mechanisms, it is of particular interest whether the proposed mechanism can be seen as an extension to standard DW or SF sterile neutrino production through the neutrino portal (see sec. 8.1). Thermalising the sterile neutrino population can reduce their average momentum, potentially alleviating structure formation constraints, and increase their abundance compared to the freeze-in population obtained without self-thermalisation, leading to smaller required portal couplings. A similar scenario to ours has been studied by Hansen&Vogl [238], who consider a dark sector consisting of a sterile neutrino and a real scalar, which self-thermalises by number changing interactions of the scalar. The number changing interactions in their case freeze out while the sterile neutrinos are still relativistic, allowing for larger final abundances than we can obtain from non-relativistic freeze-out of sterile neutrino $4 \to 2$ interactions here (cf. eqn. 8.36). They find that sterile neutrino dark matter through the neutrino portal is ruled out for $m_\chi \gtrsim 60\,\mathrm{keV}$, while we require $m_\chi \gtrsim 500\,\mathrm{keV}$ for our non-relativistic treatment to be reliable and to avoid $2 \to 2$ self-interaction constraints. With the methods laid out in this chapter, it is not possible to conclusively rule out whether *relativistically* decoupling $4 \to 2$ interactions can yield the observed relic abundance by thermalising an

initial abundance generated through the neutrino portal. This would require simulating the non-thermal phase space distribution generated by DW/SF production (this is standard and covered by publicly available codes like [258]) as well as relativistic thermally averaged cross sections for the $4 \to 2$ process, techniques for which have only recently been developed in the simpler setup of a SIMP real scalar [128]. This question of whether self-thermalised sterile neutrino dark matter that is initially produced through the neutrino portal is possible is an interesting target for future work.

Chapter 9

Conclusions

The nature of dark matter is a major open question in physics, spanning the disciplines of cosmology, astronomy and particle physics. There exists ample evidence for the existence of dark matter (see section 3.1), but to date there is no unambiguous signal to single out one of the many classes of objects that could account for it. The purpose of dark matter phenomenology is then to investigate these classes of objects for specific signatures that can be searched for to identify dark matter.

This work investigated different scenarios of thermal relic dark matter, where dark matter consists of particles whose relic density is determined by thermal processes in the early Universe. The starting point for the study of thermal relic dark matter was the one positively known dark matter quantity, its relic density, which in the models considered in this thesis is either determined by freeze-out of depletion processes, or freeze-out of production processes (referred to as "freeze-in of dark matter").

In the current absence of strong theoretical guidance on the nature of particle physics beyond the Standard Model, it seems prudent to study generic models, and models with the smallest number of ingredients promise to best represent the generic signatures we can expect of dark matter. However, restricting ourselves to the simplest models, we can miss important signatures that arise only in non-minimal dark sectors.

In this thesis, generic thermal relic production processes were reviewed in chapter 5. Chapters 6, 7 and 8 go beyond minimality by adding additional dark matter flavours to the dark sector, or allowing for strong self-interactions within the dark sector. In all cases, we find signatures that can be used to probe these scenarios, which are not present in their minimal counterparts, some of which are not the focus of traditional WIMP searches and warrant dedicated attention.

Chapter 6 considered extending the simplest (by number of degrees of freedom) dark matter model, the real scalar singlet ϕ, by a second scalar singlet flavour. While the scalar singlet is a viable WIMP candidate, we chose to focus on the feebly coupled case, which can be virtually impossible to identify in the single-component case. We found that freeze-in, either through the Higgs-portal or by coupling the real scalar through a heavy charged fermion to the SM leptons, generically produces both dark matter candidates, and that the same couplings that determine the relic abundance lead to dark matter decay into gamma rays $\phi_2 \to \phi_1\gamma\gamma$. These distinct signatures in gamma ray spectra are a possible smoking-gun dark matter signature that is not present in the corresponding minimal scenario, advocating future MeV-GeV gamma ray searches.

In chapter 7, we consider a t-channel mediated fermionic dark matter model, coupled

to the visible sector by a leptophilic charged scalar Σ. As in chapter 6, we study the effect of the presence of two dark matter flavours $\psi_{1,2}$ on relic abundance and observational signatures, this time considering the full range of couplings, from feeble values to the limit of perturbative unitarity. Much of the parameter space is ruled out by overabundance, but viable production regimes exist for either feeble or WIMP-like couplings. As in the scalar case, we find the possibility of distinctive gamma ray signals from $\psi_2 \to \psi_1\gamma$ decay if ψ_2 is produced by freeze-in, especially if ψ_1 is very light and behaves as hot dark matter or dark radiation. In the case where both ψ_i have large couplings, ψ_2 decay is fast and dark matter today is comprised solely of ψ_1. However, the heavier dark matter flavour can have a large impact on dark matter production. In particular, we find that a large boost of the present-day annihilation signal is possible, which would seem insensible in the corresponding single-flavour model. This indicates that the observation of a dark matter decay signal at upcoming gamma ray telescopes can happen at any moment, even when their sensitivity does not reach the target from canonical thermal production.

Finally, chapter 8 considered extending the sterile neutrino dark matter framework by dark matter self-interactions, studying the scenario where the dark matter relic abundance is determined by freeze-out of $4 \to 2$ reactions. This is the first implementation of the SIMP mechanism for Majorana fermion dark matter. This production mechanism can work entirely within the dark sector, but requires that the dark sector temperature is significantly smaller than that of the visible sector. The final relic abundance of the self-annihilating decoupled dark sector is then determined by its freeze-out temperature and the ratio of entropy in the dark and visible sectors. As result, we find that MeV to GeV-scale dark matter masses are viable, with dark matter self-interactions as the most promising signature for MeV-scale masses.

The quest to identify the nature of dark matter is well underway, and the most promising candidates are being searched for by many complementary strategies. In the absence of guidance from particle theory, phenomenological models can illustrate possible signals, point out interesting benchmarks or caution against overzealous conclusions. In the absence of signals, however, all we can do is to turn every stone. The work presented in this thesis illustrates that indirect signals not usually associated to minimal dark matter scenarios are not only possible, but can be powerful, specific probes of non-minimal dark sectors. Further, probes of dark-sector internal interactions may need to be further developed in the unlucky scenario where dark-to-visible interactions play little role in dark matter phenomenology.

Acknowledgements

I would like to thank my thesis advisor Alejandro Ibarra, for having me as a PhD student, for ideas, advice, travel and for his immense support. I hope that his curiosity and creativity will continue to shape my ideal of science. I was lucky to be able to work on a broad range of topics and am curious where they will lead in the years to come. I want to thank Mathias Garny for advice and all his papers cited in this work.

The scientific environment created by the members and guests of T30d, the TUM HEP community, the SFB1258 seminars and by generous travel opportunities was a privilige to enjoy. I would like to thank Karin for taking care of us PhD students and Petra for excellent organisation. I want to thank the Weiler group for hospitality and SFB42 for welcome distraction. The PhD journey would not be nearly as fun without the international community of PhD students, in particular Martin, Sebastian, Andreas, Sebastian, Max, Jovana, Patrick, Anja and Gauri. Special thanks go to my seniors Andrea, Takashi and Cesar, who it was a pleasure to work with.

I am deeply grateful to my parents, siblings and grandparents for love and support and science. Finally, I want to thank Sabine, for beyond physics.

Appendix A

Numerical Solution of the Boltzmann Equation

This appendix elaborates on the numerical solution of the coupled system of Boltzmann equations (7.14) in Chapter 7, repeated here for convenience:

$$\begin{aligned}\frac{d\ln Y_i}{dx} = &-\sum_j \left[\frac{\langle\sigma v\rangle^{\rm ann}_{ij\to AB} s Y_i \frac{Y_j^{\rm eq}}{Y_i^{\rm eq}}}{x\tilde{H}}\right]\left(\frac{Y_j}{Y_i}\frac{Y_i^{\rm eq}}{Y_j^{\rm eq}} - \frac{Y_i^{\rm eq\,2}}{Y_i^2}\right)\\ &-\sum_j \left[\frac{\langle\sigma v\rangle^{\rm sca}_{iA\to jB} s Y_A^{\rm eq}}{x\tilde{H}} + \frac{\tilde{\Gamma}_{i\to j}}{x\tilde{H}}\right]\left(1 - \frac{Y_j}{Y_i}\frac{Y_i^{\rm eq}}{Y_j^{\rm eq}}\right).\end{aligned} \tag{A.1}$$

Here $i \in \{\Sigma, \psi_2, \psi_1\}$, the thermally averaged cross section $\langle\sigma v\rangle$ is defined in eqn. (5.32) and the thermally averaged decay rate is given by $\tilde{\Gamma}_{i\to j} = \Gamma_{i\to j}/\langle\gamma\rangle = \Gamma_{i\to j}\frac{K_1(m_i/T)}{K_2(m_i/T)}$. We take $Y_\Sigma = Y_{\Sigma^+} + Y_{\Sigma^-}$. The thermally averaged cross sections were calculated using FeynRules [156], CalcHEP [157] and micrOMEGAs [126], the three-body decay rate $\Gamma_{\psi_2\to\psi_1 l^+ l^-}$ is taken from [183]. The processes considered are listed in Table A.1. The differential equations are then solved using standard routines in Mathematica [179].

initial state		final state		g_i scaling
Σ^+	Σ^-	γ	γ	1
		γ	Z	
		Z	Z	
		l^+	l^-	
Σ^+	Σ^+	l^+	l^+	$g_1^2, g_1 g_2, g_2^2$
ψ_i	Σ^+	l^+	γ, Z	g_i^2
ψ_i	ψ_j	l^+	l^-	$g_i^2 g_j^2$
ψ_i	$l^\pm$	ψ_j	$l^\pm$	$g_i^2 g_j^2$
$\Sigma^\pm$		ψ_i	$l^\pm$	g_i^2
ψ_2		ψ_1	l^+l^-	$g_1^2 g_2^2$

Table A.1: Annihilation, scattering and decay processes considered.

Annihilation In the annihilation terms, the following factors of two need to be accounted for: The $\langle\sigma v\rangle^{\text{ann}}_{ii}$ term annihilates 2 particles, compensating for the combinatorical factor of $1/2$ that needs to be introduced to avoid double counting of annihilating pairs. Casting the equations in terms of $Y_{\Sigma^+ + \Sigma^-}$, contributions to $\langle\sigma v\rangle_{\Sigma\Sigma}$ with $\Sigma^+\Sigma^+$ in the initial state need to be multiplied by $2 \times 2 \times 1/2 \times 1/4 = 1/2$ (for the number of annihilated particles, the conjugate process, double counting of annihilating pairs and for $Y^2_{\Sigma^+} = Y^2_\Sigma/2^2$ respectively). $\Sigma^+\Sigma^-$ channels receive $2 \times 1 \times 1 \times 1/4 = 1/2$.

Long before dark matter freeze-out, the annihilation rate can be much faster than the Hubble rate. In this case, it is useful for numerical stability to cap $[\dots]$ at some large value to not have to deal with overly stiff differential equations. This is sufficient for Y_i to follow Y_i^{eq} closely long before freeze-out and by construction has no effect on freeze-out:

$$\left[\frac{\langle\sigma v\rangle^{\text{ann}}_{ij\to AB} s Y_i \frac{Y_j^{\text{eq}}}{Y_i^{\text{eq}}}}{x\tilde{H}}\right] \to \text{Min}\left[1000\,,\ \frac{\langle\sigma v\rangle^{\text{ann}}_{ij\to AB} s Y_i \frac{Y_j^{\text{eq}}}{Y_i^{\text{eq}}}}{x\tilde{H}}\right] \tag{A.2}$$

Conversion The terms in the second line of eqn. (A.1) correspond to conversion processes, which ensure chemical equilibrium if the $[\dots]$-terms are large. In this case, the evolution equations for the species $i \in S$ in chemical equilibrium can be summed,

$$\frac{d\ln Y_S}{dx} = \sum_{i\in S} \frac{Y_i^{\text{eq}}}{Y_S^{\text{eq}}} \frac{d\ln Y_i}{dx}\,, \qquad Y_i = Y_S \frac{Y_i^{\text{eq}}(T)}{Y_S^{\text{eq}}(T)}\,, \tag{A.3}$$

where the fast conversion terms now cancel. In practice, we assume that all dark sector particles start out in thermal and chemical equilibrium at $T \gtrsim \text{Max}_i(m_i)$[1]. Particle species are subsequently decoupled when their conversion rate into the remaining summed species drops below $100Hx$ (and at the same time the conversion rate of the remaining summed species into the species in question is below this value):

$$\begin{aligned}\text{Max}\Bigg(&\sum_{j\in\{\text{summed}\}/\{i\}} \left[\frac{\langle\sigma v\rangle^{\text{sca}}_{iA\to jB} s Y_i}{x\tilde{H}} \frac{Y_A^{\text{eq}}}{Y_i} + \frac{\tilde{\Gamma}_{i\to j}}{x\tilde{H}}\right]\,, \\ &\sum_{j\in\{\text{summed}\}/\{i\}} \left[\frac{\langle\sigma v\rangle^{\text{sca}}_{jB\to iA} s Y_j}{x\tilde{H}} \frac{Y_B^{\text{eq}}}{Y_j} + \frac{\tilde{\Gamma}_{j\to i}}{x\tilde{H}}\right] \frac{Y_j^{\text{eq}}}{\sum_{k\in\{summed\}/\{i\}} Y_k^{\text{eq}}}\Bigg) < 100\,.\end{aligned} \tag{A.4}$$

From this point, the evolution of Y_i is treated separately. The species i usually drops out of CE shortly thereafter.

Decay vs. scattering in conversion processes In eqn. (A.1), we consider only the lowest-order contributions to the collision term (eqn. 5.28) in an expansion by number of external states for every process that affects the dark sector abundances. Processes involving additional external particles are expected to be suppressed by a phase space factor and additional powers of couplings. For processes that deplete the dark sector abundance, $2 \to 2$ annihilation is lowest order, since decays of a $\mathbb{Z}_2$-odd dark sector particle into $\mathbb{Z}_2$-even SM

[1] Except if a species i is feebly coupled, as estimated by the analytical freeze-in condition eqn. (7.6). In that case, large reaction rates are never a problem, and we start with the initial condition $Y_i(T_{\text{initial}}) = 0$ appropriate to freeze-in.

particles are forbidden[2]. For $i \to j$ conversion processes that change one dark sector particle into another, these are two-body decays for $\Sigma \to \psi_i$, while for $\psi_1 \to \psi_2$ conversion the three body decay $\psi_2 \to \psi_1 l^+ l^-$ and the crossed scattering process $\psi_2 l^+ \to \psi_1 l^+$ contribute at the same level and are both taken into account.

There are however situations in which this power counting breaks down:

- *Large couplings:* When couplings in the theory approach the perturbativity bound, the penalty for the involvement of an additional particle in a reaction drops. This can be seen in the dominance of $\psi_2 l \to \psi_1 l \propto g_1^2 g_2^2$ production of FIMP ψ_2 over the Σ-decay mode $\Sigma \to \psi_1 l \propto g_1^2$ in the WIMP-FIMP regime in fig. 7.5.

- *Kinematic suppression:* If $m_\Sigma \sim m_\psi$, the decay rate $\Gamma_{\Sigma \to \psi l}$ is kinematically suppressed, and processes like $\Sigma\gamma \to \psi l$ involving an additional external particle may be favoured in spite of the additional small coupling involved.

The second case has been investigated in work focusing on the degenerate region in the single-component leptophilic model [140] (and associated quark-coupled models [172, 173]), finding that it is important to include scattering processes like $\Sigma\gamma \to \psi l$ into the analysis if $m_\Sigma \sim m_\psi$, both for freeze-in, as well as for mediator-conversion driven freeze-out. This effect is explored in Figure A.1, which shows reaction rates for $\Sigma \to \psi l$ and $\Sigma\gamma \to \psi l$[3]. Note that $\sigma_{\Sigma\gamma \to \psi l}$ has a soft divergence related to the photon that needs to be regulated. In [172], this has been done by imposing a minimal process energy as $s_{\min} = (m_\Sigma + m_{\text{cut}})^2$. Physically, this can be motivated by the thermal mass of the photon, expected to be roughly $\mathcal{O}(T)$ [139]. From Figure A.1 it is clear that in the non-degenerate case the scattering process is irrelevant for processes happening at $T \lesssim m_\Sigma$ (such as freeze-in of ψ, which happens around $T \sim m_\Sigma$/few, or ψ freeze-out, happening at $T \ll m_\psi$). In the degenerate scenario shown, scattering can be relevant at $T \sim m_\Sigma$ and potentially down to dark matter freeze-out at much smaller temperatures for much more degenerate parameters.

As the aim of chapter 7 is to explore general implications of adding a second dark matter flavour to the leptophilic model, we choose to contend ourselves with the lowest order treatment, keeping in mind the limitations in the near-degenerate part of parameter space.

[2] Inverse decays odd + odd $\to$ even would be lower order, but are not possible kinematically in the considered model.

[3] $\Sigma\gamma \to \psi l$ is taken as example, the crossed process $\Sigma l \to \psi\gamma$ also contributes, as do those replacing γ with a Z-boson. Processes involving a Higgs particle are suppressed by the small lepton Yukawa coupling, and processes involving W-bosons and neutrinos are suppressed by a lepton mass insertion.

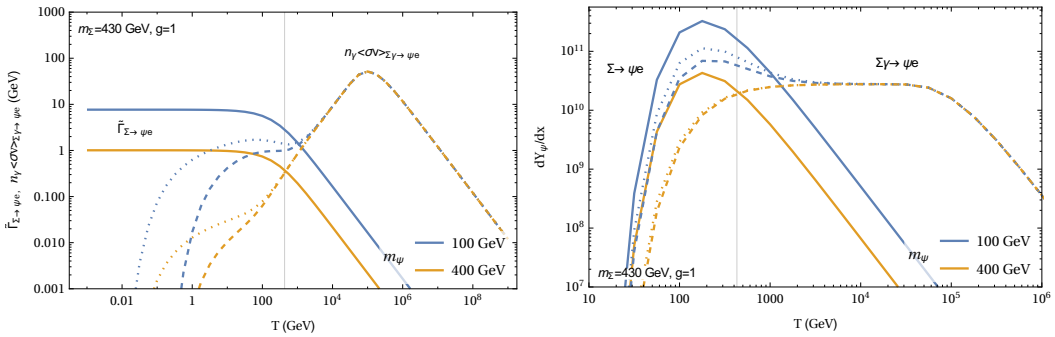

Figure A.1: *Left:* Decay rate $\tilde{\Gamma}_{\Sigma\to\psi e}$ (line) and scattering depletion rate $n_\gamma\langle\sigma v\rangle_{\Sigma\gamma\to\psi e}$ (regulated by $m_{\text{cut}} = 0.01, 2\,\text{GeV}$ (dotted, dashed)) as function of temperature. The charged scalar mass is fixed at 430 GeV (gray line at $T = m_\Sigma$), while a non-degenerate (blue) and near-degenerate (orange) scenario is shown for $m_\psi = 100, 400\,\text{GeV}$. In the degenerate case, the decay rate is kinematically suppressed, making scattering more relevant. *Right:* Resulting contribution to dY_ψ/dx in the freeze-in case from the two processes, illustrating that in both shown cases the integrated effect of decay is dominant (as $x \propto 1/T$).

Bibliography

[1] Edward W. Kolb and Michael S. Turner. *The Early Universe*. Number 69 in Frontiers in Physics. Addison-Wesley, Reading, Mass, 1990.

[2] Jean-Philippe Uzan. The big-bang theory: construction, evolution and status. June 2016. arXiv:1606.06112.

[3] Georges Aad et al. Observation of a new particle in the search for the Standard Model Higgs boson with the ATLAS detector at the LHC. *Phys. Lett. B*, 716:1–29, 2012. arXiv:1207.7214, doi:10.1016/j.physletb.2012.08.020.

[4] Serguei Chatrchyan et al. Observation of a New Boson at a Mass of 125 GeV with the CMS Experiment at the LHC. *Phys. Lett. B*, 716:30–61, 2012. arXiv:1207.7235, doi:10.1016/j.physletb.2012.08.021.

[5] M. Tanabashi et al. Review of Particle Physics. *Phys. Rev. D*, 98(3):030001, 2018. doi:10.1103/PhysRevD.98.030001.

[6] Gianfranco Bertone and M.P. Tait, Tim. A new era in the search for dark matter. *Nature*, 562(7725):51–56, 2018. arXiv:1810.01668, doi:10.1038/s41586-018-0542-z.

[7] Lawrence J. Hall, Karsten Jedamzik, John March-Russell, and Stephen M. West. Freeze-In Production of FIMP Dark Matter. *JHEP*, 03:080, 2010. arXiv:0911.1120, doi:10.1007/JHEP03(2010)080.

[8] Eric D. Carlson, Marie E. Machacek, and Lawrence J. Hall. Self-interacting dark matter. *Astrophys. J.*, 398:43–52, 1992. doi:10.1086/171833.

[9] Yonit Hochberg, Eric Kuflik, Hitoshi Murayama, Tomer Volansky, and Jay G. Wacker. Model for Thermal Relic Dark Matter of Strongly Interacting Massive Particles. *Phys. Rev. Lett.*, 115(2):021301, 2015. arXiv:1411.3727, doi:10.1103/PhysRevLett.115.021301.

[10] Johannes Herms, Alejandro Ibarra, and Takashi Toma. A new mechanism of sterile neutrino dark matter production. *JCAP*, 06:036, 2018. arXiv:1802.02973, doi:10.1088/1475-7516/2018/06/036.

[11] Johannes Herms and Alejandro Ibarra. Probing multicomponent FIMP scenarios with gamma-ray telescopes. *JCAP*, 03:026, 2020. arXiv:1912.09458, doi:10.1088/1475-7516/2020/03/026.

[12] Matthew D. Schwartz. *Quantum Field Theory and the Standard Model*. Cambridge University Press, 2014.

[13] K. Abe et al. Search for proton decay via $p \to e^+\pi^0$ and $p \to \mu^+\pi^0$ in 0.31 megaton·years exposure of the Super-Kamiokande water Cherenkov detector. *Phys. Rev. D*, 95(1):012004, 2017. arXiv:1610.03597, doi:10.1103/PhysRevD.95.012004.

[14] Fred Jegerlehner and Andreas Nyffeler. The Muon g-2. *Phys. Rept.*, 477:1–110, 2009. arXiv:0902.3360, doi:10.1016/j.physrep.2009.04.003.

[15] Stephen P. Martin. *A Supersymmetry primer*, volume 21, pages 1–153. 2010. arXiv:hep-ph/9709356, doi:10.1142/9789812839657_0001.

[16] Frank Wilczek. Problem of Strong P and T Invariance in the Presence of Instantons. *Phys. Rev. Lett.*, 40:279–282, 1978. doi:10.1103/PhysRevLett.40.279.

[17] Scott Dodelson. *Modern Cosmology*. Academic Press, Amsterdam, 2003.

[18] N. Aghanim et al. Planck 2018 results. VI. Cosmological parameters. 2018. arXiv:1807.06209.

[19] Alain Coc, Jean-Philippe Uzan, and Elisabeth Vangioni. Standard big bang nucleosynthesis and primordial CNO Abundances after Planck. *JCAP*, 10:050, 2014. arXiv:1403.6694, doi:10.1088/1475-7516/2014/10/050.

[20] Adam G. Riess et al. A 2.4% Determination of the Local Value of the Hubble Constant. *Astrophys. J.*, 826(1):56, 2016. arXiv:1604.01424, doi:10.3847/0004-637X/826/1/56.

[21] N. Jarosik et al. Seven-Year Wilkinson Microwave Anisotropy Probe (WMAP) Observations: Sky Maps, Systematic Errors, and Basic Results. *Astrophys. J. Suppl.*, 192:14, 2011. arXiv:1001.4744, doi:10.1088/0067-0049/192/2/14.

[22] F. Spite and M. Spite. Abundance of lithium in unevolved stars and old disk stars : Interpretation and consequences. *Astron. Astrophys.*, 115:357–366, November 1982.

[23] Brian D. Fields. The primordial lithium problem. *Ann. Rev. Nucl. Part. Sci.*, 61:47–68, 2011. arXiv:1203.3551, doi:10.1146/annurev-nucl-102010-130445.

[24] Lloyd Knox and Marius Millea. Hubble constant hunter's guide. *Phys. Rev. D*, 101(4):043533, 2020. arXiv:1908.03663, doi:10.1103/PhysRevD.101.043533.

[25] Steen Hannestad. What is the lowest possible reheating temperature? *Phys. Rev. D*, 70:043506, 2004. arXiv:astro-ph/0403291, doi:10.1103/PhysRevD.70.043506.

[26] Gianfranco Bertone and Dan Hooper. History of dark matter. *Rev. Mod. Phys.*, 90(4):045002, 2018. arXiv:1605.04909, doi:10.1103/RevModPhys.90.045002.

[27] V. C. Rubin, Jr. Ford, W. K., and N. Thonnard. Extended rotation curves of high-luminosity spiral galaxies. IV. Systematic dynamical properties, Sa → Sc. *ApJ*, 225:L107–L111, November 1978. doi:10.1086/182804.

[28] D. H. Rogstad and G. S. Shostak. Gross Properties of Five Scd Galaxies as Determined from 21-CENTIMETER Observations. *ApJ*, 176:315, September 1972. doi:10.1086/151636.

[29] M. Milgrom. A modification of the Newtonian dynamics as a possible alternative to the hidden mass hypothesis. *ApJ*, 270:365–370, July 1983. doi:10.1086/161130.

[30] Stacy McGaugh, Federico Lelli, and Jim Schombert. Radial Acceleration Relation in Rotationally Supported Galaxies. *Phys. Rev. Lett.*, 117(20):201101, 2016. arXiv:1609.05917, doi:10.1103/PhysRevLett.117.201101.

[31] Julio F. Navarro, Alejandro Benítez-Llambay, Azadeh Fattahi, Carlos S. Frenk, Aaron D. Ludlow, Kyle A. Oman, Matthieu Schaller, and Tom Theuns. The origin of the mass discrepancy-acceleration relation in ΛCDM. *Mon. Not. Roy. Astron. Soc.*, 471(2):1841–1848, 2017. arXiv:1612.06329, doi:10.1093/mnras/stx1705.

[32] J.I. Read. The Local Dark Matter Density. *J. Phys. G*, 41:063101, 2014. arXiv:1404.1938, doi:10.1088/0954-3899/41/6/063101.

[33] K. G. Begeman, A. H. Broeils, and R. H. Sanders. Extended rotation curves of spiral galaxies: dark haloes and modified dynamics. *Mon. Not. Roy. Astron. Soc.*, 249(3):523–537, 04 1991. doi:10.1093/mnras/249.3.523.

[34] F. Zwicky. Die Rotverschiebung von extragalaktischen Nebeln. *Helv. Phys. Acta*, 6:110–127, 1933. doi:10.1007/s10714-008-0707-4.

[35] Katherine Garrett and Gintaras Duda. Dark Matter: A Primer. *Adv. Astron.*, 2011:968283, 2011. arXiv:1006.2483, doi:10.1155/2011/968283.

[36] A.C. Fabian and S.W. Allen. X-rays from clusters of galaxies. In *21st Texas Symposium on Relativistic Astrophysics (Texas in Tuscany)*, pages 197–208, 2003. arXiv:astro-ph/0304020, doi:10.1142/9789812704009_0018.

[37] David Harvey, Richard Massey, Thomas Kitching, Andy Taylor, and Eric Tittley. The non-gravitational interactions of dark matter in colliding galaxy clusters. *Science*, 347:1462–1465, 2015. arXiv:1503.07675, doi:10.1126/science.1261381.

[38] Douglas Clowe, Marusa Bradac, Anthony H. Gonzalez, Maxim Markevitch, Scott W. Randall, Christine Jones, and Dennis Zaritsky. A direct empirical proof of the existence of dark matter. *Astrophys. J. Lett.*, 648:L109–L113, 2006. arXiv:astro-ph/0608407, doi:10.1086/508162.

[39] Image credit: X-ray: NASA/CXC/M.Markevitch et al. Optical: NASA/STScI; Magellan/U.Arizona/D.Clowe et al. Lensing Map: NASA/STScI; ESO WFI; Magellan/U.Arizona/D.Clowe et al. URL: https://www.nasa.gov/vision/universe/starsgalaxies/dark_matter_proven.html.

[40] Daniel J. Eisenstein et al. Detection of the Baryon Acoustic Peak in the Large-Scale Correlation Function of SDSS Luminous Red Galaxies. *Astrophys. J.*, 633:560–574, 2005. arXiv:astro-ph/0501171, doi:10.1086/466512.

[41] Matteo Viel, George D. Becker, James S. Bolton, and Martin G. Haehnelt. Warm dark matter as a solution to the small scale crisis: New constraints from high redshift Lyman-α forest data. *Phys. Rev. D*, 88:043502, 2013. arXiv:1306.2314, doi:10.1103/PhysRevD.88.043502.

[42] Volker Springel, Carlos S. Frenk, and Simon D.M. White. The large-scale structure of the Universe. *Nature*, 440:1137, 2006. arXiv:astro-ph/0604561, doi:10.1038/nature04805.

[43] Julio F. Navarro, Carlos S. Frenk, and Simon D.M. White. The Structure of cold dark matter halos. *Astrophys. J.*, 462:563–575, 1996. arXiv:astro-ph/9508025, doi:10.1086/177173.

[44] Julio F. Navarro, Carlos S. Frenk, and Simon D.M. White. A Universal density profile from hierarchical clustering. *Astrophys. J.*, 490:493–508, 1997. arXiv:astro-ph/9611107, doi:10.1086/304888.

[45] Samuel D. McDermott, Hai-Bo Yu, and Kathryn M. Zurek. Turning off the Lights: How Dark is Dark Matter? *Phys. Rev. D*, 83:063509, 2011. arXiv:1011.2907, doi:10.1103/PhysRevD.83.063509.

[46] Timothy D. Brandt. Constraints on MACHO Dark Matter from Compact Stellar Systems in Ultra-Faint Dwarf Galaxies. *Astrophys. J. Lett.*, 824(2):L31, 2016. arXiv:1605.03665, doi:10.3847/2041-8205/824/2/L31.

[47] Vid Irˇ sič, Matteo Viel, Martin G. Haehnelt, James S. Bolton, and George D. Becker. First constraints on fuzzy dark matter from Lyman-α forest data and hydrodynamical simulations. *Phys. Rev. Lett.*, 119(3):031302, 2017. arXiv:1703.04683, doi:10.1103/PhysRevLett.119.031302.

[48] Eric Armengaud, Nathalie Palanque-Delabrouille, Christophe Yèche, David J.E. Marsh, and Julien Baur. Constraining the mass of light bosonic dark matter using SDSS Lyman-α forest. *Mon. Not. Roy. Astron. Soc.*, 471(4):4606–4614, 2017. arXiv:1703.09126, doi:10.1093/mnras/stx1870.

[49] Anne M. Green and Bradley J. Kavanagh. Primordial Black Holes as a dark matter candidate. 7 2020. arXiv:2007.10722.

[50] Bernard Carr, Kazunori Kohri, Yuuiti Sendouda, and Jun'ichi Yokoyama. Constraints on Primordial Black Holes. 2 2020. arXiv:2002.12778.

[51] S. Tremaine and J.E. Gunn. Dynamical Role of Light Neutral Leptons in Cosmology. *Phys. Rev. Lett.*, 42:407–410, 1979. doi:10.1103/PhysRevLett.42.407.

[52] Alexey Boyarsky, Oleg Ruchayskiy, and Dmytro Iakubovskyi. A Lower bound on the mass of Dark Matter particles. *JCAP*, 03:005, 2009. arXiv:0808.3902, doi:10.1088/1475-7516/2009/03/005.

[53] Vid Iršič et al. New Constraints on the free-streaming of warm dark matter from intermediate and small scale Lyman-α forest data. *Phys. Rev.*, D96(2):023522, 2017. arXiv:1702.01764, doi:10.1103/PhysRevD.96.023522.

[54] David J. E. Marsh. Axion Cosmology. *Phys. Rept.*, 643:1–79, 2016. arXiv:1510.07633, doi:10.1016/j.physrep.2016.06.005.

[55] Mathias Garny, Andrea Palessandro, McCullen Sandora, and Martin S. Sloth. Theory and Phenomenology of Planckian Interacting Massive Particles as Dark Matter. *JCAP*, 02:027, 2018. arXiv:1709.09688, doi:10.1088/1475-7516/2018/02/027.

[56] John R. Ellis, Jihn E. Kim, and Dimitri V. Nanopoulos. Cosmological Gravitino Regeneration and Decay. *Phys. Lett. B*, 145:181–186, 1984. doi:10.1016/0370-2693(84)90334-4.

[57] Scott Dodelson and Lawrence M. Widrow. Sterile-neutrinos as dark matter. *Phys. Rev. Lett.*, 72:17–20, 1994. arXiv:hep-ph/9303287, doi:10.1103/PhysRevLett.72.17.

[58] Jonathan L. Feng. Dark Matter Candidates from Particle Physics and Methods of Detection. *Ann. Rev. Astron. Astrophys.*, 48:495–545, 2010. arXiv:1003.0904, doi:10.1146/annurev-astro-082708-101659.

[59] Jonathan L. Feng and Jason Kumar. The WIMPless Miracle: Dark-Matter Particles without Weak-Scale Masses or Weak Interactions. *Phys. Rev. Lett.*, 101:231301, 2008. arXiv:0803.4196, doi:10.1103/PhysRevLett.101.231301.

[60] David E. Kaplan, Markus A. Luty, and Kathryn M. Zurek. Asymmetric Dark Matter. *Phys. Rev. D*, 79:115016, 2009. arXiv:0901.4117, doi:10.1103/PhysRevD.79.115016.

[61] Lauren Anderson et al. The clustering of galaxies in the SDSS-III Baryon Oscillation Spectroscopic Survey: Baryon Acoustic Oscillations in the Data Release 9 Spectroscopic Galaxy Sample. *Mon. Not. Roy. Astron. Soc.*, 427(4):3435–3467, 2013. arXiv:1203.6594, doi:10.1111/j.1365-2966.2012.22066.x.

[62] Julien Baur, Nathalie Palanque-Delabrouille, Christophe Yeche, Alexey Boyarsky, Oleg Ruchayskiy, Éric Armengaud, and Julien Lesgourgues. Constraints from Ly-α forests on non-thermal dark matter including resonantly-produced sterile neutrinos. *JCAP*, 12:013, 2017. arXiv:1706.03118, doi:10.1088/1475-7516/2017/12/013.

[63] Matteo Viel, Julien Lesgourgues, Martin G. Haehnelt, Sabino Matarrese, and Antonio Riotto. Constraining warm dark matter candidates including sterile neutrinos and light gravitinos with WMAP and the Lyman-alpha forest. *Phys. Rev. D*, 71:063534, 2005. arXiv:astro-ph/0501562, doi:10.1103/PhysRevD.71.063534.

[64] Roberta Diamanti, Shin'ichiro Ando, Stefano Gariazzo, Olga Mena, and Christoph Weniger. Cold dark matter plus not-so-clumpy dark relics. *JCAP*, 1706(06):008, 2017. arXiv:1701.03128, doi:10.1088/1475-7516/2017/06/008.

[65] Torsten Bringmann. Particle Models and the Small-Scale Structure of Dark Matter. *New J. Phys.*, 11:105027, 2009. arXiv:0903.0189, doi:10.1088/1367-2630/11/10/105027.

[66] Sean Tulin and Hai-Bo Yu. Dark Matter Self-interactions and Small Scale Structure. 2017. arXiv:1705.02358.

[67] Liang Gao, Simon D.M. White, Adrian Jenkins, Felix Stoehr, and Volker Springel. The Subhalo populations of lambda-CDM dark halos. *Mon. Not. Roy. Astron. Soc.*, 355:819, 2004. arXiv:astro-ph/0404589, doi:10.1111/j.1365-2966.2004.08360.x.

[68] B. Moore, S. Ghigna, F. Governato, G. Lake, Thomas R. Quinn, J. Stadel, and P. Tozzi. Dark matter substructure within galactic halos. *Astrophys. J. Lett.*, 524:L19–L22, 1999. arXiv:astro-ph/9907411, doi:10.1086/312287.

[69] Stacy Y. Kim, Annika H. G. Peter, and Jonathan R. Hargis. Missing Satellites Problem: Completeness Corrections to the Number of Satellite Galaxies in the Milky Way are Consistent with Cold Dark Matter Predictions. *Phys. Rev. Lett.*, 121(21):211302, 2018. arXiv:1711.06267, doi:10.1103/PhysRevLett.121.211302.

[70] Michael Boylan-Kolchin, James S. Bullock, and Manoj Kaplinghat. Too big to fail? The puzzling darkness of massive Milky Way subhaloes. *Mon. Not. Roy. Astron. Soc.*, 415:L40, 2011. arXiv:1103.0007, doi:10.1111/j.1745-3933.2011.01074.x.

[71] Michael Boylan-Kolchin, James S. Bullock, and Manoj Kaplinghat. The Milky Way's bright satellites as an apparent failure of LCDM. *Mon. Not. Roy. Astron. Soc.*, 422:1203–1218, 2012. arXiv:1111.2048, doi:10.1111/j.1365-2966.2012.20695.x.

[72] Manoj Kaplinghat, Mauro Valli, and Hai-Bo Yu. Too Big To Fail in Light of Gaia. *Mon. Not. Roy. Astron. Soc.*, 490(1):231–242, 2019. arXiv:1904.04939, doi:10.1093/mnras/stz2511.

[73] B. Moore. Evidence against dissipationless dark matter from observations of galaxy haloes. *Nature*, 370:629, 1994. doi:10.1038/370629a0.

[74] Ben Moore, Thomas R. Quinn, Fabio Governato, Joachim Stadel, and George Lake. Cold collapse and the core catastrophe. *Mon. Not. Roy. Astron. Soc.*, 310:1147–1152, 1999. arXiv:astro-ph/9903164, doi:10.1046/j.1365-8711.1999.03039.x.

[75] Andrew Pontzen and Fabio Governato. How supernova feedback turns dark matter cusps into cores. *Mon. Not. Roy. Astron. Soc.*, 421:3464, 2012. arXiv:1106.0499, doi:10.1111/j.1365-2966.2012.20571.x.

[76] A. Burkert. The Structure of dark matter halos in dwarf galaxies. *IAU Symp.*, 171:175, 1996. arXiv:astro-ph/9504041, doi:10.1086/309560.

[77] Rachel Kuzio de Naray, Gregory D. Martinez, James S. Bullock, and Manoj Kaplinghat. The Case Against Warm or Self-Interacting Dark Matter as Explanations for Cores in Low Surface Brightness Galaxies. *Astrophys. J. Lett.*, 710:L161, 2010. arXiv:0912.3518, doi:10.1088/2041-8205/710/2/L161.

[78] Kyle A. Oman et al. The unexpected diversity of dwarf galaxy rotation curves. *Mon. Not. Roy. Astron. Soc.*, 452(4):3650–3665, 2015. arXiv:1504.01437, doi:10.1093/mnras/stv1504.

[79] David N. Spergel and Paul J. Steinhardt. Observational evidence for selfinteracting cold dark matter. *Phys. Rev. Lett.*, 84:3760–3763, 2000. arXiv:astro-ph/9909386, doi:10.1103/PhysRevLett.84.3760.

[80] Miguel Rocha, Annika H.G. Peter, James S. Bullock, Manoj Kaplinghat, Shea Garrison-Kimmel, Jose Onorbe, and Leonidas A. Moustakas. Cosmological Simulations with Self-Interacting Dark Matter I: Constant Density Cores and Substructure. *Mon. Not. Roy. Astron. Soc.*, 430:81–104, 2013. arXiv:1208.3025, doi:10.1093/mnras/sts514.

[81] Manoj Kaplinghat, Sean Tulin, and Hai-Bo Yu. Dark Matter Halos as Particle Colliders: Unified Solution to Small-Scale Structure Puzzles from Dwarfs to Clusters. *Phys.*

Rev. Lett., 116(4):041302, 2016. arXiv:1508.03339, doi:10.1103/PhysRevLett.116.041302.

[82] Annika H.G. Peter, Miguel Rocha, James S. Bullock, and Manoj Kaplinghat. Cosmological Simulations with Self-Interacting Dark Matter II: Halo Shapes vs. Observations. *Mon. Not. Roy. Astron. Soc.*, 430:105, 2013. arXiv:1208.3026, doi:10.1093/mnras/sts535.

[83] Felix Kahlhoefer, Manoj Kaplinghat, Tracy R. Slatyer, and Chih-Liang Wu. Diversity in density profiles of self-interacting dark matter satellite halos. *JCAP*, 12:010, 2019. arXiv:1904.10539, doi:10.1088/1475-7516/2019/12/010.

[84] Scott W. Randall, Maxim Markevitch, Douglas Clowe, Anthony H. Gonzalez, and Marusa Bradac. Constraints on the Self-Interaction Cross-Section of Dark Matter from Numerical Simulations of the Merging Galaxy Cluster 1E 0657-56. *Astrophys. J.*, 679:1173–1180, 2008. arXiv:0704.0261, doi:10.1086/587859.

[85] M. Aguilar et al. First Result from the Alpha Magnetic Spectrometer on the International Space Station: Precision Measurement of the Positron Fraction in Primary Cosmic Rays of 0.5–350 GeV. *Phys. Rev. Lett.*, 110:141102, 2013. doi:10.1103/PhysRevLett.110.141102.

[86] W.B. Atwood et al. The Large Area Telescope on the Fermi Gamma-ray Space Telescope Mission. *Astrophys. J.*, 697:1071–1102, 2009. arXiv:0902.1089, doi:10.1088/0004-637X/697/2/1071.

[87] A. Albert et al. Combined search for neutrinos from dark matter self-annihilation in the Galactic Centre with ANTARES and IceCube. 3 2020. arXiv:2003.06614.

[88] Hongwan Liu, Tracy R. Slatyer, and Jesús Zavala. Contributions to cosmic reionization from dark matter annihilation and decay. *Phys. Rev. D*, 94(6):063507, 2016. arXiv:1604.02457, doi:10.1103/PhysRevD.94.063507.

[89] Sergio Colafrancesco, S. Profumo, and P. Ullio. Multi-frequency analysis of neutralino dark matter annihilations in the Coma cluster. *Astron. Astrophys.*, 455:21, 2006. arXiv:astro-ph/0507575, doi:10.1051/0004-6361:20053887.

[90] S. P. Reynolds. Supernova remnants at high energy. *ARA&A*, 46:89–126, September 2008. doi:10.1146/annurev.astro.46.060407.145237.

[91] A.U. Abeysekara et al. Extended gamma-ray sources around pulsars constrain the origin of the positron flux at Earth. *Science*, 358(6365):911–914, 2017. arXiv:1711.06223, doi:10.1126/science.aan4880.

[92] Annika Reinert and Martin Wolfgang Winkler. A Precision Search for WIMPs with Charged Cosmic Rays. *JCAP*, 01:055, 2018. arXiv:1712.00002, doi:10.1088/1475-7516/2018/01/055.

[93] P. von Doetinchem et al. Cosmic-ray Antinuclei as Messengers of New Physics: Status and Outlook for the New Decade. 2 2020. arXiv:2002.04163.

[94] Johannes Herms, Alejandro Ibarra, Andrea Vittino, and Sebastian Wild. Antideuterons in cosmic rays: sources and discovery potential. *JCAP*, 02:018, 2017. arXiv:1610.00699, doi:10.1088/1475-7516/2017/02/018.

[95] Torsten Bringmann and Christoph Weniger. Gamma Ray Signals from Dark Matter: Concepts, Status and Prospects. *Phys. Dark Univ.*, 1:194–217, 2012. arXiv:1208.5481, doi:10.1016/j.dark.2012.10.005.

[96] M.L. Ahnen et al. Limits to Dark Matter Annihilation Cross-Section from a Combined Analysis of MAGIC and Fermi-LAT Observations of Dwarf Satellite Galaxies. *JCAP*, 02:039, 2016. arXiv:1601.06590, doi:10.1088/1475-7516/2016/02/039.

[97] Alejandro Ibarra, David Tran, and Christoph Weniger. Indirect Searches for Decaying Dark Matter. *Int. J. Mod. Phys.*, A28:1330040, 2013. arXiv:1307.6434, doi:10.1142/S0217751X13300408.

[98] Marco Cirelli, Gennaro Corcella, Andi Hektor, Gert Hutsi, Mario Kadastik, Paolo Panci, Martti Raidal, Filippo Sala, and Alessandro Strumia. PPPC 4 DM ID: A Poor Particle Physicist Cookbook for Dark Matter Indirect Detection. *JCAP*, 03:051, 2011. [Erratum: JCAP 10, E01 (2012)]. arXiv:1012.4515, doi:10.1088/1475-7516/2012/10/E01.

[99] Kevork N. Abazajian, Shunsaku Horiuchi, Manoj Kaplinghat, Ryan E. Keeley, and Oscar Macias. Strong constraints on thermal relic dark matter from Fermi-LAT observations of the Galactic Center. 3 2020. arXiv:2003.10416.

[100] Tansu Daylan, Douglas P. Finkbeiner, Dan Hooper, Tim Linden, Stephen K. N. Portillo, Nicholas L. Rodd, and Tracy R. Slatyer. The characterization of the gamma-ray signal from the central Milky Way: A case for annihilating dark matter. *Phys. Dark Univ.*, 12:1–23, 2016. arXiv:1402.6703, doi:10.1016/j.dark.2015.12.005.

[101] Richard Bartels, Suraj Krishnamurthy, and Christoph Weniger. Strong support for the millisecond pulsar origin of the Galactic center GeV excess. *Phys. Rev. Lett.*, 116(5):051102, 2016. arXiv:1506.05104, doi:10.1103/PhysRevLett.116.051102.

[102] Samuel K. Lee, Mariangela Lisanti, Benjamin R. Safdi, Tracy R. Slatyer, and Wei Xue. Evidence for Unresolved γ-Ray Point Sources in the Inner Galaxy. *Phys. Rev. Lett.*, 116(5):051103, 2016. arXiv:1506.05124, doi:10.1103/PhysRevLett.116.051103.

[103] Rebecca K. Leane and Tracy R. Slatyer. Revival of the Dark Matter Hypothesis for the Galactic Center Gamma-Ray Excess. *Phys. Rev. Lett.*, 123(24):241101, 2019. arXiv:1904.08430, doi:10.1103/PhysRevLett.123.241101.

[104] A. Albert et al. Searching for Dark Matter Annihilation in Recently Discovered Milky Way Satellites with Fermi-LAT. *Astrophys. J.*, 834(2):110, 2017. arXiv:1611.03184, doi:10.3847/1538-4357/834/2/110.

[105] Avirup Ghosh, Alejandro Ibarra, Tanmoy Mondal, and Biswarup Mukhopadhyaya. Gamma-ray signals from multicomponent scalar dark matter decays. 2019. arXiv:1909.13292.

[106] Igor V. Moskalenko, Andrew W. Strong, and Olaf Reimer. Diffuse gamma-rays: Galactic and extragalactic diffuse emission. *Astrophys. Space Sci. Libr.*, 304:279, 2004. arXiv:astro-ph/0402243, doi:10.1007/978-1-4020-2256-2_12.

[107] Torsten Bringmann, Xiaoyuan Huang, Alejandro Ibarra, Stefan Vogl, and Christoph Weniger. Fermi LAT Search for Internal Bremsstrahlung Signatures from Dark Matter Annihilation. *JCAP*, 07:054, 2012. arXiv:1203.1312, doi:10.1088/1475-7516/2012/07/054.

[108] M. Ackermann et al. Updated search for spectral lines from Galactic dark matter interactions with pass 8 data from the Fermi Large Area Telescope. *Phys. Rev.*, D91(12):122002, 2015. arXiv:1506.00013, doi:10.1103/PhysRevD.91.122002.

[109] A. Boyarsky, D. Iakubovskyi, O. Ruchayskiy, and D. Savchenko. Surface brightness profile of the 3.5 keV line in the Milky Way halo. 12 2018. arXiv:1812.10488.

[110] Edward A. Baltz, Marco Battaglia, Michael E. Peskin, and Tommer Wizansky. Determination of dark matter properties at high-energy colliders. *Phys. Rev. D*, 74:103521, 2006. arXiv:hep-ph/0602187, doi:10.1103/PhysRevD.74.103521.

[111] Patrick J. Fox, Roni Harnik, Joachim Kopp, and Yuhsin Tsai. LEP Shines Light on Dark Matter. *Phys. Rev. D*, 84:014028, 2011. arXiv:1103.0240, doi:10.1103/PhysRevD.84.014028.

[112] Jalal Abdallah et al. Simplified Models for Dark Matter Searches at the LHC. *Phys. Dark Univ.*, 9-10:8–23, 2015. arXiv:1506.03116, doi:10.1016/j.dark.2015.08.001.

[113] G. Bélanger et al. LHC-friendly minimal freeze-in models. *JHEP*, 02:186, 2019. arXiv:1811.05478, doi:10.1007/JHEP02(2019)186.

[114] Dark matter summary plots : update July 2020. Technical Report ATL-PHYS-PUB-2020-021, CERN, Geneva, Jul 2020. URL: http://cds.cern.ch/record/2725266.

[115] Albert M. Sirunyan et al. Search for supersymmetric partners of electrons and muons in proton-proton collisions at $\sqrt{s} = 13$ TeV. *Phys. Lett. B*, 790:140–166, 2019. arXiv:1806.05264, doi:10.1016/j.physletb.2019.01.005.

[116] M. Aaboud et al. Search for electroweak production of supersymmetric particles in final states with two or three leptons at $\sqrt{s} = 13$ TeV with the ATLAS detector. *Eur. Phys. J. C*, 78(12):995, 2018. arXiv:1803.02762, doi:10.1140/epjc/s10052-018-6423-7.

[117] Morad Aaboud et al. Search for heavy charged long-lived particles in the ATLAS detector in 36.1 fb^{-1} of proton-proton collision data at $\sqrt{s} = 13$ TeV. *Phys. Rev.*, D99(9):092007, 2019. arXiv:1902.01636, doi:10.1103/PhysRevD.99.092007.

[118] Mark W. Goodman and Edward Witten. Detectability of Certain Dark Matter Candidates. *Phys. Rev. D*, 31:3059, 1985. doi:10.1103/PhysRevD.31.3059.

[119] David G. Cerdeno and Anne M. Green. Direct detection of WIMPs. pages 347–369, 2 2010. arXiv:1002.1912.

[120] E. Aprile et al. Dark Matter Search Results from a One Ton-Year Exposure of XENON1T. *Phys. Rev. Lett.*, 121(11):111302, 2018. arXiv:1805.12562, doi:10.1103/PhysRevLett.121.111302.

[121] R. Bernabei et al. New results from DAMA/LIBRA. *Eur. Phys. J. C*, 67:39–49, 2010. arXiv:1002.1028, doi:10.1140/epjc/s10052-010-1303-9.

[122] Thomas Hambye, Michel H. G. Tytgat, Jérôme Vandecasteele, and Laurent Vanderheyden. Dark matter direct detection is testing freeze-in. *Phys. Rev.*, D98(7):075017, 2018. arXiv:1807.05022, doi:10.1103/PhysRevD.98.075017.

[123] Lars Husdal. On Effective Degrees of Freedom in the Early Universe. *Galaxies*, 4(4):78, 2016. arXiv:1609.04979, doi:10.3390/galaxies4040078.

[124] Paolo Gondolo and Graciela Gelmini. Cosmic abundances of stable particles: Improved analysis. *Nucl. Phys.*, B360:145–179, 1991. doi:10.1016/0550-3213(91)90438-4.

[125] Tobias Binder, Torsten Bringmann, Michael Gustafsson, and Andrzej Hryczuk. Early kinetic decoupling of dark matter: when the standard way of calculating the thermal relic density fails. *Phys. Rev. D*, 96(11):115010, 2017. [Erratum: Phys.Rev.D 101, 099901 (2020)]. arXiv:1706.07433, doi:10.1103/PhysRevD.96.115010.

[126] Geneviève Bélanger, Fawzi Boudjema, Andreas Goudelis, Alexander Pukhov, and Bryan Zaldivar. micrOMEGAs5.0 : Freeze-in. *Comput. Phys. Commun.*, 231:173–186, 2018. arXiv:1801.03509, doi:10.1016/j.cpc.2018.04.027.

[127] Oleg Lebedev and Takashi Toma. Relativistic Freeze-in. 2019. arXiv:1908.05491.

[128] Giorgio Arcadi, Oleg Lebedev, Stefan Pokorski, and Takashi Toma. Real Scalar Dark Matter: Relativistic Treatment. *JHEP*, 08:050, 2019. arXiv:1906.07659, doi:10.1007/JHEP08(2019)050.

[129] Valentina De Romeri, Dimitrios Karamitros, Oleg Lebedev, and Takashi Toma. Neutrino dark matter and the Higgs portal: improved freeze-in analysis. 3 2020. arXiv:2003.12606.

[130] J.R. Bond, G. Efstathiou, and J. Silk. Massive Neutrinos and the Large Scale Structure of the Universe. *Phys. Rev. Lett.*, 45:1980–1984, 1980. doi:10.1103/PhysRevLett.45.1980.

[131] Steen Hannestad and Georg Raffelt. Cosmological mass limits on neutrinos, axions, and other light particles. *JCAP*, 04:008, 2004. arXiv:hep-ph/0312154, doi:10.1088/1475-7516/2004/04/008.

[132] Robert J. Scherrer and Michael S. Turner. On the Relic, Cosmic Abundance of Stable Weakly Interacting Massive Particles. *Phys. Rev. D*, 33:1585, 1986. [Erratum: Phys.Rev.D 34, 3263 (1986)]. doi:10.1103/PhysRevD.33.1585.

[133] Graciela B. Gelmini, Philip Lu, and Volodymyr Takhistov. Cosmological Dependence of Non-resonantly Produced Sterile Neutrinos. *JCAP*, 12:047, 2019. arXiv:1909.13328, doi:10.1088/1475-7516/2019/12/047.

[134] Kim Griest and Marc Kamionkowski. Unitarity Limits on the Mass and Radius of Dark Matter Particles. *Phys. Rev. Lett.*, 64:615, 1990. doi:10.1103/PhysRevLett.64.615.

[135] Juri Smirnov and John F. Beacom. TeV-Scale Thermal WIMPs: Unitarity and its Consequences. *Phys. Rev. D*, 100(4):043029, 2019. arXiv:1904.11503, doi:10.1103/PhysRevD.100.043029.

[136] Céline Boehm, Matthew J. Dolan, and Christopher McCabe. A Lower Bound on the Mass of Cold Thermal Dark Matter from Planck. *JCAP*, 08:041, 2013. arXiv:1303.6270, doi:10.1088/1475-7516/2013/08/041.

[137] Kim Griest and David Seckel. Three exceptions in the calculation of relic abundances. *Phys. Rev. D*, 43:3191–3203, 1991. doi:10.1103/PhysRevD.43.3191.

[138] Xiaoyong Chu, Thomas Hambye, and Michel H. G. Tytgat. The Four Basic Ways of Creating Dark Matter Through a Portal. *JCAP*, 1205:034, 2012. arXiv:1112.0493, doi:10.1088/1475-7516/2012/05/034.

[139] Saniya Heeba and Felix Kahlhoefer. Probing the freeze-in mechanism in dark matter models with U(1) gauge extensions. *Phys. Rev. D*, 101(3):035043, 2020. arXiv:1908.09834, doi:10.1103/PhysRevD.101.035043.

[140] Sam Junius, Laura Lopez-Honorez, and Alberto Mariotti. A feeble window on leptophilic dark matter. *JHEP*, 07:136, 2019. arXiv:1904.07513, doi:10.1007/JHEP07(2019)136.

[141] Mathias Garny and Jan Heisig. Interplay of super-WIMP and freeze-in production of dark matter. *Phys. Rev.*, D98(9):095031, 2018. arXiv:1809.10135, doi:10.1103/PhysRevD.98.095031.

[142] Saniya Heeba, Felix Kahlhoefer, and Patrick Stöcker. Freeze-in production of decaying dark matter in five steps. *JCAP*, 1811(11):048, 2018. arXiv:1809.04849, doi:10.1088/1475-7516/2018/11/048.

[143] Andre G. Hessler, Alejandro Ibarra, Emiliano Molinaro, and Stefan Vogl. Probing the scotogenic FIMP at the LHC. *JHEP*, 01:100, 2017. arXiv:1611.09540, doi:10.1007/JHEP01(2017)100.

[144] Kyu Jung Bae, Myeonghun Park, and Mengchao Zhang. Demystifying freeze-in dark matter at the LHC. *Phys. Rev. D*, 101(11):115036, 2020. arXiv:2001.02142, doi:10.1103/PhysRevD.101.115036.

[145] Carlos E. Yaguna. The Singlet Scalar as FIMP Dark Matter. *JHEP*, 08:060, 2011. arXiv:1105.1654, doi:10.1007/JHEP08(2011)060.

[146] Nicolás Bernal. Boosting Freeze-in through Thermalization. 5 2020. arXiv:2005.08988.

[147] Vanda Silveira and A. Zee. SCALAR PHANTOMS. *Phys. Lett. B*, 161:136–140, 1985. doi:10.1016/0370-2693(85)90624-0.

[148] John McDonald. Gauge singlet scalars as cold dark matter. *Phys. Rev. D*, 50:3637–3649, 1994. arXiv:hep-ph/0702143, doi:10.1103/PhysRevD.50.3637.

[149] C.P. Burgess, Maxim Pospelov, and Tonnis ter Veldhuis. The Minimal model of nonbaryonic dark matter: A Singlet scalar. *Nucl. Phys. B*, 619:709–728, 2001. arXiv:hep-ph/0011335, doi:10.1016/S0550-3213(01)00513-2.

[150] Peter Athron et al. Status of the scalar singlet dark matter model. *Eur. Phys. J. C*, 77(8):568, 2017. arXiv:1705.07931, doi:10.1140/epjc/s10052-017-5113-1.

[151] Geneviève Bélanger, Fawzi Boudjema, Andreas Goudelis, Alexander Pukhov, and Bryan Zaldivar. micrOMEGAs5.0 : Freeze-in. *Comput. Phys. Commun.*, 231:173–186, 2018. arXiv:1801.03509, doi:10.1016/j.cpc.2018.04.027.

[152] L. Bouchet, E. Jourdain, J. P. Roques, A. Strong, R. Diehl, F. Lebrun, and R. Terrier. INTEGRAL SPI All-Sky View in Soft Gamma Rays: Study of Point Source and Galactic Diffuse Emissions. *Astrophys. J.*, 679:1315, 2008. arXiv:0801.2086, doi:10.1086/529489.

[153] G. Weidenspointner, M. Varendorff, K. Bennett, H. Bloemen, W. Hermsen, S. C. Kappadath, G. G. Lichti, J. Ryan, and V. Schönfelder. The Cdg Spectrum from 0.8-30 MeV Measured with COMPTEL Based on a Physical Model of the Instrumental Background. *Astrophysical Letters and Communications*, 39:193, Jan 1999.

[154] Andrew W. Strong, Igor V. Moskalenko, and Olaf Reimer. Diffuse galactic continuum gamma rays. A Model compatible with EGRET data and cosmic-ray measurements. *Astrophys. J.*, 613:962–976, 2004. arXiv:astro-ph/0406254, doi:10.1086/423193.

[155] M. Ackermann et al. The spectrum of isotropic diffuse gamma-ray emission between 100 MeV and 820 GeV. *Astrophys. J.*, 799:86, 2015. arXiv:1410.3696, doi:10.1088/0004-637X/799/1/86.

[156] Adam Alloul, Neil D. Christensen, Céline Degrande, Claude Duhr, and Benjamin Fuks. FeynRules 2.0 - A complete toolbox for tree-level phenomenology. *Comput. Phys. Commun.*, 185:2250–2300, 2014. arXiv:1310.1921, doi:10.1016/j.cpc.2014.04.012.

[157] Alexander Belyaev, Neil D. Christensen, and Alexander Pukhov. CalcHEP 3.4 for collider physics within and beyond the Standard Model. *Comput. Phys. Commun.*, 184:1729–1769, 2013. arXiv:1207.6082, doi:10.1016/j.cpc.2013.01.014.

[158] Tracy R. Slatyer and Chih-Liang Wu. General Constraints on Dark Matter Decay from the Cosmic Microwave Background. *Phys. Rev.*, D95(2):023010, 2017. arXiv:1610.06933, doi:10.1103/PhysRevD.95.023010.

[159] Laura Covi, Jihn E. Kim, and Leszek Roszkowski. Axinos as cold dark matter. *Phys. Rev. Lett.*, 82:4180–4183, 1999. arXiv:hep-ph/9905212, doi:10.1103/PhysRevLett.82.4180.

[160] Jonathan L. Feng, Arvind Rajaraman, and Fumihiro Takayama. SuperWIMP dark matter signals from the early universe. *Phys. Rev. D*, 68:063504, 2003. arXiv:hep-ph/0306024, doi:10.1103/PhysRevD.68.063504.

[161] Ayuki Kamada and Keisuke Yanagi. Constraining FIMP from the structure formation of the Universe: analytic mapping from $m_{\rm WDM}$. 2019. arXiv:1907.04558.

[162] Vardan Khachatryan et al. Search for long-lived charged particles in proton-proton collisions at $\sqrt{s} = 13$ TeV. *Phys. Rev.*, D94(11):112004, 2016. arXiv:1609.08382, doi:10.1103/PhysRevD.94.112004.

[163] Masahiro Kawasaki, Kazunori Kohri, Takeo Moroi, and Yoshitaro Takaesu. Revisiting Big-Bang Nucleosynthesis Constraints on Long-Lived Decaying Particles. *Phys. Rev.*, D97(2):023502, 2018. arXiv:1709.01211, doi:10.1103/PhysRevD.97.023502.

[164] Kerstin Perez, Kenny C. Y. Ng, John F. Beacom, Cora Hersh, Shunsaku Horiuchi, and Roman Krivonos. Almost closing the νMSM sterile neutrino dark matter window with NuSTAR. *Phys. Rev. D*, 95(12):123002, 2017. arXiv:1609.00667, doi:10.1103/PhysRevD.95.123002.

[165] Regina Caputo et al. All-sky Medium Energy Gamma-ray Observatory: Exploring the Extreme Multimessenger Universe. 2019. arXiv:1907.07558.

[166] Richard Bartels, Daniele Gaggero, and Christoph Weniger. Prospects for indirect dark matter searches with MeV photons. *JCAP*, 05:001, 2017. arXiv:1703.02546, doi:10.1088/1475-7516/2017/05/001.

[167] M. Tavani et al. Science with e-ASTROGAM: A space mission for MeV–GeV gamma-ray astrophysics. *JHEAp*, 19:1–106, 2018. arXiv:1711.01265, doi:10.1016/j.jheap.2018.07.001.

[168] Mathias Garny, Alejandro Ibarra, and Stefan Vogl. Dark matter annihilations into two light fermions and one gauge boson: General analysis and antiproton constraints. *JCAP*, 04:033, 2012. arXiv:1112.5155, doi:10.1088/1475-7516/2012/04/033.

[169] Mathias Garny, Alejandro Ibarra, Miguel Pato, and Stefan Vogl. Internal bremsstrahlung signatures in light of direct dark matter searches. *JCAP*, 12:046, 2013. arXiv:1306.6342, doi:10.1088/1475-7516/2013/12/046.

[170] Mathias Garny, Alejandro Ibarra, Sara Rydbeck, and Stefan Vogl. Majorana Dark Matter with a Coloured Mediator: Collider vs Direct and Indirect Searches. *JHEP*, 06:169, 2014. arXiv:1403.4634, doi:10.1007/JHEP06(2014)169.

[171] Mathias Garny, Alejandro Ibarra, and Stefan Vogl. Signatures of Majorana dark matter with t-channel mediators. *Int. J. Mod. Phys.*, D24(07):1530019, 2015. arXiv:1503.01500, doi:10.1142/S0218271815300190.

[172] Mathias Garny, Jan Heisig, Benedikt Lülf, and Stefan Vogl. Coannihilation without chemical equilibrium. *Phys. Rev.*, D96(10):103521, 2017. arXiv:1705.09292, doi:10.1103/PhysRevD.96.103521.

[173] Mathias Garny, Jan Heisig, Marco Hufnagel, and Benedikt Lülf. Top-philic dark matter within and beyond the WIMP paradigm. *Phys. Rev.*, D97(7):075002, 2018. arXiv:1802.00814, doi:10.1103/PhysRevD.97.075002.

[174] Joachim Kopp, Lisa Michaels, and Juri Smirnov. Loopy Constraints on Leptophilic Dark Matter and Internal Bremsstrahlung. *JCAP*, 1404:022, 2014. arXiv:1401.6457, doi:10.1088/1475-7516/2014/04/022.

[175] Lars Bergstrom, Torsten Bringmann, and Joakim Edsjo. New Positron Spectral Features from Supersymmetric Dark Matter - a Way to Explain the PAMELA Data? *Phys. Rev.*, D78:103520, 2008. arXiv:0808.3725, doi:10.1103/PhysRevD.78.103520.

[176] Ernest Ma. Verifiable radiative seesaw mechanism of neutrino mass and dark matter. *Phys. Rev. D*, 73:077301, 2006. arXiv:hep-ph/0601225, doi:10.1103/PhysRevD.73.077301.

[177] Emiliano Molinaro, Carlos E. Yaguna, and Oscar Zapata. FIMP realization of the scotogenic model. *JCAP*, 1407:015, 2014. arXiv:1405.1259, doi:10.1088/1475-7516/2014/07/015.

[178] Rouven Essig, Eric Kuflik, Samuel D. McDermott, Tomer Volansky, and Kathryn M. Zurek. Constraining Light Dark Matter with Diffuse X-Ray and Gamma-Ray Observations. *JHEP*, 11:193, 2013. arXiv:1309.4091, doi:10.1007/JHEP11(2013)193.

[179] Wolfram Mathematica: Modern Technical Computing. URL: https://www.wolfram.com/mathematica/.

[180] Raffaele Tito D'Agnolo, Duccio Pappadopulo, and Joshua T. Ruderman. Fourth Exception in the Calculation of Relic Abundances. *Phys. Rev. Lett.*, 119(6):061102, 2017. arXiv:1705.08450, doi:10.1103/PhysRevLett.119.061102.

[181] Torsten Bringmann, Joakim Edsjö, Paolo Gondolo, Piero Ullio, and Lars Bergström. DarkSUSY 6 : An Advanced Tool to Compute Dark Matter Properties Numerically. *JCAP*, 07:033, 2018. arXiv:1802.03399, doi:10.1088/1475-7516/2018/07/033.

[182] Malcolm Fairbairn and Jure Zupan. Dark matter with a late decaying dark partner. *JCAP*, 07:001, 2009. arXiv:0810.4147, doi:10.1088/1475-7516/2009/07/001.

[183] Mathias Garny, Alejandro Ibarra, David Tran, and Christoph Weniger. Gamma-Ray Lines from Radiative Dark Matter Decay. *JCAP*, 1101:032, 2011. arXiv:1011.3786, doi:10.1088/1475-7516/2011/01/032.

[184] D.J. Fixsen, E.S. Cheng, J.M. Gales, John C. Mather, R.A. Shafer, and E.L. Wright. The Cosmic Microwave Background spectrum from the full COBE FIRAS data set. *Astrophys. J.*, 473:576, 1996. arXiv:astro-ph/9605054, doi:10.1086/178173.

[185] Vivian Poulin, Julien Lesgourgues, and Pasquale D. Serpico. Cosmological constraints on exotic injection of electromagnetic energy. *JCAP*, 03:043, 2017. arXiv:1610.10051, doi:10.1088/1475-7516/2017/03/043.

[186] Masahiro Kawasaki, Kazunori Kohri, Takeo Moroi, Kai Murai, and Hitoshi Murayama. Big-bang nucleosynthesis with sub-GeV massive decaying particles. 6 2020. arXiv:2006.14803.

[187] Lars Bergstrom, Torsten Bringmann, Ilias Cholis, Dan Hooper, and Christoph Weniger. New Limits on Dark Matter Annihilation from AMS Cosmic Ray Positron Data. *Phys. Rev. Lett.*, 111:171101, 2013. arXiv:1306.3983, doi:10.1103/PhysRevLett.111.171101.

[188] Alejandro Ibarra, Anna S. Lamperstorfer, and Joseph Silk. Dark matter annihilations and decays after the AMS-02 positron measurements. *Phys. Rev.*, D89(6):063539, 2014. arXiv:1309.2570, doi:10.1103/PhysRevD.89.063539.

[189] H. Goldberg. Constraint on the Photino Mass from Cosmology. *Phys. Rev. Lett.*, 50:1419, 1983. [Erratum: Phys.Rev.Lett. 103, 099905 (2009)]. doi:10.1103/PhysRevLett.50.1419.

[190] Giuseppina Battaglia, Amina Helmi, Heather Morrison, Paul Harding, Edward W. Olszewski, Mario Mateo, Kenneth C. Freeman, John Norris, and Stephen A. Shectman. The Radial velocity dispersion profile of the Galactic Halo: Constraining the density profile of the dark halo of the Milky Way. *Mon. Not. Roy. Astron. Soc.*, 364:433–442, 2005. [Erratum: Mon.Not.Roy.Astron.Soc. 370, 1055 (2006)]. arXiv:astro-ph/0506102, doi:10.1111/j.1365-2966.2005.09367.x.

[191] Torsten Bringmann, Lars Bergstrom, and Joakim Edsjo. New Gamma-Ray Contributions to Supersymmetric Dark Matter Annihilation. *JHEP*, 01:049, 2008. arXiv:0710.3169, doi:10.1088/1126-6708/2008/01/049.

[192] Rebecca K. Leane, Tracy R. Slatyer, John F. Beacom, and Kenny C.Y. Ng. GeV-scale thermal WIMPs: Not even slightly ruled out. *Phys. Rev. D*, 98(2):023016, 2018. arXiv:1805.10305, doi:10.1103/PhysRevD.98.023016.

[193] Oscar Adriani et al. An anomalous positron abundance in cosmic rays with energies 1.5-100 GeV. *Nature*, 458:607–609, 2009. arXiv:0810.4995, doi:10.1038/nature07942.

[194] J. Chang et al. An excess of cosmic ray electrons at energies of 300-800 GeV. *Nature*, 456:362–365, 2008. doi:10.1038/nature07477.

[195] Marco Cirelli, Mario Kadastik, Martti Raidal, and Alessandro Strumia. Model-independent implications of the e+-, anti-proton cosmic ray spectra on properties of Dark Matter. *Nucl. Phys. B*, 813:1–21, 2009. [Addendum: Nucl.Phys.B 873, 530–533 (2013)]. arXiv:0809.2409, doi:10.1016/j.nuclphysb.2008.11.031.

[196] Ilias Cholis, Lisa Goodenough, Dan Hooper, Melanie Simet, and Neal Weiner. High Energy Positrons From Annihilating Dark Matter. *Phys. Rev. D*, 80:123511, 2009. arXiv:0809.1683, doi:10.1103/PhysRevD.80.123511.

[197] J. Diemand, M. Kuhlen, P. Madau, M. Zemp, B. Moore, D. Potter, and J. Stadel. Clumps and streams in the local dark matter distribution. *Nature*, 454:735–738, 2008. arXiv:0805.1244, doi:10.1038/nature07153.

[198] Junji Hisano, Shigeki. Matsumoto, Mihoko M. Nojiri, and Osamu Saito. Non-perturbative effect on dark matter annihilation and gamma ray signature from galactic center. *Phys. Rev. D*, 71:063528, 2005. arXiv:hep-ph/0412403, doi:10.1103/PhysRevD.71.063528.

[199] Marco Cirelli, Alessandro Strumia, and Matteo Tamburini. Cosmology and Astrophysics of Minimal Dark Matter. *Nucl. Phys. B*, 787:152–175, 2007. arXiv:0706.4071, doi:10.1016/j.nuclphysb.2007.07.023.

[200] Marco Cirelli and Alessandro Strumia. Minimal Dark Matter predictions and the PAMELA positron excess. *PoS*, IDM2008:089, 2008. arXiv:0808.3867, doi:10.22323/1.064.0089.

[201] Georges Aad et al. Search for direct production of charginos, neutralinos and sleptons in final states with two leptons and missing transverse momentum in pp collisions at $\sqrt{s} = 8$ TeV with the ATLAS detector. *JHEP*, 05:071, 2014. arXiv:1403.5294, doi:10.1007/JHEP05(2014)071.

[202] Vardan Khachatryan et al. Searches for electroweak production of charginos, neutralinos, and sleptons decaying to leptons and W, Z, and Higgs bosons in pp collisions at 8 TeV. *Eur. Phys. J. C*, 74(9):3036, 2014. arXiv:1405.7570, doi:10.1140/epjc/s10052-014-3036-7.

[203] Morad Aaboud et al. Search for electroweak production of supersymmetric states in scenarios with compressed mass spectra at $\sqrt{s} = 13$ TeV with the ATLAS detector. *Phys. Rev. D*, 97(5):052010, 2018. arXiv:1712.08119, doi:10.1103/PhysRevD.97.052010.

[204] Georges Aad et al. Search for the direct production of charginos, neutralinos and staus in final states with at least two hadronically decaying taus and missing transverse momentum in pp collisions at $\sqrt{s} = 8$ TeV with the ATLAS detector. *JHEP*, 10:096, 2014. arXiv:1407.0350, doi:10.1007/JHEP10(2014)096.

[205] Georges Aad et al. Search for direct stau production in events with two hadronic τ-leptons in $\sqrt{s} = 13$ TeV pp collisions with the ATLAS detector. *Phys. Rev. D*, 101(3):032009, 2020. arXiv:1911.06660, doi:10.1103/PhysRevD.101.032009.

[206] Albert M. Sirunyan et al. Search for supersymmetry in events with a τ lepton pair and missing transverse momentum in proton-proton collisions at $\sqrt{s} = 13$ TeV. *JHEP*, 11:151, 2018. arXiv:1807.02048, doi:10.1007/JHEP11(2018)151.

[207] Lorenzo Calibbi, Laura Lopez-Honorez, Steven Lowette, and Alberto Mariotti. Singlet-Doublet Dark Matter Freeze-in: LHC displaced signatures versus cosmology. *JHEP*, 09:037, 2018. arXiv:1805.04423, doi:10.1007/JHEP09(2018)037.

[208] Jose Miguel No, Patrick Tunney, and Bryan Zaldivar. Probing Dark Matter freeze-in with long-lived particle signatures: MATHUSLA, HL-LHC and FCC-hh. *JHEP*, 03:022, 2020. arXiv:1908.11387, doi:10.1007/JHEP03(2020)022.

[209] Zachary Flowers, Quinn Meier, Christopher Rogan, Dong Woo Kang, and Seong Chan Park. Timing information at HL-LHC: Complete determination of masses of Dark Matter and Long lived particle. *JHEP*, 03:132, 2020. arXiv:1903.05825, doi:10.1007/JHEP03(2020)132.

[210] Georges Aad et al. Search for displaced vertices of oppositely charged leptons from decays of long-lived particles in pp collisions at $\sqrt{s}$ =13 TeV with the ATLAS detector. *Phys. Lett.*, B801:135114, 2020. arXiv:1907.10037, doi:10.1016/j.physletb.2019.135114.

[211] Morad Aaboud et al. Search for long-lived particles in final states with displaced dimuon vertices in pp collisions at $\sqrt{s} = 13$ TeV with the ATLAS detector. *Phys. Rev. D*, 99(1):012001, 2019. arXiv:1808.03057, doi:10.1103/PhysRevD.99.012001.

[212] Georges Aad et al. Search for light long-lived neutral particles produced in pp collisions at $\sqrt{s} = 13$ TeV and decaying into collimated leptons or light hadrons with the ATLAS detector. 9 2019. arXiv:1909.01246.

[213] Vardan Khachatryan et al. Search for long-lived particles that decay into final states containing two electrons or two muons in proton-proton collisions at $\sqrt{s} = 8$ TeV. *Phys. Rev. D*, 91(5):052012, 2015. arXiv:1411.6977, doi:10.1103/PhysRevD.91.052012.

[214] John Paul Chou, David Curtin, and H.J. Lubatti. New Detectors to Explore the Lifetime Frontier. *Phys. Lett. B*, 767:29–36, 2017. arXiv:1606.06298, doi:10.1016/j.physletb.2017.01.043.

[215] E. Aprile et al. Light Dark Matter Search with Ionization Signals in XENON1T. *Phys. Rev. Lett.*, 123(25):251801, 2019. arXiv:1907.11485, doi:10.1103/PhysRevLett.123.251801.

[216] Tatsumi Aoyama, Masashi Hayakawa, Toichiro Kinoshita, and Makiko Nio. Tenth-Order QED Contribution to the Electron g-2 and an Improved Value of the Fine Structure Constant. *Phys. Rev. Lett.*, 109:111807, 2012. arXiv:1205.5368, doi:10.1103/PhysRevLett.109.111807.

[217] Keith R. Dienes, Doojin Kim, Huayang Song, Shufang Su, Brooks Thomas, and David Yaylali. Nonminimal dark sectors: Mediator-induced decay chains and multijet collider signatures. *Phys. Rev. D*, 101(7):075024, 2020. arXiv:1910.01129, doi:10.1103/PhysRevD.101.075024.

[218] Peter Minkowski. $\mu \to e\gamma$ at a Rate of One Out of 10^9 Muon Decays? *Phys. Lett.*, 67B:421–428, 1977. doi:10.1016/0370-2693(77)90435-X.

[219] Rabindra N. Mohapatra and Goran Senjanovic. Neutrino Mass and Spontaneous Parity Violation. *Phys. Rev. Lett.*, 44:912, 1980. doi:10.1103/PhysRevLett.44.912.

[220] Tsutomu Yanagida. HORIZONTAL SYMMETRY AND MASSES OF NEUTRINOS. *Conf. Proc.*, C7902131:95–99, 1979.

[221] Murray Gell-Mann, Pierre Ramond, and Richard Slansky. Complex Spinors and Unified Theories. *Conf. Proc.*, C790927:315–321, 1979. arXiv:1306.4669.

[222] J. Schechter and J. W. F. Valle. Neutrino Masses in SU(2) x U(1) Theories. *Phys. Rev.*, D22:2227, 1980. doi:10.1103/PhysRevD.22.2227.

[223] M. Drewes et al. A White Paper on keV Sterile Neutrino Dark Matter. *JCAP*, 1701(01):025, 2017. arXiv:1602.04816, doi:10.1088/1475-7516/2017/01/025.

[224] Kevork N. Abazajian. Sterile neutrinos in cosmology. *Phys. Rept.*, 711-712:1–28, 2017. arXiv:1705.01837, doi:10.1016/j.physrep.2017.10.003.

[225] Alexander Kusenko. Sterile neutrinos: The Dark side of the light fermions. *Phys. Rept.*, 481:1–28, 2009. arXiv:0906.2968, doi:10.1016/j.physrep.2009.07.004.

[226] Xiang-Dong Shi and George M. Fuller. A New dark matter candidate: Nonthermal sterile neutrinos. *Phys. Rev. Lett.*, 82:2832–2835, 1999. arXiv:astro-ph/9810076, doi:10.1103/PhysRevLett.82.2832.

[227] Shunsaku Horiuchi, Philip J. Humphrey, Jose Onorbe, Kevork N. Abazajian, Manoj Kaplinghat, and Shea Garrison-Kimmel. Sterile neutrino dark matter bounds from galaxies of the Local Group. *Phys. Rev.*, D89(2):025017, 2014. arXiv:1311.0282, doi:10.1103/PhysRevD.89.025017.

[228] Esra Bulbul, Maxim Markevitch, Adam Foster, Randall K. Smith, Michael Loewenstein, and Scott W. Randall. Detection of An Unidentified Emission Line in the Stacked X-ray spectrum of Galaxy Clusters. *Astrophys. J.*, 789:13, 2014. arXiv:1402.2301, doi:10.1088/0004-637X/789/1/13.

[229] Alexey Boyarsky, Oleg Ruchayskiy, Dmytro Iakubovskyi, and Jeroen Franse. Unidentified Line in X-Ray Spectra of the Andromeda Galaxy and Perseus Galaxy Cluster. *Phys. Rev. Lett.*, 113:251301, 2014. arXiv:1402.4119, doi:10.1103/PhysRevLett.113.251301.

[230] Christopher Dessert, Nicholas L. Rodd, and Benjamin R. Safdi. The dark matter interpretation of the 3.5-keV line is inconsistent with blank-sky observations. *Science*, 367:1465, 2020. arXiv:1812.06976, doi:10.1126/science.aaw3772.

[231] Alexey Boyarsky, Denys Malyshev, Oleg Ruchayskiy, and Denys Savchenko. Technical comment on the paper of Dessert et al. "The dark matter interpretation of the 3.5 keV line is inconsistent with blank-sky observations". 4 2020. arXiv:2004.06601.

[232] Christopher Dessert, Nicholas L. Rodd, and Benjamin R. Safdi. Response to a comment on Dessert et al. "The dark matter interpretation of the 3.5 keV line is inconsistent with blank-sky observations". 6 2020. arXiv:2006.03974.

[233] Aurel Schneider. Astrophysical constraints on resonantly produced sterile neutrino dark matter. *JCAP*, 1604(04):059, 2016. arXiv:1601.07553, doi:10.1088/1475-7516/2016/04/059.

[234] Alexander Kusenko. Sterile neutrinos, dark matter, and the pulsar velocities in models with a Higgs singlet. *Phys. Rev. Lett.*, 97:241301, 2006. arXiv:hep-ph/0609081, doi:10.1103/PhysRevLett.97.241301.

[235] Kalliopi Petraki and Alexander Kusenko. Dark-matter sterile neutrinos in models with a gauge singlet in the Higgs sector. *Phys. Rev.*, D77:065014, 2008. arXiv:0711.4646, doi:10.1103/PhysRevD.77.065014.

[236] Alexander Merle, Viviana Niro, and Daniel Schmidt. New production mechanism for kev sterile neutrino dark matter by decays of frozen-in scalars. *JCAP*, 1403:028, 2014. arXiv:1306.3996, doi:10.1088/1475-7516/2014/03/028.

[237] Johannes König, Alexander Merle, and Maximilian Totzauer. keV Sterile Neutrino Dark Matter from Singlet Scalar Decays: The Most General Case. *JCAP*, 1611(11):038, 2016. arXiv:1609.01289, doi:10.1088/1475-7516/2016/11/038.

[238] Rasmus S. L. Hansen and Stefan Vogl. Thermalizing sterile neutrino dark matter. *Phys. Rev. Lett.*, 119(25):251305, 2017. arXiv:1706.02707, doi:10.1103/PhysRevLett.119.251305.

[239] Andrew A. de Laix, Robert J. Scherrer, and Robert K. Schaefer. Constraints of selfinteracting dark matter. *Astrophys. J.*, 452:495, 1995. arXiv:astro-ph/9502087, doi:10.1086/176322.

[240] Yonit Hochberg, Eric Kuflik, Tomer Volansky, and Jay G. Wacker. Mechanism for Thermal Relic Dark Matter of Strongly Interacting Massive Particles. *Phys. Rev. Lett.*, 113:171301, 2014. arXiv:1402.5143, doi:10.1103/PhysRevLett.113.171301.

[241] Yonit Hochberg, Eric Kuflik, and Hitoshi Murayama. SIMP Spectroscopy. *JHEP*, 05:090, 2016. arXiv:1512.07917, doi:10.1007/JHEP05(2016)090.

[242] Nicolas Bernal, Camilo Garcia-Cely, and Rogerio Rosenfeld. WIMP and SIMP Dark Matter from the Spontaneous Breaking of a Global Group. *JCAP*, 1504(04):012, 2015. arXiv:1501.01973, doi:10.1088/1475-7516/2015/04/012.

[243] Soo-Min Choi and Hyun Min Lee. SIMP dark matter with gauged Z_3 symmetry. *JHEP*, 09:063, 2015. arXiv:1505.00960, doi:10.1007/JHEP09(2015)063.

[244] Shu-Yu Ho, Takashi Toma, and Koji Tsumura. A Radiative Neutrino Mass Model with SIMP Dark Matter. *JHEP*, 07:101, 2017. arXiv:1705.00592, doi:10.1007/JHEP07(2017)101.

[245] Nicolas Bernal and Xiaoyong Chu. $\mathbb{Z}_2$ SIMP Dark Matter. *JCAP*, 1601:006, 2016. arXiv:1510.08527, doi:10.1088/1475-7516/2016/01/006.

[246] Matti Heikinheimo, Tommi Tenkanen, Kimmo Tuominen, and Ville Vaskonen. Observational Constraints on Decoupled Hidden Sectors. *Phys. Rev.*, D94(6):063506, 2016. [Erratum: Phys. Rev.D96,no.10,109902(2017)]. arXiv:1604.02401, doi:10.1103/PhysRevD.96.109902,10.1103/PhysRevD.94.063506.

[247] Nicolás Bernal, Xiaoyong Chu, and Josef Pradler. Simply split strongly interacting massive particles. *Phys. Rev.*, D95(11):115023, 2017. arXiv:1702.04906, doi:10.1103/PhysRevD.95.115023.

[248] Matti Heikinheimo, Tommi Tenkanen, and Kimmo Tuominen. WIMP miracle of the second kind. *Phys. Rev.*, D96(2):023001, 2017. arXiv:1704.05359, doi:10.1103/PhysRevD.96.023001.

[249] Nicolas Bernal, Xiaoyong Chu, Camilo Garcia-Cely, Thomas Hambye, and Bryan Zaldivar. Production Regimes for Self-Interacting Dark Matter. *JCAP*, 1603(03):018, 2016. arXiv:1510.08063, doi:10.1088/1475-7516/2016/03/018.

[250] Matti Heikinheimo, Tommi Tenkanen, and Kimmo Tuominen. Prospects for indirect detection of frozen-in dark matter. 2018. arXiv:1801.03089.

[251] Xiaoyong Chu and Camilo Garcia-Cely. Self-interacting Spin-2 Dark Matter. *Phys. Rev.*, D96(10):103519, 2017. arXiv:1708.06764, doi:10.1103/PhysRevD.96.103519.

[252] Soo-Min Choi, Yonit Hochberg, Eric Kuflik, Hyun Min Lee, Yann Mambrini, Hitoshi Murayama, and Mathias Pierre. Vector SIMP dark matter. *JHEP*, 10:162, 2017. arXiv:1707.01434, doi:10.1007/JHEP10(2017)162.

[253] Yonit Hochberg, Eric Kuflik, Robert Mcgehee, Hitoshi Murayama, and Katelin Schutz. Strongly interacting massive particles through the axion portal. *Phys. Rev. D*, 98(11):115031, 2018. arXiv:1806.10139, doi:10.1103/PhysRevD.98.115031.

[254] Matti Heikinheimo, Kimmo Tuominen, and Kasper Langæble. Hidden strongly interacting massive particles. *Phys. Rev. D*, 97(9):095040, 2018. arXiv:1803.07518, doi:10.1103/PhysRevD.97.095040.

[255] Soo-Min Choi, Hyun Min Lee, and Min-Seok Seo. Cosmic abundances of SIMP dark matter. *JHEP*, 04:154, 2017. arXiv:1702.07860, doi:10.1007/JHEP04(2017)154.

[256] R. Mertig, M. Bohm, and Ansgar Denner. FEYN CALC: Computer algebraic calculation of Feynman amplitudes. *Comput. Phys. Commun.*, 64:345–359, 1991. doi:10.1016/0010-4655(91)90130-D.

[257] Vladyslav Shtabovenko, Rolf Mertig, and Frederik Orellana. New Developments in FeynCalc 9.0. *Comput. Phys. Commun.*, 207:432–444, 2016. arXiv:1601.01167, doi:10.1016/j.cpc.2016.06.008.

[258] Tejaswi Venumadhav, Francis-Yan Cyr-Racine, Kevork N. Abazajian, and Christopher M. Hirata. Sterile neutrino dark matter: Weak interactions in the strong coupling epoch. *Phys. Rev. D*, 94(4):043515, 2016. arXiv:1507.06655, doi:10.1103/PhysRevD.94.043515.